Master's thesis

NTNU
Norwegian University of Science and Technology
Faculty of Natural Sciences
Department of Physics

Armand Sepehri

Transmission Electron Microscopy Characterization of Degradation Mechanisms in Lithium-ion Batteries

Master's thesis in Nanotechnology
Supervisor: Per-Erik Vullum
Co-supervisor: Marte O. Skare & Asbjørn Ulvestad
June 2022

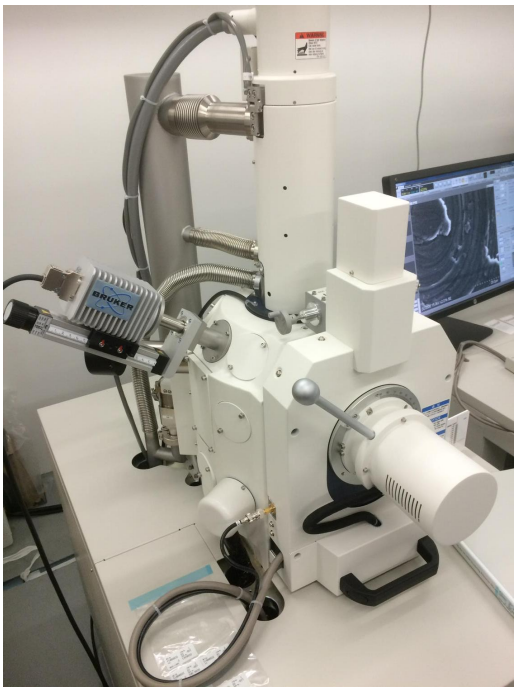

NTNU
Norwegian University of
Science and Technology

Armand Sepehri

Transmission Electron Microscopy Characterization of Degradation Mechanisms in Lithium-ion Batteries

Master's thesis in Nanotechnology
Supervisor: Per-Erik Vullum
Co-supervisor: Marte O. Skare & Asbjørn Ulvestad
June 2022

Norwegian University of Science and Technology
Faculty of Natural Sciences
Department of Physics

NTNU
Norwegian University of
Science and Technology

ABSTRACT

With the increasing need for portable, efficient, and low-cost energy storage devices, lithium-ion batteries (LIBs) have emerged as a promising solution. Silicon has a theoretical capacity that is roughly ten times higher than that of graphite, which has been used as anode material in commercial applications since the invention of LIBs. The main challenge with silicon concerns its substantial volume changes during charging and discharging, which accelerate the degradation of the battery.

In this work, the degradation mechanisms of LIBs have been investigated. Pure silicon and substoichiometric silicon carbide thin films were used as working electrodes in coin-type half cells with lithium metal as the counter electrode. The thin film electrodes were deposited with plasma-enhanced chemical vapor deposition, and the cells were mounted in an inert argon-atmosphere glove box. The electrochemical performance was examined by galvanostatic cycling over 1000 charge/discharge cycles. Transmission electron microscopy (TEM) lamellae were prepared from the thin films with a dual-beam focused ion beam microscope, from which scanning electron microscopy (SEM) images were also acquired. Spectroscopy data were acquired using energy-dispersive X-ray spectroscopy and electron energy-loss spectroscopy. Characterization was performed on films before cycling, after 3 cycles and, after 1000 cycles.

The films exhibited good cycling performance with high capacity retention over 1000 cycles. After cycling, SEM imaging showed significant changes in morphology, and TEM imaging revealed delamination of the pure silicon film. After 1000 cycles, the pure silicon film and the carbon containing film had expanded with 1600 % and 540 %, respectively. Spectroscopy results revealed that a SEI layer of 20 nm - 30 nm had formed after three cycles. After 1000 cycles a significant amount of the silicon had oxidized and was observed stretched with the film. Conclusively the capacity loss is thought to be caused by the loss of active material, while the high cycling stability comes from the practically infinite lithium reservoir in the Li metal counter electrode, excluding degradation due to loss of lithium inventory.

SAMMENDRAG

Litium-ion batterier har fremtredd som en lovende løsning for det økende behovet for bærbare, effektive og billige energilagringsenheter. Grafitt har blitt brukt som anodemateriale i kommersielle litium-ion batterier siden deres opprinnelse, men silisium har en teoretisk kapasitet som er omtrent ti ganger den til grafitt. Hovedproblemet med silisium omhandler de omfattende volumendringene det gjennomgår når det lades opp og lades ut, som forverrer degraderingen av batteriet.

Degraderingsmekanismene til litium-ion batterier har blitt undersøkt i dette arbeidet ved å se på knappceller av halfcelle konfigurasjon med rent silisium og substøkiometrisk silisiumkarbid som aktiv elektrode, og litium metall som motvirkende elektrode. Tynnfilm elektrodene ble deponert med plasmaforsterket kjemisk dampavsetning, og cellene ble montert i en inert argon-atmosfærisk hanskeboks. Den elektrokjemiske ytelsen til cellene ble undersøkt med galvanostatisk over 1000 ladningssykler. Deretter ble transmisjonselektronmikroskopi (TEM) lameller laget fra tynnfilmene med et dobbelstråle fokusert ion-stråle instrument, som det også ble tatt skanneelektronmikroskopi (SEM) bilder med. TEM karakteriseringen innebar lysefelt avbildning og skannende TEM avbildning. Spektroskopidata ble innhetet med energidispersiv røntgenspektroskopi og elektronenergitap spektroskopi. Filmene ble karakterisert før sykling, etter tre sykler og etter 1000 sykler.

Filmende utøvde god syklingsprestasjon med høy kapasitetsbevaring etter 1000 sykler. Etter sykling viste SEM avbildning store endringer i morfologi, og TEM avbildning viste delaminering for filmen av rent silisium. Etter 1000 sykler hadde henholdsvis filmen med rent silisium og den med substøkiometrisk silisiumkarbid utvidet seg 1600 % og 540 %. Spektroskopi viste dannelsen av et passiverende overflatelag av omlag 20 nm-30 nm etter 3 sykler. Etter 1000 sykler hadde en stor andel av silisiumet oksidert, og blitt strukket ut med filmen. Kapasitetstapet i filmene ser ut til å ha skyldtes tap av aktivt materialet. Den gode syklingsstabiliteten kommer fra det omtrent uendelige litium reservoaret i litium metall motelektroden, som utelukket degradering på grunn av tap av litium.

PREFACE

This master's thesis is the product of my work in my last semester studying a master of science degree in nanotechnology at the Norwegian University of Science and Technology (NTNU) in Trondheim.

The work has been carried out during the spring of 2022. Focused ion beam (FIB) work has been done within the Norwegian Micro- and Nano-Fabrication Facility, NorFab (RCN grant 245963/F50). Transmission electron microscopy (TEM) work was carried out at the NORTEM (RCN grant 197405) infrastructure at the TEM Gemini Centre, Trondheim, Norway. Battery cell disassembly was carried out at the Institute for Material Technology at NTNU, Trondheim, Norway. All experimental work was performed by myself, unless otherwise stated. The thin films investigated were produced by supervisor Marte O. Skare at Institute for Energy Technology at Kjeller as part of the SEAMLESS (Screening of Emerging Anode Materials for Li-based Energy Storage Systems) project.

The energy-dispersive X-ray spectroscopy detector on the TEM primarily used in this work, was out of order from January till the beginning of April, which delayed parts of the experimental work. This project has had a steep learning curve, and I have gathered new experiences by the day. With gained experience, there are parts of the experimental work which I would liked to have redone. That includes preparation of TEM samples of higher quality with FIB, and acquiring better images and spectroscopy data.

On the front page is an image of the first electron microscope I ever saw. Until that moment, I had only heard of electron microscopes, and was overwhelmed of finally seeing one in real life. At the time of delivering this thesis, that was seven years, two months and five days ago, and I am proud of what I have achieved since then.

Trondheim - June 20, 2022
Armand Sepehri

ACKNOWLEDGMENTS

I would like to thanks everyone who has been a part of my thesis. First and foremost my closest supervisor, Per Erik Vullum, who through weekly meetings throughout the semester has provided valuable guidance and encouragement. Thank you for teaching me your ways and sharing your expertise. Thanks are due to my supervisors at IFE, Marte O. Skare and Asbjørn Ulvestad for their guidance throughout the semester. Marte, who was also my supervisor during my summer 2021-internship at IFE, has taught me much of what I know about batteries and battery characterization. I would also like to thank Emil Christiansen and Bjørn Gunnar Soleim for providing training in transmission electron microscopy.

Thanks to my parents for continuously motivating me to stay strong, and work harder. I would like to thank my classmates and friends at nanotechnology and material technology for their technical and moral support during moments of struggle.

Lastly, I would like to send out my appreciation to my friends in the NTNUI salsa community, who have taken me in with open arms, and given me so much the last three years. I am very grateful.

ABBREVIATIONS

BF	**B**right-**F**ield
CCD	**C**harge-**C**oupled **D**evice
CE	**C**oulombic **E**fficiency
DF	**D**ark-**F**ield
DMC	**Dim**ethyl **C**arbonate
EC	**E**thylene **C**arbonate
EDS	**E**nergy-**D**ispersive **X**-ray **S**pectroscopy
EELS	**E**lectron **E**nergy **L**oss **S**pectroscopy
EMC	**E**thyl **M**ethyl **C**arbonate
EV	**E**lectric **V**ehicle
FEC	**F**luoro**e**thylene **C**arbonate
FEG	**F**ield **E**mission **G**un
FIB	**F**ocused **I**on **B**eam
GIS	**G**as **I**njection **S**ystem
HAADF	**H**igh-**A**ngle **A**nnular **D**ark-**F**ield
ICE	**I**on **C**onversion and **E**lectron
IFE	**I**nstitute **F**or **E**nergy technology
LIB	**L**ithium-**I**on **B**attery
ROI	**R**egion **o**f **I**nterest
sccm	**S**tandard **C**ubic **cm**
SEM	**S**canning **E**lectron **M**icroscopy
STEM	**S**canning **T**ransmission **E**lectron **M**icroscopy
TEM	**T**ransmission **E**lectron **M**icroscopy
TLD	**T**hrough-**L**ens **D**etector
XPS	**X**-ray **P**hotoelectron **S**pectroscopy

CONTENTS

Abstract i

Sammendrag ii

Preface iii

Acknowledgments iv

Abbreviations v

Contents vi

1 Introduction 1

2 Theory 3

2.1 Batteries . . . 3

2.1.1 Early History . . . 3

2.1.2 Working Principles . . . 3

2.1.3 The Solid Electrolyte Interphase . . . 6

2.1.4 Main Components . . . 8

2.1.5 Cell types . . . 14

2.1.6 Electrochemical Characterization . . . 14

2.2 Silicon Anodes . . . 15

2.2.1 Emergence of Silicon as LIB Anode Material . . . 15

2.2.2 Pure Silicon Thin Film Anodes . . . 16

2.2.3 Silicon Alloy Anodes . . . 17

2.2.4 Silicon-Carbon Anodes . . . 18

2.2.5 Mitigation Strategies for Silicon Degradation . . . 18

2.3 Scanning Electron Microscopy . . . 19

2.4 Transmission Electron Microscopy . . . 21

2.4.1 Design and Operation . . . 21

2.4.2 Modes of Operation . . . 23
2.4.3 STEM . . . 24
2.5 Spectroscopy . . . 25
2.5.1 Energy-Dispersive X-ray Spectroscopy . . . 26
2.5.2 Electron Energy Loss Spectroscopy . . . 27

3 Methods **29**
3.1 Sample Preparation . . . 29
3.1.1 Plasma-Enhanced Chemical Vapor Deposition . . . 29
3.1.2 Cell Fabrication and Opening . . . 30
3.1.3 TEM Sample Preparation with FIB . . . 31
3.2 Electrochemical Characterization . . . 32
3.3 Electron Microscopy . . . 32

4 Results **35**
4.1 Samples . . . 35
4.2 Cycling Data . . . 36
4.3 Surface Morphology . . . 37
4.4 Physical and Structural Changes . . . 38
4.5 Chemical Results . . . 40

5 Discussion **47**
5.1 Sources of Error and Uncertainty . . . 47
5.1.1 Sample Preparation . . . 47
5.1.2 Measurement Uncertainty . . . 48
5.2 Characterization of Degradation Mechanisms . . . 49
5.2.1 Before Cycling . . . 49
5.2.2 After 3 Cycles . . . 51
5.2.3 After 1000 Cycles . . . 52
5.3 Consequences of Degradation . . . 56
5.3.1 Discussion of Cycling Data . . . 56
5.3.2 Comparing Cycling Data to Observations . . . 58
5.4 Utilizing Silicon Anodes in Full-Scale Full-Cell Batteries . . . 59

6 Conclusion **62**

7 Further Work **63**

Bibliography **64**

Appendices **i**

A Supplementary Results **ii**
A.1 SEM Images of Film Morphology . . . ii
A.2 SEM Images of TEM Lamellae . . . iii
A.3 TEM Overview Images of films with low magnification . . . iv

A.4 EDS Maps v
A.5 Quantitative EDS STEM Images xi

B Galvanostatic Cycling Parameters **xii**

C Linescan Smoothing code **xiii**

D Supporting Results from IFE **xiv**

CHAPTER 1

INTRODUCTION

Countries all over the world are struggling with the effects of global warming as a result of greenhouse gasses. The high consumption of fossil fuel-based energy must come to an end, and researchers are investigating more efficient ways of implementing cleaner and renewable energy sources [1]. The two most common types of renewable energy sources are wind and solar power, however, neither of them are capable of providing a continuous and predictable energy supply independently of uncontrollable conditions such as the weather. Solar energy is biased towards summer months and daylight, whilst wind power is only a viable option in regions with high/low-pressure zones [2]. Especially regarding wind power, countless favorable locations are preserved, not allowing the construction of wind turbines. Such challenges, unfortunately favor non-renewable energy sources. An advisable and already implemented solution is through the use of rechargeable batteries, which can store excess electrical energy and redistribute it at a later time [3].

Furthermore, looking into the continuous increase of portable electronic devices and the need for more sustainable and environmentally friendly transport solutions, the demand for more lightweight batteries with higher capacity and lifetime is increasing. The range of applications in need of storing electrical energy is enormous, ranging from laptops to electric vehicles (EV). The first mobile phone, Motorola's DynaTac 8000X was powered by a 500 mAh Ni-Cd battery which was drained by a 20-minute phone call and had to charge for 10 hours [4]. Modern smartphones such as the Samsung Galaxy S22 Ultra and iPhone 13 Pro are expected to last at least a full day of heavy use with their 4000-5000 mAh batteries. In terms of transport, there has also been much focus on converting to zero-emission energy solutions, such as battery-electric or hydrogen-driven motors. Batteries have been used in cars for many years, but not as the main power source for the car. With EVs, the battery is one of the limiting factors, as it takes up a large physical size and weight of the car, and usually comes with a significant price tag.

The lithium-ion battery (LIB) is perhaps the best option in terms of portable rechargeable

batteries [5–7]. Compared to its competitors, e.g. lead-acid, Ni-Cd, and Ni-MH batteries, LIBs offer several advantages. These include high specific energy, low self-discharge rate, high operation voltages, maintenance-free, lightweight, good safety, and excellent cycling stability [4]. Today's EVs are almost exclusively powered by LIBs, and the technology is growing in terms of popularity and performance. LIBs have increased their specific energy by almost 300% since the 1990's, and the cost has decreased significantly as well [8]. Additionally, LIBs are being applied to grid storage, which can be quite useful e.g. in the case of electrical blackouts [9].

In the pursuit of further improving the LIB, researchers have been looking into improving the components of the LIB cell. Graphite which has commercially been used as the anode material in most LIBs since their invention, suffers from a limited specific capacity of 372mAh g^{-1} [10]. Silicon has the last few decades become gradually more popular in research. With a roughly 10 times Li-ion storage potential than that of graphite, it is already being applied in some applications [11–14]. This thesis addresses the problems that at present stop Si-based materials from being utilized in LIBs, one of which being the mechanical instability introduced by the colossal volume expansion during lithiation [15, 16]. During cycling, a solid electrolyte interphase (SEI) is formed, which acts as a passivation layer on the electrodes. This layer is one of the main causes of the capacity drop in the first cycles of LIBs, but is favorable as it is ionically conducting and electrically insulating. During mechanical deformation of the silicon anode, crack formation is inevitable, exposing more silicon surface on which more SEI can form [17–20]. Increased SEI formation exacerbates the cycling instability, e.g. through Li-ion trapping, electrolyte consumption, and converting active material in the electrodes to inactive via irreversible reactions. Proposed solutions include various Si nanostructures to cope with the mechanical instability related to volume expansions, different coating strategies to enhance the structural stability of the SEI, and alloying of silicon with other elements to again improve the mechanical stability, to mention a few [2, 7, 9, 21–31]. The fundamental degradation mechanisms of Si-based anodes are one of the key elements that must be understood to be able to utilize these materials in future LIBs with improved gravimetric and volumetric energy density.

The approach chosen in this thesis is through characterization of thin film anodes with transmission electron microscopy (TEM). The use of thin films is primarily to understand the fundamental processes during cycling. Thin films are very useful for lab-scale testing, due to their easy production and low cost. For the same reason, they cannot provide a high total capacity for commercial batteries. They are primarily used to understand how degradation works. On the other hand, thin films are useful thanks to their lower expansion at the nanoscale, the good electrical conductivity of dense thin films compared to bulk, and the absence of binders. Si thin films can deposit onto about any shape, with the same techniques as for microdevice manufacturing. Also, the batteries can be made very thin [18, 22]. Use of TEM enables the determination of detailed insight in the micro and nano-sized regimes, where some of the most outermost important degradation mechanisms are located. TEM can also be combined with spectroscopy techniques, allowing further insight into the chemical composition of the anode.

CHAPTER 2

THEORY

2.1 Batteries

2.1.1 Early History

The first battery dates back to Alessandro Volta in 1800, with the generation of an electrical current, inspired by Luigi Galvani from a few years earlier [20]. This sparked an evolution of battery technology, eventually leading to the modern rechargeable LIB. The first generation of batteries, primary batteries, were non-rechargeable. These were discarded after their available chemical potential had been used to generate an electrical current. Improved primary batteries are still commercially used today in several applications, e.g. TV controllers, toys, and smoke detectors. In a nutshell, by sacrificing rechargeability they offer longer lifetimes and high capacities. The second generation of batteries, secondary batteries, arrived in 1859 with the invention of lead-acid batteries invented by Gaston Planté. These are still used today due to their cheap cost, high discharge currents, and low-temperature tolerance. The downside of lead-acid batteries, which still is the motivation for the development of new batteries is the pursuit of higher capacities and cycle lifetime. The LIB set the stage for a new level of battery performance in 1991, commercialized by Sony Corporation [4, 32]. Besides, it is generally preferable to reduce the usage of lead. Figure 2.1.1 shows a comparison of LIBs with other existing secondary battery technologies.

2.1.2 Working Principles

This section is heavily based on *Linden's handbook of batteries* by Reddy and Linden [33], and thus citations to their work are omitted.

Batteries are devices which convert the chemical energy stored in their components into electric

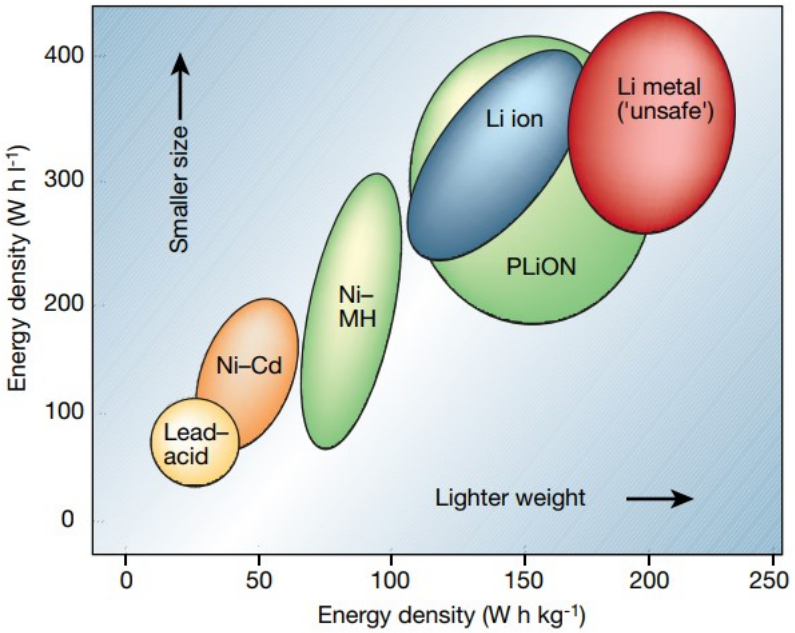

Fig. 2.1.1: Comparison of different secondary battery technologies by volumetric and gravimetric energy density [5].

energy, through electrochemical reactions called reduction-oxidation (redox) reactions. Redox reactions can also be non-electrochemical, e.g. corrosion, in which there is a direct transfer of electrons. A battery consists of one or more electrochemical cells connected in series, parallel or a combination, based on requirements for output voltage and current. A cell consists of a positive electrode, a negative electrode and an electrolyte. During discharging of a battery, the negative electrode is referred to as the anode and the positive electrode as the cathode. Throughout this thesis, the anode is the electrode which is oxidized during discharging, and vice versa with the cathode, which is reduced during discharging. The anode gives out electrons and ions in an oxidation reaction. The electrons are pushed through an external circuit, to the cathode. The electrolyte is an ionic conductor, typically water or another solvent with dissolved salts, providing a way for the ions from the anode to the cathode, where there is a reduction reaction. The external circuit which the electrons are forced through is in reality the application of the battery, e.g. powering a car. The electrons are pushed by an electromotive force from the electrochemical potential, E, which is given by the difference between the redox potentials of the anode and the cathode. The redox potential, divided into an oxidation potential and a reduction potential refer to a material's tendency to lose or acquire an electron, respectively.

It is common to distinguish between non-rechargeable and rechargeable batteries, which have previously been termed primary and secondary batteries, respectively. Primary batteries can be convenient as they are usually cheaper, lighter, have longer shelf lives, have high capacities, and require little maintenance. Shelf life refers to how long a battery can be stored without losing its capacity. Capacity refers to the material's or battery's ability to store electric charge, and will be discussed in further detail later in this section and throughout the thesis. Examples of applications for primary batteries are remote controllers, toys and smoke detectors. Secondary

batteries can be restored to their original charge state, by applying a reverse bias current, charging up the cell(s) in the battery. It is this class of batteries which will be investigated in this thesis.

For the specific case of LIBs, the "rocking chair" principle is often applied to explain the concept in a simple manner. In its simple form, the Li-ion electrochemical cell consists of an electrolyte, a separator, an anode, a cathode, Li-ions, and an external circuit connecting the anode and the cathode. This is illustrated in Figure 2.1.2. In a charged state, the Li-ions are hosted within the anode. When the external circuit is closed, electrons are free to flow through it, while Li-ions are conducted through the electrolyte. The ions go through the separator and are reduced at the cathode. When a reverse bias current is applied to the electrodes, electrons are forced back to the anode. The Li-ions diffuse back through the separator and the electrolyte, and lithiate the anode. The terms lithiation and delithiation of an electrode refer to when the electrode takes in, and when it sends out Li-ions, respectively. When the reverse bias is removed and the external circuit closed, the discharging process starts over again. This back-and-forth motion is referred to as the rocking chair.

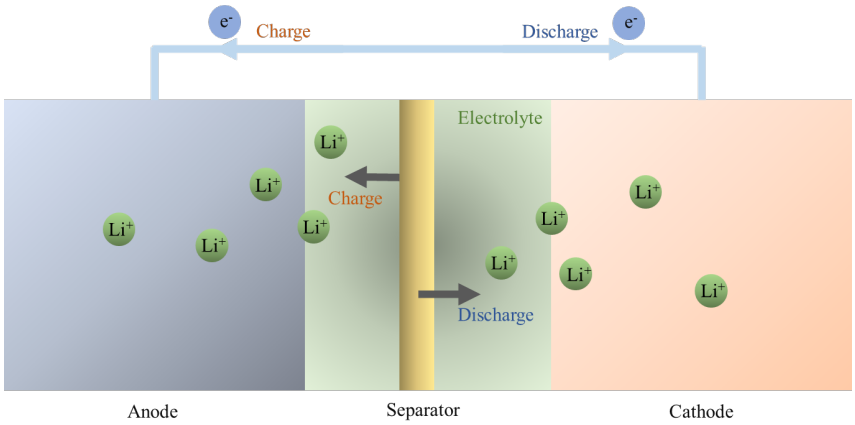

Fig. 2.1.2: Schematic showing the rocking chair principle in LIBs. The Li-ions go from the anode to the cathode during discharging, and the opposite way during charging when a reverse bias is applied. A real battery cell is more complex than this, e.g. the external circuit is connected to current collectors which are attached to the electrodes.

The capacity of a battery cell refers to the amount of electric charge it can store, and is determined by both operating conditions and the composition of the cell. Chosen discharge current, cut-off voltage and temperature during operation can affect the amount of charge the cell outputs [17]. The most considerable factor for the capacity is however the cell components, i.e. type of and amount of material. The unit for capacity is Ah. Specific capacity refers to the capacity per weight, and for portable LIBs, the unit mAh g^{-1} is commonly used. The total capacity of the cell Cap_{cell} is determined from

$$Cap_{cell} = \frac{1}{\frac{1}{Cap_A} + \frac{1}{Cap_C} + \frac{1}{Cap_M}}, \tag{2.1.1}$$

where Cap_A and Cap_C represent the capacity of the anode and cathode respectively. C_M represents the effective capacity of all remaining components in the cell. From Equation 2.1.1 it can be shown that an infinite increase in the specific capacity of one single component, can

only improve the total specific capacity of the cell up to a certain limit [18].

Irreversible capacity describes the amount of electric charge that is not restored and thus lost. For LIBs, irreversible capacity is primarily attributed to the loss of exchangeable Li-ions by Li trapping and Li forming irreversible phases. For Li trapping, Li-ions become stuck in the host material, which is not the same as irreversibly binding to SEI in the electrodes during cycling. However, both mechanisms lead to loss of lithium inventory, implying that the Li-ions become incapable of contributing to transferring charge. Loss of active material is another cause of irreversible capacity loss, as active material which stores Li-ions undergo an irreversible conversion and is inactivated. Thus, irreversible capacity refers to the difference between the lithiation and delithiation capacities. The irreversible capacity is typically high in the first cycles of a battery, called the formation-cycles which are covered more extensively in subsection 2.1.3. Capacity retention refers to how much of the initial capacity is retained after a certain amount of charge/discharge cycles.

Coulombic efficiency (CE) is another important parameter, which describes the ratio between the charge and the discharge capacities, Cap_{Charge} and $Cap_{Discharge}$, respectively. It can be determined by the equation

$$\eta_{CE} = \frac{Cap_{Charge}}{Cap_{Discharge}} \tag{2.1.2}$$

and resembles the reversible capacity in one cycle.

2.1.3 The Solid Electrolyte Interphase

During lithiation of the anode, Li-ions are transported through the electrolyte as complex cation solvent adducts, called solvate complexes. The solvent of the liquid electrolyte degrades at the anode due to the electrode's reductive nature, and the electrolyte's unstable nature at high and low voltages vs Li/Li^+. The solvent molecules detach from the Li-ions and decompose to form a passivation layer on the electrode. This layer is the solid electrolyte interphase (SEI) and is mostly formed during the first few cycles. The SEI is permeable for Li-ions, and electrically isolating, but first of all, it hinders direct contact of the solvent with the electrode [17, 18]. The LIB performance, i.e. reversible and irreversible capacity, rate capability, cyclability, etc. all depend on the quality of the SEI [19, 20]. To achieve a stable SEI, formation-cycles at lower C-rates, typically C/20 are run before the battery is used commercially.

C-rate refers to the rate at which the battery is charged and discharged. 1C indicates a charge/discharge rate at which it takes the cell one hour to complete a charge/discharge cycle. C/20 means it takes the cell 20 hours to complete the cycle. This value is calculated from the total capacity of the cell. As a cell initiates its cycling, it is common to use low C-rates in the first cycles, such that initial reactions can occur completely. These typically include SEI formation and structural changes of the electrodes. These normally three cycles are known as formation-cycles and consume typically up to ~ 10 % of the capacity of the cell. The formation-cycles are time and energy-consuming, and typically last a few days to a few

weeks [34]. Increasing the C-rate to speed up the formation-cycles is accompanied by negative effects such as non-uniformity in thickness and discontinuity of the SEI [34].

The composition and thickness of the SEI vary between batteries. The amount of and composition of electrolyte, anode material, and cycling procedure of initial cycles contribute to determining the SEI properties. The thickness and composition also vary during cycling and storage. Moreover, the SEI has a different thickness in the delithiated state, than in the lithiated state [35]. The actual structure of the SEI is not conclusively determined, and multiple theories have been presented. In general, it has a multilayered polycrystalline structure as seen in Figure 2.1.3 [36]. Depending on electrode materials and electrolyte composition, some common SEI phases are LiF, Li_xO, Li_2CO_3, LiOH and $Li_xSi_yO_z$. The latter is more specific for Si-containing electrodes.

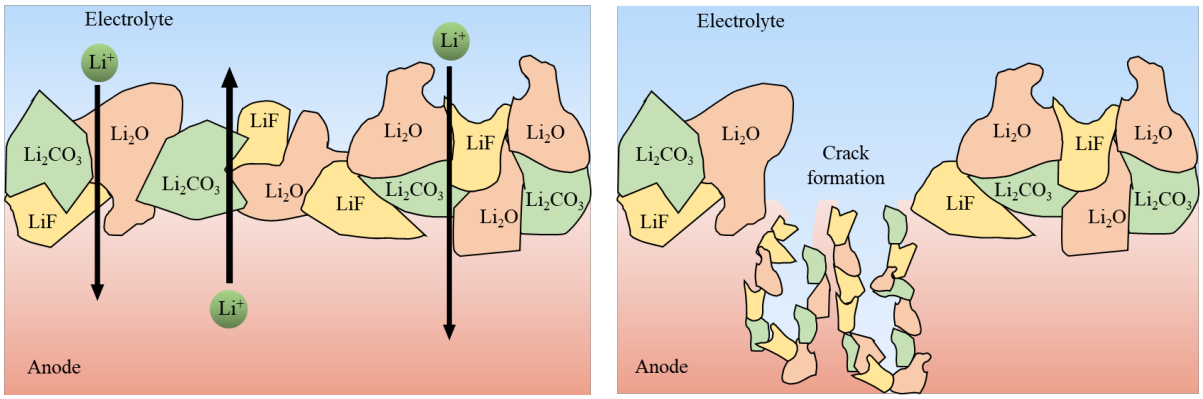

Fig. 2.1.3: Schematics showing the SEI structure on a thin film, and examples of possible components. a) The SEI separates the film from the electrolyte, but Li can diffuse through. b) Cracks in the anode, which allow the electrolyte to reach more film surface and form additional SEI.

Stability issues can cause delamination and cracking of the SEI, enabling additional electrolyte to come in contact with the electrode and degrade into SEI. The consumption of electrolyte and Li-ions worsen the performance of the battery through irreversible capacity loss. Volume expansion and contraction of the electrode during lithiation and delithiation is a substantial cause of cracking of the SEI. Graphite which has been commercially used in LIBs through the years, has a volume expansion of $\sim$ 10 %, while for silicon it can be as high as $\sim$400 % while lithiated [15, 16]. Several measures can be made to prevent cracking, by reducing volume expansions, increasing the adhesion between the film and the anode, and improving the SEI stability. These are covered in Sections 2.1.4 and 2.2.

Characterization of the SEI layer is often challenging, as it is highly reactive in ambient conditions [16, 37, 38]. In a study by Schroder et. al., the composition of the SEI was characterized by X-ray photoelectron spectroscopy (XPS) before and after exposure to ambient conditions, revealing compositional changes due to several chemical reactions associated with oxidation processes. This includes, among others, fluorinated products formed from the dissolution of LiF and degraded $LiPF_6$-products in the presence of water, and a general increase of oxygen-containing species related to Li-carbonate reacting with carbon dioxide and moisture in the air [16]. More specifically for silicon anodes, $Li_xSi_yO_z$ can also form [38]. Cycled anodes should

therefore be transported via an inert transfer chamber, to avoid exposure to normal atmosphere. For further reading on SEI, the reader is advised to check out the book *Lithium-ion batteries: solid-electrolyte interphase* by Balbuena & Wang [36].

2.1.4 Main Components

The main components of every battery are the anode, the cathode, and the electrolyte. Most batteries include additional components, and their composition vary depending on application and requirements. It is gradually becoming more popular to use the names negative and positive electrode, for anode and cathode, respectively. This is because the terms anode and cathode refer to the occurring reactions at the electrodes, and therefore switch depending on whether the electrochemical cell is being charged or discharged. As mentioned previously, this thesis will use the terms anode and cathode, simply because it has been the convention for many years. Below is an attempt to illustrate the naming of the electrodes through an example. Take the following reactions [39]:

$$\begin{aligned} \mathrm{Cu}^{2+} + 2\mathrm{e} &\rightleftharpoons \mathrm{Cu}, & E^0 &= 0.34\mathrm{V} \\ \mathrm{Zn}^{2+} + 2\mathrm{e} &\rightleftharpoons \mathrm{Zn}, & E^0 &= -0.76\mathrm{V} \end{aligned}$$

where Zn is the strongest reducing agent and is therefore named the positive electrode as it is more likely to be reduced, i.e. receiving an electron. This will always be the case in this cell, and vice versa with Cu being the negative electrode. During discharging, which is a spontaneous reaction, the negative electrode is oxidized and the positive electrode is reduced. Per definition, the negative and the positive electrodes are named the anode and cathode, respectively. During charging, a reverse bias current is applied to the system, reversing the reactions. Now, the positive electrode is the anode, and the negative electrode is the cathode. This is also an example of the rocking chair principle which was explained in subsection 2.1.2

Anode

Lithium metal anodes: Lithium is very light, has an exceptionally high capacity (3860 mAh g^{-1}) and a strongly negative potential, nominating it to be a very suitable anode for rechargeable and portable batteries. Ideally, the anode of secondary batteries would have been a metallic lithium plate, which was initially the case [40]. A Li anode implies that the anode material is metallic lithium, contrary to LIBs where another material is used to store Li-ions through intercalation or alloying. Li redeposits during cycling and forms dendrites, which is a great challenge that must be overcome before using metallic Li as anodes. This is due to concentration gradients in the liquid electrolyte, that prefer re-deposition of Li in specific regions, especially at lower voltages. These spike-formed dendrites can in the worst case penetrate the separator and short circuit the cell. Quick discharges could potentially cause an internal thermal chain reaction, further leading to fire and explosions [17, 18, 40, 41]. Lithium metal anodes are constantly revisited, to better understand the degradation mechanisms and commercialize them [42].

Criteria for LIBs: Instead of using pure metallic lithium, secondary batteries rather rely on materials that store Li-ions via intercalation/deintercalation or alloying with Li. Here are some criteria which should be fulfilled for such materials [43]:

1. Lightweight and able to accommodate as much lithium as possible, to maximize the gravimetric capacity.
2. Redox potential should be as low as possible vs Li/Li^+, independently of the lithium concentration.
3. Have high electronic and ionic conductivity to yield high power density.
4. Cannot be soluble in the electrolyte, and cannot react with the Li salt.
5. Must be safe in terms of environmental friendliness, toxicity and other hazards.
6. Cheap and readily available.

Carbon and graphite anodes: Since the invention of LIBs, graphitic carbon has almost exclusively been used as anode material in commercial applications. Graphite is cheap, readily available and has excellent cycling stability. At maximum intercalation of Li in graphite, it reaches a chemical composition of LiC_6, yielding a theoretical capacity of 372 mAh g^{-1} in ambient conditions [10]. This process forces the graphite to expand along its c-axis with ~ 10 % [15]. Graphite has an electrochemical potential of 0.25 V versus Li/Li^+. Other form factors of carbon have been and are still being investigated to increase this capacity. There are two main classes of carbon which may be used as active material in LIBs: hard carbons, and soft carbons. The latter refers to carbon structures in which its crystallites are almost all oriented in the same direction. In hard carbon, the crystallites have more random orientations. Both types have been used in LIBs. In short terms hard carbon struggles with rate capability due to slow diffusion processes, because of the many voids associated with the randomly oriented crystallites. Soft carbons have long cycling life and high CE, whereas graphite is an example of a soft carbon [43]. Other carbon polymorphs, such as carbon nanotubes, graphene and surface-modified carbons can introduce additional qualities such as greatly increased electronic conductivity and flexibility but are challenging in terms of commercial production.

Alloying anodes: Graphite and nearly all cathode materials store Li-ions through intercalation into interstitial sites in the host lattice, such that minimal strain and structural changes are imposed onto the host. These materials exhibit good cycling stability over many cycles but suffer from low specific capacity due to the limited number of intercalation sites for Li-ions. Alloying materials such as Si, Ge and Sn host Li-ions through a different lithiation mechanism, in which they are capable of reversibly forming an alloy with the Li-ions. The alloying process involves breaking the inter-atomic bonds in the host material, forcing structural changes. Because the atomic framework of the host material does not oppose volumetric constraints on the reaction, a much higher specific capacity is achievable [17, 20, 33, 44, 45].

The major volume changes during lithiation and delithiation worsen the cycling stability. Irreversible reactions during lithiation, e.g. SEI formation, and irreversible alloying prevent the

host material from returning to its initial shape during delithiation. This causes internal strains. This process is visualized in Figure 2.1.4 for the case of thin film electrodes. To relax the strained structure, crack formation occurs. Cracks can also form because Li enters and disappears through the film-electrolyte interface with different rates at different locations [44, 46–48]. Cracks in the electrode expose new surfaces on which the electrolyte can react with the electrode and form additional SEI, as was illustrated in Figure 2.1.3. The described process is responsible for the loss of active material, followed by a reduction of CE. Furthermore, alloy anodes suffer from potential hysteresis between charging and discharging, which is the difference between lithiation and delithiation potentials when a constant current is applied. The hysteresis can be mitigated by using catalysts and surface coatings [44, 45, 49–51].

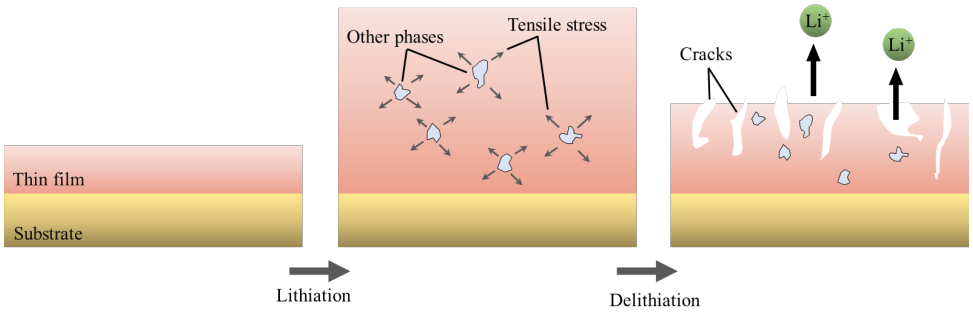

Fig. 2.1.4: Schematic showing volume changes of thin film anodes during lithiation and delithiation, which result in crack formation. During lithiation, alloying between the active material and Li imposes stress on the surrounding electrode material. Some of the alloy phases are irreversible and prevent an isotropic contraction of the material during discharging. The stress is released through crack formations seen in the figure to the right. Li-ions are seen going out from the contracting film, leaving additional holes. Dimensions are not to scale.

Besides Si, which will be covered in section 2.2, other group-14 elements, e.g. Ge and Sn are potential anode material candidates. Ge exhibits impressive electronic conductivity and lithium diffusivity. In theory, it has a lithium saturated phase $Li_{22}Ge_5$ with a theoretical specific capacity of 1625 mAh g^{-1}, but in reality, its $Li_{15}Ge_4$ phase is formed, with a capacity of 1385 mAh g^{-1} [52]. Another desirable feature of Ge as an anode for LIBs is its mechanical stability during cycling. As it delithiates, it has been found to form a nanoporous amorphous phase. This process is isotropic, and even at very high C-rates, it is not vulnerable to crack formations [53, 54]. The downside with germanium is its high price, making it less attractive for mass production. An additional challenge is finding suitable cathode materials, to be able to draw advantage of the high C-rate capability. So far, the phosphate $LiFePO_4$ is a viable option, but it suffers from limited capacity [43]. Sn provides a decent theoretical capacity of 960 mAh g^{-1}, but similar to many other metal anodes, it undergoes large volume expansions during lithiation. To mitigate the volume expansions, Sn anodes have been made with microstructures such as Sn-filled nanotubes or nanofibers, or by making metal composites. Some attempts have almost succeeded in achieving theoretical reversible capacity, but have been complicated to produce, making them less suited for commercial applications [55]. Other elements such as Al, Bi and Mg are also capable of reversibly alloying with Li, and have been studied as alternative replacements for graphite by Zhang [51], who presented a comparison of the theoretical specific capacity, volume change, and other key parameters of alloy anodes.

Oxide anodes: A new class of promising anode materials is oxides with intercalation-deintercalation

reactions and oxides based on alloying/de-alloying reactions. Titanium oxides, especially $Li_4Ti_5O_{12}$, commonly known as LTO offer low cost, environmentally friendliness, mechanical stability, and thermal stability. For these reasons, it is seen as more suitable for the growing markets of large-scale electrochemical storage and EVs, than carbon/graphite. A drawback of LTO is its poor electric conductivity and high operating potential. Current research is working on further improving rate capability and cycling stability, but suggested solutions so far are seemingly too complicated and cost-effective to be commercially favorable [43, 56].

Silicon oxides were first thought to be electrochemically inactive, and to only provide a buffering matrix for the volume changes of pure silicon during cycling, but have later been shown to contribute to the capacity of LIBs [57–59]. Thus, they have in some cases been adopted by industry for commercial use, but as part of a larger composite [60–62]. Pure SiO_2 is shown to have poor electrochemical activity because of inefficient Li-ion diffusion and poor intrinsic conductivity. However, attempts of reducing SiO_2 particle size and creating a composite with carbon have shown improved results [59, 62, 63]. The perhaps biggest issue with silicon oxides is the very low initial CE, caused by the generation of Li_2O and lithium silicates during the formation-cycles [62].

Conversion anodes A final class of potential anode materials is conversion materials, which react reversibly with lithium according to the reaction $M_aX_b + (b \cdot n)Li \longleftrightarrow aM + bLi_nX$, in which M=transition metal, X=anion, n=formal oxidation state of X. The metal can for example be Ti, V, Cr, Ge, Co, Ni, Cu, Mo, W or Ru, while the anion can be O, S, N, P or F. With the many possible combinations of transition metals and anions, a range of operating voltages can be chosen. The major downside of conversion materials is caused by the particle reorganization during cycling, leading to pulverization and loss of electrical contact, which strongly affect the cycle lifetime. Additionally, conversion materials experience potential hysteresis [64].

Cathode

The magnitude of the cell voltage in a battery varies depending on the redox potentials of the anode and the cathode materials. Ideally, the potential difference between the electrodes should be as high as possible. Cathodes have traditionally contained one or more transition metals, due to their multiple stable oxidation states [18]. Cathodes can be classified into three classes: layered oxides, spinels and phosphates [17].

Layered oxides: An early and highly popular example of layered oxides is $LiCoO_2$, which has a distorted rock-salt structure [65, 66]. The significant size difference between Li^+ and Co^{3+} yields favorable cation ordering, facilitating fast 2D Li diffusion. Along with structural stability, $LiCoO_2$ provides high charge/discharge rates with good reversibility, and operating voltages up to ∼4 V. A downside of layered oxide cathodes is limited capacity, and the high cost of Co, which was the motivation for $LiNi_{1-y-z}Mn_yCo_zO_2$. Mn can offer improved chemical stability and is more environmentally friendly, while Co has higher structural stability and electrical conductivity. Ni has intermediate properties between the Mn and Co [67–69]. Other $LiMO_2$

layered oxide materials, where M=3d transition metals, such as V, Mn and Fe can also be synthesized with direct high-temperature reactions but may struggle with structural stability during cycling [70].

Spinel oxides: Motivated by successful Li insertion into spinel structured magnetite, spinel oxides attracted attention as a possible LIB cathode material [71, 72]. Spinel oxides have the chemical formula LiM_2O_4, where M very often is Mn, but may also be Ni, Ti or V. Unlike the layered oxides, the spinel structure offers a 3D lithium diffusion pathway. This permits even higher charge/discharge rates and reversibility while keeping the ~ 4 V operation voltage, but with lower capacity. A notable disadvantage of $LiMn_2O_4$ in particular, is the dissolution of Mn into the electrolyte, contributing to capacity-loss and reducing cycle life [73–75]. Alternative spinel oxides are $LiTi_2O_4$ and LiV_2O_4 as they also have stable $M^{3+/4+}$ oxidation states but suffer from limited voltage windows [69, 76].

Phosphates: The third class, phosphates, have the chemical formula $LiMPO_4$ in which M is a transition metal. $LiMPO_4$ phosphates have an olivine structure with M at the octahedral sites, phosphorus at the tetrahedral sites, and Li as 1D chains along the [010] direction [66, 77]. The most common phosphate for LIB cathodes is $LiFePO_4$, partly because it has a miscibility gap between $FePO_4$ and $LiFePO_4$. This causes the delithiation to occur through the growth of two phases, which essentially yields a flat discharge curve [66, 78]. Other phosphate alternatives include $LiMnPO_4$ and $LiCoPO_4$, which have higher open-circuit voltages but fall short in terms of lower capacity. Additionally, both phosphates have been seen to degrade into MnP_4O_7 and CoP_4O_7, which degrade the battery lifetime and introduces safety concerns, due to oxygen development [79–82].

As cathode materials are not the main focus of this thesis, the reader referred to *Lithium-ion batteries: basics and applications* by Korthauer and *A reflection on lithium-ion battery cathode chemistry* by Manthiram for supplementary reading [17, 69].

Electrolyte

This section about electrolytes in LIBs is heavily based on *Lithium Ion Batteries - Basics and Applications* by Korthauer [17], and thus citations to this book are omitted.

The function of an electrolyte in a LIB is to conduct Li-ions from one electrode to the other, while at the same time being electrically insulating. There are several requirements which electrolytes must fulfil. The electrolyte must have a high conductivity for Li-ions across a wide temperature range while at the same time having a low electronic conductivity relative to the ionic conductivity. It must have cycling stability over thousands of cycles, and be chemically and electrochemically compatible with the other components in the battery cell. Moreover, it should be cost-efficient for large-scale production and non-toxic. There are three classes of electrolytes, differentiated by their physical characteristics; liquid electrolytes, solid electrolytes, and ionic liquids.

Liquid electrolytes: These typically consist of two main components; a combination of solvents and a conducting salt. The solvents must dissolve the conducting salt and provide low viscosity, for the salt to be transported. The solvents should have a low melting point and high boiling point, be inert towards other cell components, and satisfy safety issues, e.g. toxicity. They should also be economically favorable. Inertness towards other components is a major challenge for LIBs with Si anodes. Ethers and esters, especially organic carbonates, are very popular as solvents, due to their aprotic and highly polar nature. The anode and cathode materials used in LIBs are usually very oxidizing and reductive, respectively, which promotes the development of hydrogen from solvents with an active acidic compound. Ethylene carbonate (EC) is currently the most used solvent for LIBs with a carbon-based anode, because it exhibits high quality SEI formation and high permittivity. However, as it also has a high melting point, it is typically combined with dimethyl carbonate (DMC), diethyl carbonate, ethyl methyl carbonate (EMC) and/or esters. In terms of conducting salts, they should have high solubility in the solvent, chemical and electrochemical stability, and good compatibility with other cell components. The most common salt used in electrolytes is lithium hexafluorophosphate ($LiPF_6$). It has been used since the '60s and is almost the only one used in commercial LIBs. $LiPF_6$ offers high conductivity at room temperature, electrochemical stability up to $\sim$5 V vs Li/Li^+ and good compatibility towards other cell components. On the other hand, the salt suffers from being thermally unstable, as it degrades above 70°C and risks forming hydrofluoric acid in contact with water.

Solid electrolytes: The innovation of solid electrolytes was inspired by the volatility and flammability of organic solvents in liquid electrolytes. Solid electrolytes are commonly classified into organic and inorganic. Organic solid electrolytes are commonly polymer and gel-polymer-based electrolytes. These involve a Li salt which is dissolved in a polymer host. They are simple in construction and regarded as a safer option than many other electrolytes e.g. due to resistance to short-circuiting and less prone to leakage. On the downside, they suffer from a relatively lower ionic conductivity. Inorganic solid electrolytes may be divided into glass-based and crystalline, e.g. ceramic electrolytes which typically have near-liquid electrolyte conductivity but suffer from stability issues. Ceramic electrolytes can often act as both electrolytes and separators [18, 83].

Ionic liquids: Ionic liquids are typically organic salts, also known as molten salt, and have low melting points, i.e. below 100 °C. Room-temperature ionic liquids have been acknowledged in previous studies for their near excellent properties such as thermal and chemical stability, tunable structure over a wide range of operating temperatures, broad electrochemical stability-window, high ionic conductivity at room temperature and non-flammability. Furthermore, they have essentially negligible vapor pressure near room temperature. They are therefore regarded as highly applicable for LIBs and other electrochemical energy storage devices [84–87].

There is yet to be made a perfect electrolyte for every application. The different classes of electrolytes can offer desirable properties for some applications while being unsuitable for others. As an example, the requirements for mobile phone batteries are not the same as for EVs.

2.1.5 Cell types

About all LIBs are made up of the same components, i.e. anode, cathode, current collectors, electrolyte and often a separator. These components can be assembled in form factors, depending on the application of the battery. The three most common cell types are cylindrical, prismatic and pouch cells. The cylindrical cells have good retention against expansion when fully charged, due to their shape, but are somewhat challenging to stack up compactly in a large battery pack. The prismatic cells are often encased in a hard plastic case and are excellent for compact designs. They do require retaining plates to resist expansion when fully charged, but are popular for their practical form factor. Pouch cells are contained in a soft bag, and thus also need retaining plates to resist expansion when fully charged. Due to their soft casing, they have fewer applications, but offer high energy density and are appropriate for large production runs. Pouch cells are often made with semi-solid gel-polymer electrolytes [18, 88].

A fourth cell type is the coin type cell, very often found in the 2032-format (20 mm diameter and 3.2 mm thickness), and sometimes also referred to as button cells or watch batteries. Typical applications of such batteries are watches, remote controllers and bathroom weighing scales. These cells are small and thus require only a little amount of anode, cathode and electrolyte material. For this reason, they are also cheap. Their coin-shaped geometry and cheap price make them suitable for research applications such as electrochemical testing. Commercially they are almost exclusively available as primary lithium metal batteries.

2.1.6 Electrochemical Characterization

Several testing strategies can be applied to investigate the electrochemical properties of a battery. Independently of technique, the only parameters which are measured are the voltage across the cell, the current through the cell, and the elapsed time. From these, the power, capacity, energy, CE and energy efficiency of the cycled cell can be determined. Additionally, with the electrode mass and volume known, the specific volumetric power, capacity and energy are found. During testing, it is common practice to construct half-cells, i.e. the counter electrode is a Li metal disc. A stable and practically infinite Li reservoir assures that the counter electrode potential is kept constant, such that any change in cell potential and capacity is attributed to the working electrode. Note, however, that in half-cell configurations with a Li metal electrode, the working electrode which is being characterized will always be the cathode because of the low working potential of Li. A potential downside of the endless supply of lithium is the exclusion of loss of Li inventory as a cause of irreversible capacity. In full-cells which have a limited amount of Li-ions, loss of Li inventory is perhaps the largest contribution to capacity loss.

Galvanostatic cycling, which is one of the most basic and frequent forms of electrochemical testing, works by charging and discharging a battery cell with constant current density between two predetermined cut-off voltages and determining the capacity fade over time. This technique offers useful information about the cyclability and durability of the investigated material, and the stability of the electrochemical cell. The C-rate has a major influence on the results, e.g.

the measured capacity which is lower for higher C-rated. This is because with higher charging and discharging rates, the Li diffusion kinetics are insufficient to lithiate and delithiate 100 % of the active material, yielding a lower measured capacity. This is the only electrochemical characterization technique used in this thesis [18, 89].

Other testing methods such as rate capability testing, cyclic voltammetry, potentiostatic cycling and differential capacity analysis can also be employed. The latter, also known as dQ/dV, is another testing strategy where the capacity is differentiated as a function of voltage. This technique is useful for finding the amount of charge which passes through the cell at a given voltage, i.e. at which voltages the electrode materials are active.

2.2 Silicon Anodes

2.2.1 Emergence of Silicon as LIB Anode Material

Silicon was first investigated for the storage of electrochemical energy by Sharma and Seefurth in 1976 [90, 91]. They published about the formation of Li−Si alloys for cells operating at ∼380°C - 480°C. The Li−Si alloys were found to be reversible with current efficiencies above 95 %. The four Li-rich phases $Li_{12}Si_7$, $Li_{14}Si_6$, $Li_{13}Si_4$ and $Li_{22}Si_5$ were confirmed in the Li−Si system, whereas the latter generates a gravimetric capacity of 4200 mAh g^{-1} [92]. While this is confirmed in later publications, it does not hold for room-temperature conditions. It was later found by Obrovac and Christensen, through XRD studies, that the metastable $Li_{15}Si_4$ with a theoretical specific capacity of 3579 mAh g^{-1} is formed instead [93, 94]. The described phases are seen in Figure 2.2.1 but note that this phase diagram only shows crystalline phases in equilibrium, which is not necessarily the case for amorphous Si and its metastable phases with Li. The $Li_{15}Si_4$ phase has roughly ten times the capacity of graphite, at 372 mAh g^{-1}. Another beneficial property of Si is its low electrochemical potential at 0.45 V versus Li/Li^+, enabling high open-circuit voltages. Besides its electrochemical properties, silicon is one of the most abundant elements in nature, making it cheap and readily available [95–98]. With all these traits Si has therefore been considered as a replacement for graphite as an anode material for LIB. Running up to the 2000s, only a handful of publications regarded Si as an anode material, including Si thin films, alloys and Si/C composites [92].

In terms of drawbacks, Si is subject to a ∼400 % volume expansion during lithiation, which induces a massive strain [16, 46, 100]. The expansion is caused by the formation of metastable amorphous Li-Si phases which take up more volume than the initial Si [45]. When Si approaches its fully lithiated state $Li_{15}Si_4$, the inter-atomic bonds between Si atoms are mostly broken, forcing atoms to relocate. This is one of several addressed causes for why the contraction during delithiation does not result in the electrode's initial shape. For thin films, the expansion is mostly perpendicular to the silicon surface, as expansions in the parallel directions are mitigated by the adhesion to the substrate [44, 46]. As a consequence of the mostly one directional expansion, atoms in the film move a longer distance during expansion and contraction, than for a three-dimensional expansion, resulting in larger structural reorganization. Otherwise the expansion

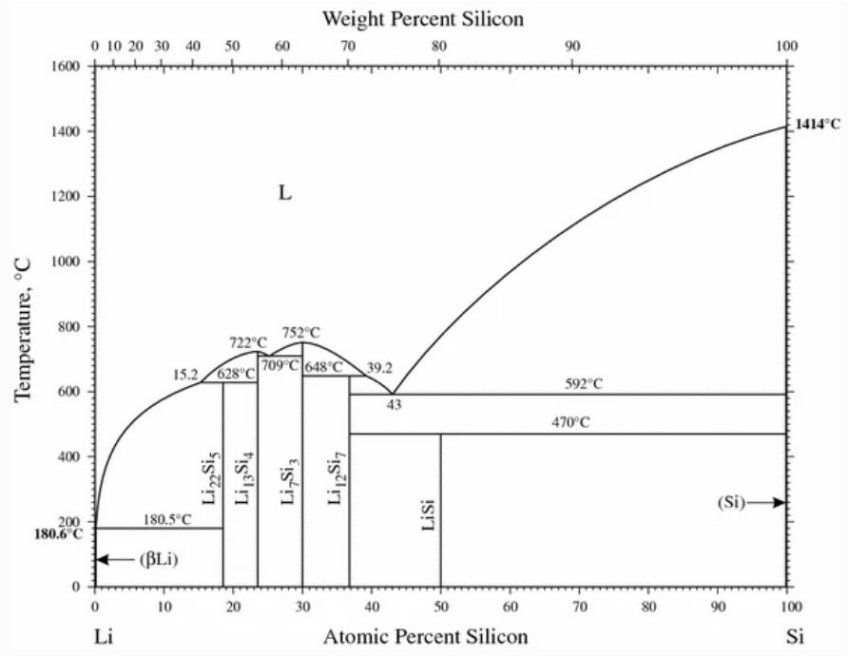

Fig. 2.2.1: Lithium-silicon phase diagram [99]

can be assumed to be isotropic, as there are no underlying crystallographic orientations making anisotropic growth preferential in amorphous Si. Si nanoparticles expand in all three dimensions, such that the translation of each atom is shorter, for the same volume expansion. Due to the strains imposed by the volume changes, cracking occurs to release the internal pressure. New electrode surface is exposed to electrolyte during cracking, such that additional SEI can form, as was seen in Figure 2.1.3. This consumes both active material and electrolyte, causing irreversible capacity. Multiple approaches to overcome the large volume expansions of Si have been studied. Some of the strategies are through the use of micro and nano-structured features, dispersing Si in an active or inactive matrix, and by the use of thin films [45]. The latter is described in further detail in the next section. The working potential for the formation of Li_xSi is outside the stability window of most electrolytes, which accelerates the formation of a SEI layer in the interface between the electrode and the electrolyte.

2.2.2 Pure Silicon Thin Film Anodes

Research on Si thin films as potential anodes for LIBs emerged in 1999, with low-pressure CVD deposited amorphous silicon thin films. With only 20 % capacity retention after 20 cycles, the new thin films were not very promising, part of the reason being poorly chosen cutoff potentials [22,92,101]. In 2003 radio frequency magnetron sputtered Si thin films were deposited with thicknesses of 250 nm and 1 µm on Cu foil. These films were able to retain a capacity of up to 3500 mAh g^{-1} for 30 cycles [102]. Later studies showed a relation between decreasing film thickness and increased specific capacity. Capacities up to 4000 mAh g^{-1} were measured, but with insufficient cycling stability [103–107].

The lithiation mechanisms in amorphous Si thin films have been studied to understand the

limiting factors, crack formation and volume expansion. As already explained in section 2.1.4, lithiation of Si works by the formation of Li_xSi phases, rather than intercalation of Li-ions into interstitial sites. The lithiated Si phases take up a larger volume, causing the film to expand perpendicularly from the surface. As the concentration of Li-ions surpasses the Si concentration, inter-atomic Si bonds are broken. This combined with significant volume expansions provoke structural changes in the thin film [44]. Bordes et al. [47] investigated Li insertion mechanisms of a thin-film Si electrode and found that in the first cycles, up to 10 % of the Li from the electrolyte is consumed by the formation of the SEI. After around 30 % lithiation, after the SEI has stabilized, then Li insertion becomes the main source of Li consumption, used to form the $Li_{15}Si_4$ alloy. Furthermore, they proposed a lithiation mechanism in which fast diffusion paths are formed in the Si active material. This also corresponds with a kinetic study, where they found that the initial lithiation occurs through the propagation of a new phase from the electrolyte-film interface to the film-substrate interface. Testing with potentiostatic techniques revealed that in the voltage range 360mV-600mV, the rate-limiting step was the diffusion of Li in the newly formed phase, and not the phase formation itself [108].

Substrate and film structure and morphology also play a major role in terms of anode performance and stability. Crack propagation in the film is a significant reason for capacity fade, as explained in subsection 2.1.3, and several proposals for solutions have been suggested. First of all, amorphous films have shown better performance than nanocrystalline thin films, as they provide better capacity retention and lower irreversible capacity loss. Cutoff voltages near 0.0V vs Li/Li^+ may induce crystallization of the amorphous lithiated Si phase, which impairs subsequent Li extraction during delithiation [21, 93, 104]. Roughening the film surface provides increased contact area and also yields better performance. This can be done mechanically, e.g. with sandpaper, or chemically, e.g. with an aqueous solution of $FeCl_3$ [21, 107]. Introducing patterns with smaller features than the average crack size has also shown to be effective in reducing cracking and improving mechanical stability. An example is the Lozenge pattern, produced by masking a substrate during deposition, published by Cho et al. [109]. The patterning allowed for enhanced capacity retention, stress suppression and increased overall mechanical stability. Furthermore, 3D patterns such as trenches and honeycomb wall structures, typically made with lithography techniques demonstrated even better performance, partly due to the increased surface area [22, 110–112].

2.2.3 Silicon Alloy Anodes

By introducing other elements into the anode material, its performance can be enhanced in terms of mechanical stability and improved CE, to mention a few. Introduction of additional components to silicon anodes, has the purpose of controlling the significant volume expansion, increasing the electrical conductivity, and increasing the stability of the SEI layer [2]. One typically divides added components into Li-active and Li-inactive components. Li-active components actively store Li during lithiation/delithiation, while Li-inactive components are not electrochemically active with Li, and can not store Li. The sole purpose of the latter is increased mechanical stability and long–term performance. Some examples of active materials are

Al, C, Sn, Ag, Mg and Ge, while examples of inactive materials are Ti, Mo, Va, Fe, Cu, Cr and Ni [113]. A review article by Salah et al. [2] gives a good overview of some of these materials. For the sake of relevance and space, this thesis will focus on carbon.

2.2.4 Silicon-Carbon Anodes

Graphite differs from Si because lithiation/delithiation works through intercalation/deintercalation instead of alloying, thus resulting in better mechanical stability but worse specific capacity than Si. As mentioned previously, carbon in the form of graphite is the commercially used anode material, and its properties are well studied. In the case of thin films, carbon can be combined with silicon as a multilayered structure, composite or alloy [114]. The latter is the case for the substoichiometric silicon carbide (SiC_x) thin films which are studied in this thesis. Other non-thin film examples are coating for silicon nanoparticles or nanowires. Moreover, SiC formation happens spontaneously due to the strong bonding tendency between Si and C. Previously SiC was regarded as an inactive material. It has been discovered recently that SiC can demonstrate high reversible capacity in LIBs, sparking research in this field [115, 116]. Efforts have been put into the designs of varying anode materials by combining Si and C in varying ways [2, 22, 117–121]. They show promising results, but their results are not comparable enough to optimize the commercial production of SiC anode materials for LIBs. In summary, they found that adding C to silicon mitigates the Si volume expansion during cycling, which further stabilizes the SEI. C also increases the charge/discharge rates by improving the Li-ion kinetics and electrical conductivity. For C coatings and layers, it can even serve as a protective film for the Si, hindering the electrolyte to come in contact with Si. Lastly, C may reduce Si thin film oxidation, and thus enhance cycling performance [2].

2.2.5 Mitigation Strategies for Silicon Degradation

This section presents potential strategies and solutions to prevent the degradation of Si anodes in LIBs. Many degradation mechanisms have been addressed in previous works [2, 21, 22, 44, 45, 51, 122]. The mechanisms of particular interest are SEI growth and mechanical deformations such as cracking, which exacerbate degradation related to further SEI formation. Since thin film anodes are not yet a realistic alternative in commercial applications, the solutions presented below will regard other more practical and application-oriented form factors, e.g. nanoparticles, and other nano-sized structures.

Concerning the lack of mechanical stability and crack formation, nanosized features seem to offer multiple advantages [3, 123]. Nanosized particles are seen to limit fracture and pulverization. In an article by Liu et al., it was found that stored strain energy from electrochemical reactions is insufficient to drive crack propagation in Si nanoparticles if the particle diameter was below 150 nm [124]. Nanoporous anode designs are also seen to improve resistance towards fracture and mechanical stress. Similarly to yolk-shell and core-shell structures, the voids in nanoporous structures allow the Si to expand upon lithiation, which in terms leaves stable SEI and improves

the performance [125, 126]. The problem with nanoporous Si anode designs is that they are not cost-effective due to fabrication prices and challenges of scalability [127].

Tackling the challenges related to continuous SEI formation, and thus consumption of Li-ions and active material, multiple strategies are already proposed. Various coatings have been tested, with the intention of mitigating SEI formation, to enhance cycling stability and initial CE. $LiAlO_2$ coating around silicon particles is observed to act as an artificial SEI layer, which mitigated Li trapping. The coating was seen to have good Li-ion conductivity, which enhanced Li diffusion into the Si nanoparticles. A further consequence of the coating was reduced electrolyte decomposition [7]. Other coating strategies include carbon, silicon carbide, and metal oxides such as Al_2O_3 and TiO_2 [3, 22, 128–133]. Carbon coatings have been observed to stabilize the Si-electrolyte interface and promote the formation of stable SEI to extend cycle life, as well as improved lithiation kinetics [3, 132, 133]. Silicon carbide coatings have also been shown to enhance the kinetics of lithiation in mesoporous Si electrodes, which is beneficial for fast charging and discharging of the battery [128]. The benefits of coatings must also be seen in terms of scalability, cost and available technology. Some coating procedures are complex, making them a less viable option, and this must be accounted for. In general, the requirements for a coating should be that it is elastic enough to not crack as the active material expands during lithiation, and which satisfies the criteria of high Li-ion conductivity while isolating the electrolyte from the active components. The final goal would be to enhance the CE, by reducing the loss of active material and loss of Li inventory. For Li metal electrodes, a coating of hollow carbon nanospheres helped isolate Li metal deposition and facilitate the formation of a stable SEI. Additionally, the coating reduced the Li dendrite formation up to a certain current density [134].

A predictable route for precisely controlling and adjusting the oxygen content in the Si may improve the performance of Si anodes. The O content directly affects the electrochemical properties, electrical conductivity and structural stability of the silicon [135]. There is sadly a discrepancy in the appropriate O content in Si anodes, which likely is caused by unmatched particle sizes, electrode morphology, other cell components and test conditions between the studies [136, 137]. Additionally, through an irreversible reaction, oxygen forms LiO_x during the first lithiation, which is observed to reduce the first cycle CE [123].

2.3 Scanning Electron Microscopy

Scanning electron microscopy (SEM) is a characterization technique applied to study the microstructure of the surface of a specimen by scanning it with a focused beam of electrons. The electrons are drawn from a filament by applying a strong electric field and or heating the filament until electrons are fired out from it. This is called an electron gun. Figure 2.3.1 gives a schematic representation of the components of a SEM. The condenser lens has the task of collecting the emitted electron radiation to a narrow beam, which is sent through the condenser aperture. The apertures are thin metal plates with a small hole, blocking electrons with an undesired angle. The scan coils deflect the focused beam in x and y -directions, scanning across the sample. The objective lens fine focused the beam into a probe which eventually hits the sample.

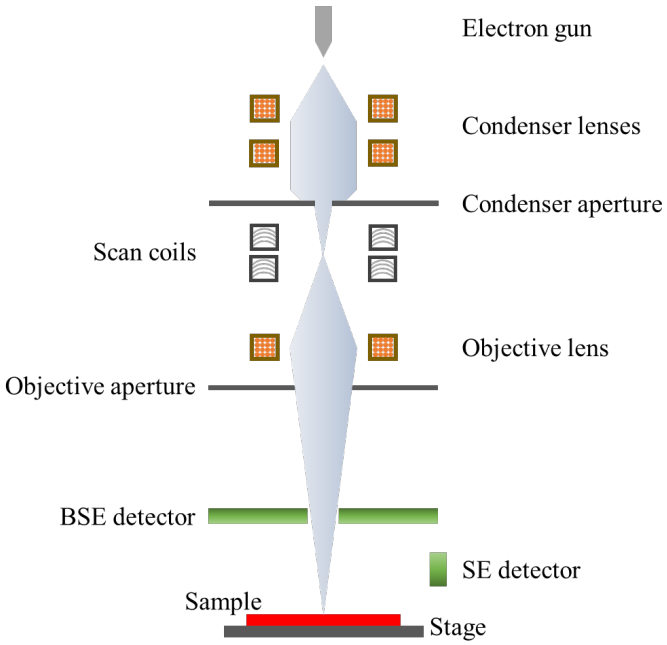

Fig. 2.3.1: Schematic representation of the positioning of electromagnetic lenses in a typical SEM. The position of aperture, detectors and scan coils are also included. Inspired from [18].

The acceleration voltage and beam current are adjustable and affect the formed image. A typical SEM operates at acceleration voltages in the range 2 kV to 30 kV. Increasing the acceleration voltage increases the kinetic energy of the electrons in the beam, enabling them to penetrate further into the sample, giving information from sub-surface features. Lower acceleration voltages give more surface-sensitive images. Increasing the beam current gives a higher signal-to-noise ratio as more electrons are incident on the sample, but it also increases the probe diameter which lowers the resolution. Thus a lower beam current is preferential as long as the noise signal is not significantly reducing the quality of the image.

When the beam electrons interact with the sample, electrons and X-rays can be detected around the sample. There are two types of electron signals in a SEM instrument; backscattered electrons (BSE) and secondary electrons (SE). SEs are generated as incident electrons inelastically collide with the specimen electrons, giving them enough energy to be knocked out of their orbit and into the detector. The SEs originate from the first few tens of nm of the sample surface and give topographical information. Multiple SEs can be generated from a single incident electron. BSEs are the electrons from the incoming beam undergoing scattering events below the sample surface before being projected out. This allows BSEs to come from further into the sample, providing sub-surface information. Furthermore, the probability of scattering events for BSEs is dependent on the elemental composition of the sample. Heavier elements have a larger probability of scattering electrons than lighter elements, which is observable as a brighter contrast in the generated image. This concept is similar to dark-field (DF) scanning transmission electron microscopy (STEM) imaging, which is covered in subsection 2.4.3. Beam electrons may also knock out the inner shell electrons from the specimen, which are replaced with outer shell electrons. During this exchange, energy is emitted as photons. The wavelengths of the emitted photons are in the X-ray range and characteristic for each element. A semiconductor detector

in the sample chamber absorbs these X-rays and generates a spectrum of the elements present. This characterization technique is called energy-dispersive X-ray spectroscopy (EDS) and will be described in further detail in section 2.5.

2.4 Transmission Electron Microscopy

A transmission electron microscope is a powerful instrument used in material science and physics to examine the nanoscopic properties of materials. Alike SEM, a TEM utilizes electrons to form an image. Electrons, having much shorter wavelengths than visible light, can in theory resolve features down to the Angstrom scale. With the high acceleration voltage and thin samples of TEM, such a high resolution becomes achievable. Detailed insight into the micro and nano-sized regimes becomes reachable, where some of the most outermost important degradation mechanisms are located. TEM can also be combined with spectroscopy techniques, allowing further insight into the chemical composition of the anode. The main downside with TEM is first and foremost the high costs of the instrument and the accompanying equipment. Additionally, preparing samples and handling the instrument are technically challenging.

The theory of TEM is far too extensive to be covered in this thesis. The sections below are an attempt to cover the most central aspects relevant to the work carried out. It is based on the four-volume series by Williams and Carter [138], which the reader is referred to for additional details and uncovered topics. Citations to their work are thus omitted. Additionally, this section was also covered in the author's project thesis, and will therefore overlap with some of its content [139].

2.4.1 Design and Operation

The first transmission electron microscope was made by Max Knoll and Ernst Ruska at the Berlin Technische Hochschule in 1931. This was before the first SEM, but the two microscopy techniques share several similarities. Contrary to SEM, the electrons are transmitted through the sample and projected onto a fluorescent screen or a charge-coupled device (CCD) camera by several lens systems. Another difference between SEM and TEM is the acceleration voltage. Most TEM instruments operate with acceleration voltages of 60 kV to 300 kV, but some instruments can operate at a few kV and others in the MV range. The high voltage provides the electrons with much higher kinetic energy, enabling higher achievable resolution when combined with extremely thin samples. Note that this is and will be a simplification of the real working principles, and that in reality, a TEM is more complex.

The Electron Gun

The electron source is called an electron gun, and there are two types of electron guns. These are thermionic guns and field emission guns (FEG). Thermionic guns work by heating a filament,

such that electrons in the material overcome the work potential function, allowing them to loosen from the filament and radiate in all directions. Thermionic filaments must have very high melting points, and therefore a bent tungsten wire with a melting point at $T_m = 3660$ K was commonly used as a filament in early TEMs. Modern TEMs commonly use a LaB_6 filament, as it has almost half the work potential compared to tungsten, yielding higher electron currents at the same temperature. LaB_6 also have longer lifetimes, but are much more reactive and thus require UHV and pristine conditions.

FEGs use an electric field to draw out electrons, by applying a strong negative potential to a needle-shaped tungsten filament. The small tip radius concentrates the electric field to a smaller point and reduces the area from which electrons can be emitted from. The filament must be pristine, which makes it very difficult to replace an old filament with a new one. Heating of the filament makes it easier to keep it pristine, as well as aiding electron emission. Heat-assisted FEGs are commonly called Schottky emitters, while non-heat-assisted FEGs are called cold-FEGs. The latter requires a higher vacuum, is more expensive and less common.

FEGs are often preferred over thermionic sources for high-resolution imaging, as they can offer superior brightness and coherency. Coherency is divided into spatial and temporal coherency, referring to their spatial spread from the filament and their spread in kinetic energy, respectively. FEGs emit their electrons from a smaller point on the filament using an electric field, and thus yield a better spatial and temporal coherency than thermionic sources. That said, for imaging with lower magnification, thermionic sources provide a better and more stable beam.

Lenses

The lenses in a TEM serve the same purpose as in traditional optical microscopes, in that they bend radiation to form and magnify an image. The principle difference is that since electrons are used for illumination, the lenses are electrostatic or electromagnetic and generate a field which manipulates the beam from the electron gun.

Figure 2.4.1 shows a schematic of the lens systems in a typical TEM. Note that this figure is greatly simplified, as it for instance does not show any detectors or lens details. The condenser lens collects the electrons from the electron gun, and forms a stable narrow beam which is sent towards the sample. The objective lens is split up in the upper and lower polepieces which are located over and under the specimen stage, respectively. This lens system is the most important, as it forms the image and the diffraction pattern, which are magnified by the intermediate and projection lenses.

The lens systems in a TEM are built up by deflectors, stigmators, an aperture and the lens itself. Since the illumination source is an electron beam, the lenses are electrostatic or electromagnetic. The latter consists of a polepiece and Cu coils. As current passes through the coils, a magnetic field is generated, which manipulates the electron beam. Before the electron beam passes through the lens, a set of deflectors correct the beam path, centering its position of incidence into the lens. After the lens, a set of stigmators correct the distorted beam from an elliptical shape, into

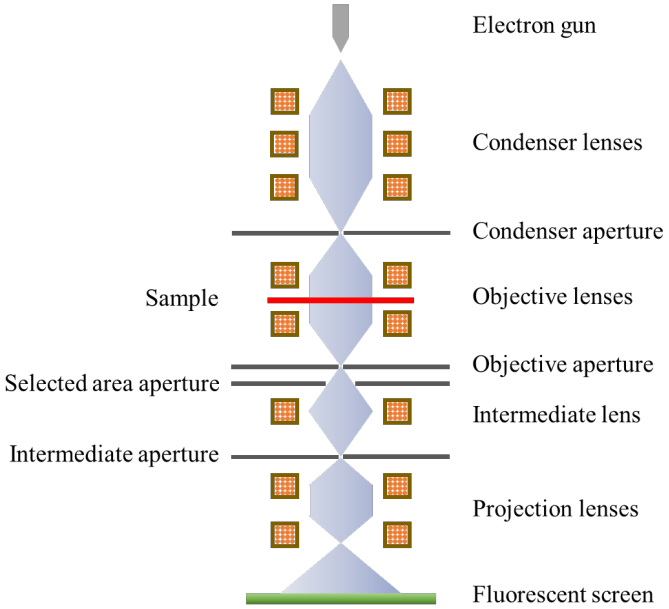

Fig. 2.4.1: Schematic representation of the positioning of electromagnetic lenses in a typical TEM. The figure does not include detectors, correctors and STEM-components. In normal operation, the electron path depends on the activated lenses. Inspired from [18].

a circle. At the end of the lens system, there is an aperture which blocks out parts of the beam. By inserting an objective aperture in the back focal plane, it is possible to filter out electrons scattered to certain angles, which increases the contrast of the image.

Analogous to imperfect lens curvature in optical microscopes, aberrations hindering the formation of an ideally distributed magnetic field in the lenses cause the electrons to not focus onto a single spot. These are called spherical aberrations, and make the image appear as blurry. Spherical aberrations can be corrected with C_S correctors. TEMs with C_S below the sample are called image-corrected. TEMs with C_S correctors above the sample are called probe-corrected. Instruments with both are called double-corrected. Chromatic aberration is another aberration type, in which the electrons enter the lens with a relatively wide spread in temporal coherency, and thus do not experience the same force from the magnetic field in the lens. The electrons are thus deflected with slightly different angles, reducing the obtained resolution. Chromatic aberrations are corrected with C_c correctors, not to be confused with monochromators which are in essence energy filters.

2.4.2 Modes of Operation

What makes TEM so powerful is that it can operate in both normal imaging mode and diffraction mode. In both modes, the beam illuminates the specimen in the same way. With the use of intermediate and projection lenses, either the back focal plane or the image plane are magnified to form diffraction patterns or images, respectively.

Diffraction mode is very powerful when working with crystalline materials, and thus heavily used in the field of crystallography. Due to the wave properties of electrons, diffraction patterns

are formed after interacting with the crystal lattice, according to Bragg's law and the Laue condition. With a TEM, electrons from a selected area of the sample can be chosen to contribute to the diffraction pattern. This is called selected area electron diffraction. As only amorphous thin films were investigated in this work, the reader is referred to the aforementioned series by Williams and Carter [138] for further reading on this topic.

2.4.3 STEM

Many modern TEMs can also operate in scanning TEM (STEM) mode which, as the name suggests, is a hybrid between SEM and TEM. Own dedicated STEM instruments also exist. The images resemble those from a TEM in imaging mode but differ in that they are formed by scanning a convergent beam across the sample. An image is formed by scanning the electron beam across the sample using deflection scan coils and measuring the intensity of the transmitted and forward scattered electrons. The time it takes to measure one pixel is called the dwell time. Increasing the dwell time increases the signal-to-noise ratio, but also the time to capture one frame. Figure 2.4.2 shows a schematic of the active components of TEM which is operating in STEM mode. Some of the transmitted electrons are scattered at high angles and collected by a high-angle annular dark-field (HAADF) detector. Electrons scattered at lower angles are collected by an annular DF detector. Electrons scattered to small angles, or not scattered at all, are collected by a bright-field (BF) detector. The probability of scattering events generally increases with Z, which is the atomic number. For this reason, heavier elements are seen as darker in BF images and brighter in DF images.

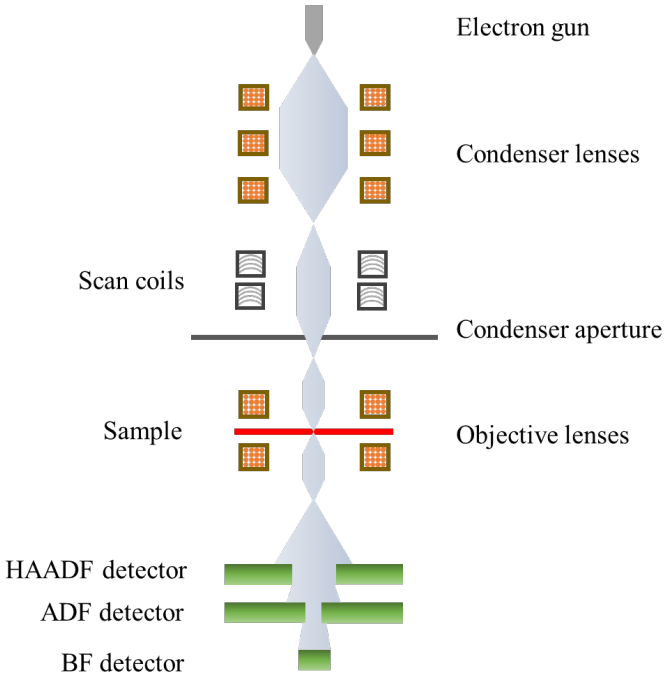

Fig. 2.4.2: Schematic representation of a TEM operating in STEM mode, showing only the active lenses and the scan coils. HAADF, annular dark-field (ADF) and BF detectors are positioned below the sample. Figure inspired from [18].

Another key difference between a TEM in STEM mode, and a conventional SEM, is the acceleration voltage. Electrons in a STEM have much higher kinetic energy, such that they can be transmitted through the sample more easily, as well as being focused to a smaller spot. In combination with the thin TEM samples, the interaction volume becomes very small compared to SEM. The interaction volumes are illustrated in Figure 2.4.3. The achievable spatial resolution in STEM is primarily limited by how small the electron probe can be made, i.e. the smallest possible area on which the probe converges onto. Factors which limit how much the probe can be focused are spherical and chromatic aberrations, and the electron filament. Assuming the probe is as good as it can be, the achievable resolution further depends on the sample thickness and type. For crystalline materials oriented along their high symmetry axis, the atomic planes act as mirrors and trap the converged beam, maintaining the spatial resolution. For amorphous samples, the beam converges outwards through the thickness of the sample. The electrons may also laterally diffuse within the sample. For this reason, amorphous materials can not be imaged with the same resolution as crystalline.

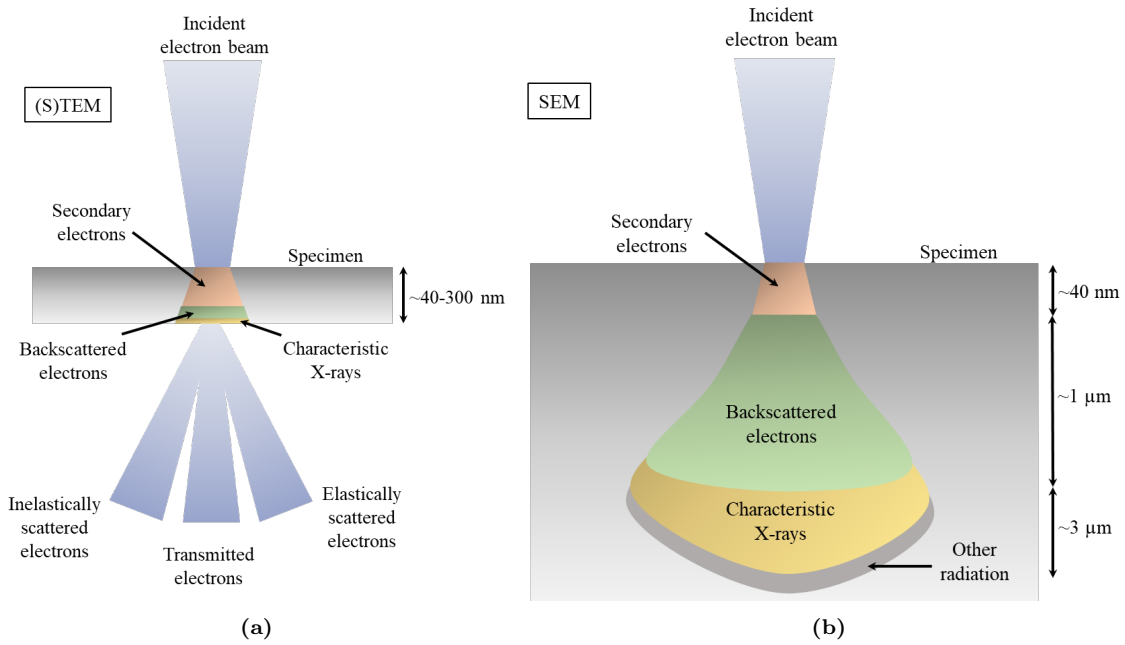

Fig. 2.4.3: Interaction volumes of (S)TEM (a) and SEM (b). The figure shows from where in the samples the signals origin. Distances vary depending on beam parameters and the composition of the examined samples. Distances in the figures are not to scale.

2.5 Spectroscopy

This section is also based on the four-volume series by Williams and Carter [138], which the reader is referred to for additional details and uncovered topics, and from which citations are omitted. This section was also covered in the author's project thesis, and thus includes some of its content [139]. EDS and electron energy loss spectroscopy (EELS) are the two spectroscopy methods most commonly used in a TEM. They are complementary to each other, and provide information on which elements are found in a given sample, as well as where in the sample.

2.5.1 Energy-Dispersive X-ray Spectroscopy

Electrons in the electron beam can interact with the atoms in the sample in several ways, e.g. by inelastic scattering. An incident electron may knock out an atom's electron, causing another electron from a higher energy-level to fall to a lower energy level to fill the vacancy. During the transition, energy is emitted as photons in the X-ray range. These photons are characteristic for each element, and therefore provide information about which elements are present in the sample. A useful feature of EDS is elemental mapping, in which the spatial distribution of the elements in the sample is visualized. In a TEM, the instrument must be operated in STEM mode to form elemental maps as they are constructed by narrowing the beam into a probe and scanning one pixel at a time. Elemental mapping is also common feature in most SEM instruments with an EDS detector.

Another feature of EDS is quantitative determination of the composition, i.e. the amount of the elements present. However, it comes with a certain amount of uncertainty. There are several common methods to convert measured intensity to concentration. One of which is the Cliff-Lorimer method, based on the Cliff-Lorimer equation

$$\frac{I_A}{I_B} = \frac{C_A}{C_B} k_{AB} \tag{2.5.1}$$

which calculates the concentration of the observed elements by using the characteristic peak intensities for elements A and B, I_A and I_B, respectively. C_A and C_B are their respective concentrations, and k_{AB} is the Cliff-Lorimer k-factor, which is a proportionality constant. Much uncertainty is related to this factor, as to how it varies with element, beam energy, and other parameters [140]. At best, the uncertainty k_{AB} is $< \pm 5 - 10\%$ [138]

A challenge concerning EDS is artifacts in the spectrum, which may mislead an unaware eye, and cause misinterpretation around obtained results. EDS artifacts are categorized into two main groups: Signal detection artifacts, such as stray X-ray and escape peaks, and signal processing artifacts, such as sum peaks and peak overlapping. Not all artifacts are always present, but a brief understanding is recommended for a more correct interpretation of EDS-spectra.

Stray X-rays: Stray X-rays are spurious signals generated outside the region of interest (ROI). Commonly stray X-rays are generated from BSE and SE which hit the polepiece, stage, sample grid, other areas on the sample or even other areas in the chamber. These collisions can generate unwanted X-rays which are measured and thus seen in the spectrum. A collimator positioned at the tip of an EDS detector helps block out stray X-rays. In the case of TEM, the sample grid is often made of Cu, and the inside of the TEM is made of Fe. Therefore Cu and Fe signals often show when their absent from the sample.

Escape peaks: Escape peaks are signal detection artifacts that occur when not all the emitted characteristic X-ray energy is absorbed by the X-ray detector, generating electron-hole pairs which contribute to the measured signal intensity. This can happen when a photon fluoresces the Si, generating a Si K_α line with energy $E = 1.74$ keV. A small fraction of the intensity of

the characteristic peak is thus moved to the escape peak at 1.74 keV further down the spectrum. Simultaneously, an increase can be detected at the Si K_α line. This effect is called Si internal fluorescence peak, and occurs if "dead" areas in the Si crystal produce their own X-rays, which are detected by the "live" areas. Some detectors are more exposed than others, however, escape peaks are rarely greater than 2 % of their characteristic peaks, making the effect insignificant in most situations. Other fluorescent effects are also possible, where generated x-rays lines from one material match another line with another material, exciting their atoms instead. Fluorescence effects further increase the uncertainty of the elemental concentrations.

Sum peaks occur when two X-rays arrive at the detector simultaneously. When this happens, the pulse processor is not able to distinguish them and instead measures the sum of these, forming a new peak. The result is the appearance of a new element, or strengthening of the element if it is already present. The probability of sum peaks occurring is related to the electronics' ability to avoid pulse pile-up, which is increased with increasing count rate and dead time. After a photon arrives at the detector, the detector shuts for a period of less than a µs, called the dead time, during which incoming pulses are not measured. Longer dead times cause incoming pulses to be rejected, while shorter dead times result in a longer time to get a spectrum. The optimal dead time for mapping is 40-60 %.

There are several advantages of using EDS in (S)TEM, over SEM. TEM instruments operate at much higher acceleration voltages and examine thinner samples, resulting in a smaller interaction volume. SEM interaction volumes from which X-rays are generated, are considerably larger and lead to higher X-ray absorption within the material. Figure 2.4.3 shows the interaction volume of SEM and (S)TEM. Finally, SEM samples must be electrically conducting, such that none-conducting samples must be coated with a conducting material prior to characterization. The coating will show up in the spectrum, but often this is not a major issue, as it is very thin.

A great downside of EDS, in the relevance of LIBs, is its inability in effectively and accurately detecting light elements, e.g. Li which has a very low fluorescence yield and thus produces an extremely weak signal [140]. The low fluorescence yield is because Li often is a cation in the +1 oxidation state, such that no remaining electrons are available to replace the vacancy in the K-shell after excitation. Additionally, most EDS detectors have a protection window between the sample and the detection system. This window absorbs low-energy X-rays, e.g. those which would originate from Li.

2.5.2 Electron Energy Loss Spectroscopy

EELS differs fundamentally from EDS in that the electrons transmitted through the sample are detected and are used to generate the spectrum. As the electrons are transmitted, they interact with the sample through inelastic collisions, losing a fraction of their kinetic energy. During the collision, inner shell electrons in the sample are excited to a state above the Fermi level. The transmitted electron beam is dispersed using a magnetic prism such that the electrons are separated based on their kinetic energy. Thereafter they are recorded to form an energy-

loss spectrum, as the lost energy corresponds to the ionization energy of the atom the incident electrons collided with.

The EELS spectrum is divided into two regions; low-loss and high-loss. The low-loss spectrum includes the energy-loss range <50 eV, containing the zero-loss peak for unscattered and elastically scattered electrons which have not experienced a loss of kinetic energy. The low-loss spectrum holds information about physical properties, e.g. band structure and dielectric properties. The high-loss spectrum, also called the core-loss, includes the energy range >50 eV and is where the majority of the aforementioned ionization edges are located. As there are significantly fewer inelastically scattered electrons than elastically scattered and unscattered, this spectrum has a much lower intensity than the low-loss spectrum [141, 142].

Measuring the loss of electron energy is heavily reliant on a monochromatic electron beam, i.e. the energy spread of the electrons should be as small as possible, e.g. with a cold-FEG. Schottky emitters can be combined with a monochromator to achieve similar energy resolutions.

EELS has several advantages over EDS. First of all, since EELS is not dependent on generated X-ray signals, it can detect Li signals and other light elements which are challenging to obtain good signals from in EDS. That said, it requires the samples to be very thin. The Li K edge is at 54.8 eV, which can easily be drowned by bulk plasmon edges if the TEM sample is not thin enough. Bulk plasmons are collective oscillations of the loosely bound electrons in the material. Loosely bound electrons in the conduction and valence bands can produce an oscillating polarization as they move around a quasi-stationer set of nuclei. This collective set of oscillations may be described as a quasi-particle, plasmon, which may inelastically collide with incident electrons, which is visible in the EELS spectrum. They typically appear near the zero-loss peak and up to $\sim$ 30 eV but may appear at higher energies, if the thickness of the sample allows for multiple inelastic scattering events. This distorts the pre-edge background, essentially masking the Li K-edge.

On the bright side, EELS uses electron energy loss to generate spectra, thus it does not suffer from the artifacts of EDS as described in subsection 2.5.1. Similarly to EDS, the spectra from different pixels are put together to form a map. The concentration of the elements can be found with EELS as well, but quantitative analysis is much more challenging with EELS than EDS. Part of the reason being substantially more data processing, in which background subtraction, deconvolution to remove plural scattering effects and edge integration must be performed [142]. However, since EDS relies on generated X-rays, while EELS on forward-scattered electrons, they can be used simultaneously and serve as complementary to each other. Additional drawbacks of EELS include sample and instrument requirements. The samples should ideally be very thin, i.e. 10 nm-100 nm.

CHAPTER 3

METHODS

This chapter describes all methods and techniques used. A description of the fabrication of the thin films before they were received by the author is also provided. A table of all the produced and characterized samples is presented later in the results, in Table 4.1.1. A total of six samples were characterized, from two different films and three stages of cycling. From each of the two films, one uncycled film, one film after three formation-cycles in galvanostatic testing, and one film after 1000 cycles. This combination was chosen in order to compare the cycling performance and degradation of a SiC_x film versus a pure Si film.

3.1 Sample Preparation

3.1.1 Plasma-Enhanced Chemical Vapor Deposition

The thin films investigated in this work were deposited with an Oxford PlasmaLab 133 situated in a cleanroom environment. This was done by supervisor Marte O. Skare at the Institute For Energy technology (IFE) at Kjeller, Norway. The low concentration of air-born dust particles allows for minimal contamination onto the sample ahead of and after film deposition. The instrument is a direct deposition plasma-enhanced chemical vapor deposition (PECVD) with a parallel-plate design driven by a 13.56MHz RF power supply to ignite the capacitively coupled plasma. Two films were deposited, one with pure silicon and one with substoichiometric silicon carbide (SiC_x). For the pure silicon film, 40 standard cubic centimeter (sccm) silane (SiH_4) was used as the only precursor. For the SiC_x film, a combination of 20 sccm silane and 80 sccm methane (CH_4) was used. Deposition parameters of the two films are given in table Table 3.1.1. All films were deposited on non-dendritic Cu foils cleaned with acetone and ethanol. The Cu foils were mounted onto 4 inch $\times$ 4 inch Si wafers.

From each of these films, seven 15 mm discs were punched out. Four discs were used to make

Table 3.1.1: Deposition parameters for the thin films examined in this work. High CH_4 precursor prevented plasma ignition at 40W for SiC_x samples. Therefore plasma power of 60W was used to ignite the plasma, before being reduced to 40W for the rest of the deposition.

Material	**SiC_x**	**Pure Si**
Precursors [SiH_4/CH_4/sccm]	20/80	40/0
Deposition time [s]	506	275
Plasma power [W]	60-40	40
Chamber pressure [mTorr]	300	300
Substrate	Cu	Cu
Substrate temperature [°C]	400	400

coin cells for cycling, while the three remaining were sent to TEM sample preparation.

3.1.2 Cell Fabrication and Opening

The cycled 2032 (20 mm diameter and 3.2 mm thickness) coin cells were fabricated in an Ar-filled glove box with <0.1 ppm H_2O and <0.1 ppm O_2 with the following procedure:

1. Stainless steel bottom cap from Hohsen Corp
2. Electrode with Cu-foil (current collector) facing down, centered in bottom
3. 15 µl electrolyte
4. 18 mm Celgard separator
5. 15 µl electrolyte
6. Gasket
7. Li metal disk scraped free of oxides using scalpel
8. Stainless steel spacer and washer
9. Stainless steel top cap from Hohsen Corp
10. Sealing in crimping machine

A schematic of this is also shown in Figure 3.1.1. The liquid electrolyte was provided by Solvionic, and consists of 1.2 mol/L in (3:7 vol%) EC/EMC + 2 wt% vinylene carbonate + 10 wt% fluoroethylene carbonate (FEC)-99.9 %.

After cycling, the cells were opened in a similar glove box to the one they were made in. For each of the four cells, the cap was opened with a coin cell disassembly tool to extract the content. The active material was rinsed in a bath of DMC, and the other components were discarded. The electrode was transported from the glove box to the FIB, via a sealed plastic bag. Ideally, an inert transfer chamber would have been used, but this was not available at the time in which the experimental work was carried out.

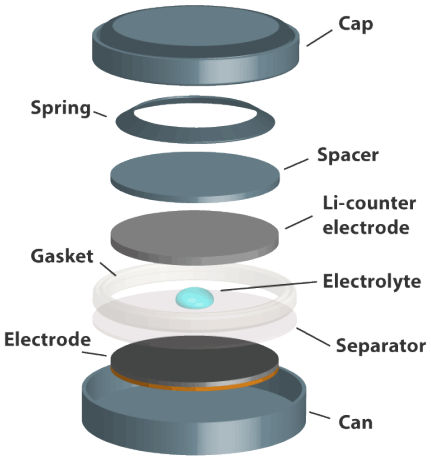

Fig. 3.1.1: Schematic of the components of a coin cell. Figure provided by Jan Petter Mæhlen at IFE.

3.1.3 TEM Sample Preparation with FIB

All TEM samples examined in this work were prepared with a FEI Helios NanoLab DualBeam FIB in a cleanroom environment. The FIB column is angled 52° relative to the SEM column, which is parallel to the sample stage's rotational axis. The tilting axis of the stage is perpendicular to both columns. The instrument also has a gas injection system (GIS) enabling the deposition of carbon, platinum and other elements from precursor gasses. The instrument is equipped with an Everhart Thornley detector, a through-lens detector (TLD), and an ion conversion and electron (ICE) detector. Overview images of the samples were captured with the TLD detector in immersion mode. In this mode, an electro-magnetic lens is activated, which provides better spatial resolution, but also exposes the sample to a magnetic field. During sample preparation, the ICE detector was used, as it shows a brighter contrast when the sample becomes thinner than $\sim$ 100 nm. The brighter contrast comes from the positioning of the detector, such that more electrons are detected as the lamella becomes thinner. Thin films from the cycled batteries were mounted onto the specimen stage right before chamber evacuation, to reduce exposure to normal atmosphere. The procedure for preparing TEM-lamellae with a FIB is given below, and also shown in Figure 3.1.2:

1. Use the electron beam and carbon precursor gas to deposit a $\sim$ 100 nm protection layer over an area of 10 µm × 2 µm. Electron beam voltage 3 kV and current 11 nA.

2. Tilt the stage 52°, such that the FIB column is incident normal to the surface of the thin film. Deposit a $\sim$2 µm thick carbon protection layer on top of the previously deposited layer. Ion beam voltage 30 kV and current 93 pA. See Figure 3.1.2 a).

3. Mill out sections around the protection layer, forming the TEM-lamella. See Figure 3.1.2 b).

4. Tilt sample back to 0°. Perform a cut below the lamella, such that it is only held by a tiny bridge connecting it to the rest of the surface.

5. Insert nanomanipulator needle and position it such that it barely touches the side of the lamella.
6. Attach the needle to the lamella, and deposit Pt to connect them. See Figure 3.1.2 c).
7. Mill the remaining connection between the lamella and the rest of the sample.
8. Move the needle with the lamella over to one of the fingers of the TEM grid, attach it using Pt, and mill away the Pt connecting the lamella to the needle.
9. Begin with voltage 30 kV and current 0.92 nA and thin the lamella down to 300 nm. Gradually reduce the ion beam current, and thin down until the sample thickness is below 60 nm. See Figure 3.1.2 d).

A carbon protection layer was used ahead of milling with the FIB. Often Pt is used for the protection layer, but as Pt gives a very bright contrast in HAADF STEM images, carbon was chosen. The amorphous pure carbon layer is much lighter than the thin film, and therefore distinguishable because of its brighter contrast in BF TEM and darker in HAADF STEM.

TEM sample preparation of thin films can also be done manually by polishing with diamond lapping films, dimpling and precision ion polishing. These strategies are more suitable for harder samples, such as sample preparation from a bulk of Al, or thin films deposited on Si wafers. FIB sample preparation has the downsides of structural changes under electron and ion beam exposure, as well as Ga-ion implantation, but allows for more accurate preparation of sub 100 nm regions.

3.2 Electrochemical Characterization

Electrochemical testing of the CR2032 half-cells with Li metal as the counter electrode was conducted at IFE's laboratories using an Arbin BT-20000 galvanostat/potentiostat at ambient temperature between 0.05 V and 1 V vs Li/Li^+. The first cycle of all the cells was a taper cycle, in which the C-rate was adjusted from C/20 to C/100 and then C/200. The second and third cycles were held at C/20 rates, while the rest of the cycles were run at 1C. Cycling was ended in a delithiated state with respect to the working electrode. Additional cycling parameters are provided in Appendix B.

3.3 Electron Microscopy

In advance of TEM characterization, the thin films were imaged with the FIB instrument presented previously. The settings on the instrument were 3.0 kV, 0.17 nA, TLD detector in immersion mode, 0 tilt and x25000 magnification. Secondary electrons were detected rather than backscattered for better insight into the surface morphology.

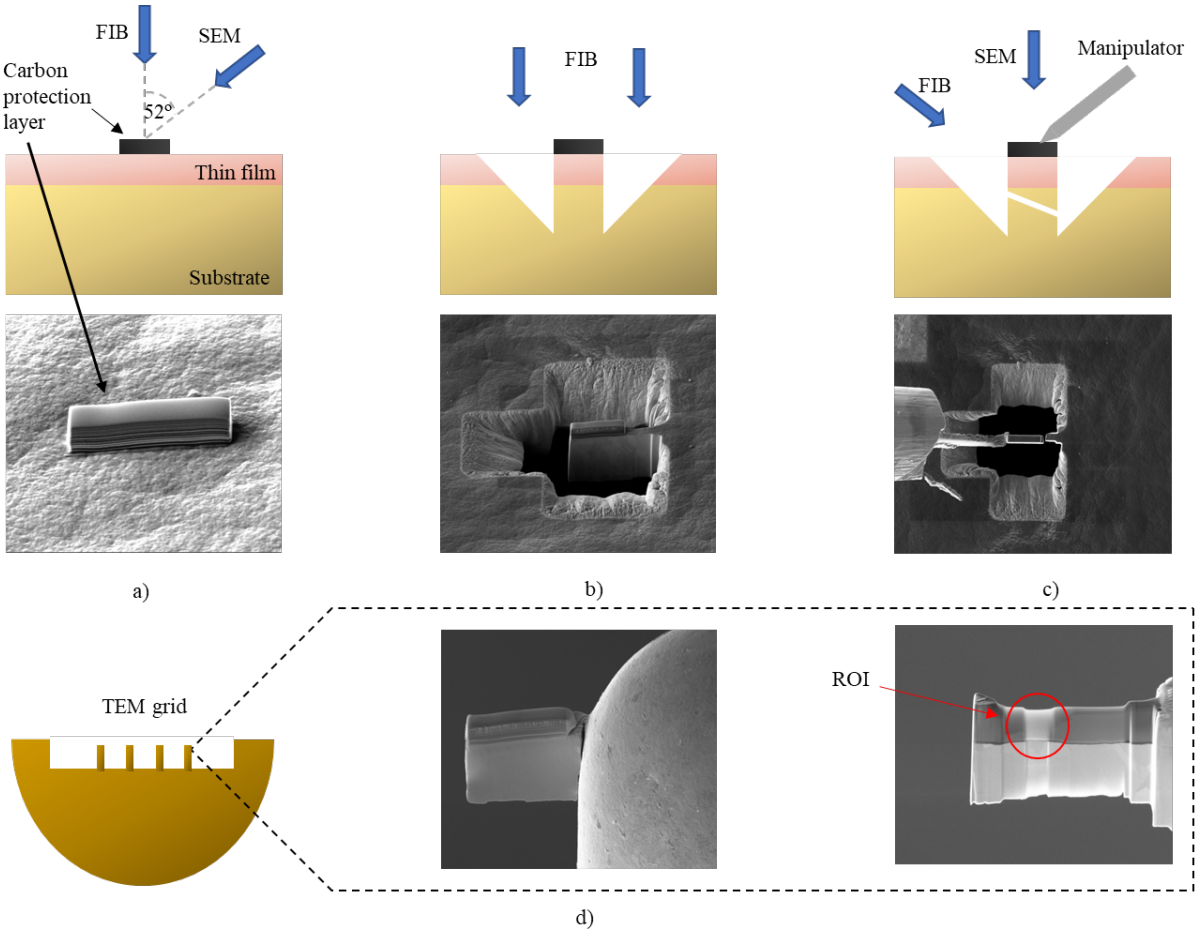

Fig. 3.1.2: Schematics showing the procedure of producing TEM samples from a thin film on a substrate, with FIB. a) The electron beam and ion beam protection layers are deposited. b) The area around the lamella is milled away. c) Nanomanipulator is attached to the lamella, and the remaining connection to the sample is removed. d) The lamella is connected to the TEM grid and thinned to <100 nm.

The main characterization work was performed with a Jeol JEM 2100F - FEG microscope, operated by the author. This instrument is optimized for precession diffraction, orientation mapping and tomography, STEM and high-resolution imaging. It is equipped with a 200 kV Schottky FEG with an energy spread of 0.7 eV. The specimen holder is a double tilt holder with a beryllium clamping plate, +/- 35 degrees alpha tilt limit and +/- 30 degrees beta tilt limit. In terms of detectors, it has a bottom-mounted Gatan 2k UltraScan CCD camera, BF and HAADF STEM detectors, and an Oxford X-Max 80T EDX detector with a super atmospheric thin window. This instrument is equipped with the Aztec software, to control and analyze the EDS scans. All EDS results and BF TEM images presented are acquired with this instrument. The samples were mounted such that the TEM lamella on the TEM grid faced the EDS detector, to avoid stray radiation from the Cu-grid.

A Jeol JEM ARM200F - Double corrected ColdFEG microscope was used for EELS spectroscopy, as EELS was not available on the 2100F microscope. The instrument has an energy spread of < 0.3 eV with an under-saturated filament, and < 0.5 eV at standard conditions. It has a C_s-probe corrector and a C_s-image corrector, enabling <1 Å resolution in HAADF and high-resolution TEM. The instrument is equipped with a JED-2300T Centurio EDS detector with

an ultra-thin type window, Quantum Gatan imaging system with DualEELS and 2k CCD. A 2k Orius CCS (side-mounted) and 2k UltraScan XP CCD (bottom-mounted). For STEM it has two BF, one annular DF and two HAADF detectors. The sample was inserted with a reinforced double tilt specimen holder with a beryllium clamping plate, +/- 35 degrees alpha tilt limit and +/- 30 degrees beta tilt limit. The microscope is located in a custom designed room with water-cooled walls and field cancellation, aiding its ability to perform atomic-scale studies. This instrument was used only for three out of six samples. Analysis with this instrument was done in cooperation with supervisor Per-Erik Vullum who was operating the instrument, while data analysis was performed by the author. With limited time on the instrument, only the most important samples were prioritized. These were Si-1000, SiC-1000 and SiC-3. All EELS results presented are acquired with this instrument.

During the majority of the period in which the experimental work of this thesis was carried out, the EDS-detector of the JEOL JEM 2100F was out of order. Thus a similar microscope, a JEOL JEM 2100 was used temporarily to investigate qualitative trends. The instrument is equipped with a 200kV LaB_6 filament, a side-mounted large view Gatan 2k Orius CCD, and BF and HAADF detectors for STEM mode. The sample holder is equivalent to that of the 2100F.

CHAPTER 4

RESULTS

4.1 Samples

This chapter serves to present results acquired with SEM and TEM. An overview of all produced samples is given in Table 4.1.1. Electrochemical characterization was conducted by Marte O. Skare at IFE, from which the results are presented for comparison with results from electron microscopy and spectroscopy. The letters in the sample names represent the composition of the films they are prepared from. Note that the samples labeled with SiC are actually substoichiometric SiC_x, i.e. they do not have a 50/50 Si-C ratio, as the name may mislead. The numbers 0,3,1000 indicate how many cycles they have been charged and discharged in galvanostatic cycling.

Table 4.1.1: Overview of the produced TEM samples.

Sample	**#Cycles**	**Comments**
Si-0	0	
Si-3	3	Slightly electron beam sensitive
Si-1000	1000	Strongly electron beam sensitive
SiC-0	0	
SiC-3	3	
SiC-1000	1000	Slightly electron beam sensitive

4.2 Cycling Data

The results from galvanostatic cycling are presented in Table 4.2.1 and Figure 4.2.1. The charge and discharge capacities are presented as a function of cycle number. The red and the blue lines represent the pure Si and the SiC_x films, respectively. Standard deviation is given as a brighter contrast around the graphs, and is based on three test cells after 1000 charge/discharge cycles in parallel. Note that since the tested cells are half-cells with a Li metal counter electrode, charging corresponds to the delithiation of the thin films. Correspondingly, discharging is associated with the lithiation of the thin films.

Table 4.2.1: Key values from cycling data, i.e. initial CE, and total delithiation capacity loss and retention after 1000 cycles. Calculations are based on film thicknesses measured with ellipsometry at IFE, given in Table 4.4.1.

Sample	Pure Si	SiC_x
Initial specific charge capacity	4381 mAh g^{-1}	2293 mAh g^{-1}
Initial specific discharge capacity	5422 mAh g^{-1}	3289 mAh g^{-1}
Initial CE	81 %	70 %
Total capacity retention	41 %	30 %
Total capacity loss	59 %	70 %

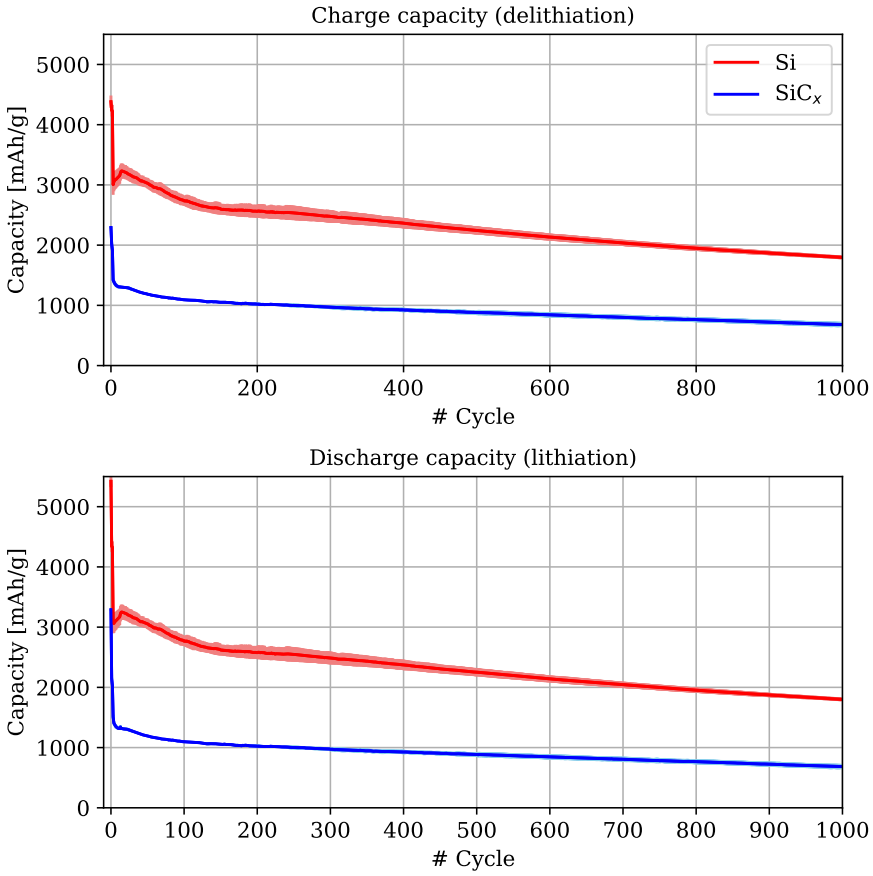

Fig. 4.2.1: Results from galvanostatic cycling of pure silicon film (in red) and Sic_x (in blue). Top graph shows charge capacity, and bottom graph shows discharge capacity, i.e. delithiation and lithiation capacity, respectively. Data provided by Marte O. Skare at IFE

4.3 Surface Morphology

Figure 4.3.1 shows the surface of the 6 films examined in this work. All films were exposed to ambient conditions ahead of characterization. Beginning with the pure Si films, Si-0 in Figure 4.3.1a shows small height variations, but is otherwise relatively flat with small surface features. Small white spots are visible. After three formation-cycles, several cracks have formed on the surface, with an average width of $\sim$ 160 nm and lengths varying from a few hundred nm to several µm. A bright contrast is seen around the crack edges. After 1000 cycles, the surface morphology from the initial film is close to unrecognizable, as seen in Figure 4.3.1c. Cracks are seemingly penetrating through the thin film, and the surface looks swollen. During deposition of the first protection layer as well as imaging, the structure was observed to change when exposed to the electron beam. These regions of the sample were therefore regarded as electron beam sensitive.

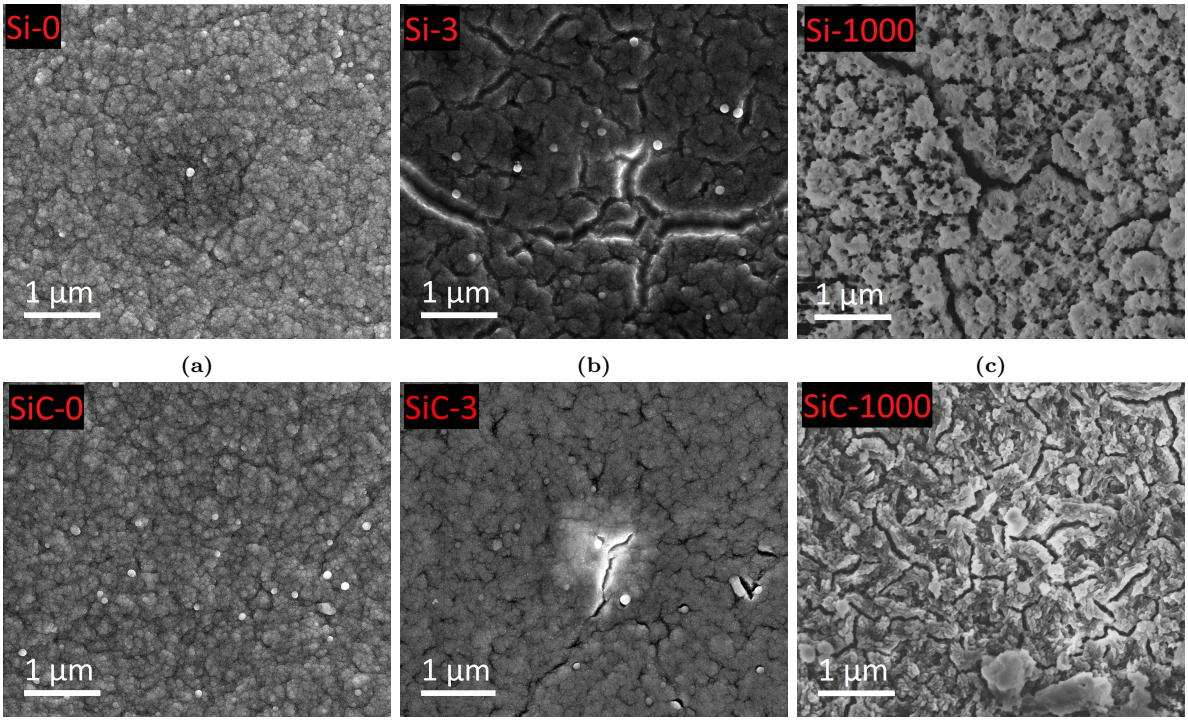

Fig. 4.3.1: Secondary electron SEM overview images of films. All images are acquired with the TLD detector in immersion mode on the dualbeam FIB instrument. a) Si-0 b) Si-3 c) Si-1000 d) SiC-0 e) SiC-3 f) SiC-1000.

Sample SiC-0 also had relatively flat surface morphology, with small height variations and small white spots, as seen in Figure 4.3.1d. Similar to Si-3, cracks had formed after the formation-cycles in SiC-3, but with a lower crack density than Si-3. The average crack size was measured to $\sim$ 50 nm, where most had a length of a few µm. Samples Si-3 and SiC-3 had big variations in crack length, and the presented values indicate observed trends. A bright contrast was observed around the crack edges here as well. Sample SiC-1000 in Figure 4.3.1f has also undergone significant morphological changes, but resembles the original film more than Si-1000. SiC-1000 was also electron-beam sensitive, but not as much as Si-1000. SEM characterization is not the main focus of this thesis, therefore additional SEM images are provided in Appendix A.2

4.4 Physical and Structural Changes

Figure 4.4.1 shows BF images of the cross-section of all six films. Figure 4.4.2 shows similar BF images with thickness measurements that complement Table 4.4.1. Little to no change is seen from the uncycled films to the formation-cycled films, except for an increase in thickness. Based on the values in Table 4.4.1, the pure silicon thin film has expanded 13 % during the three formation-cycles, and 1600 % after 1000 cycles, relative to the uncycled film. The SiC_x film expanded by 8 % after the three formation-cycles, and 540 % after 1000 cycles. The interface between the electron beam and ion beam deposited carbon protection layers is seen for samples Si-0, SiC-0, Si-3 and SiC-1000. Above the films, there is a bright contrast from the electron beam protection layer, above which there is a darker contrast from the ion-beam protection layer.

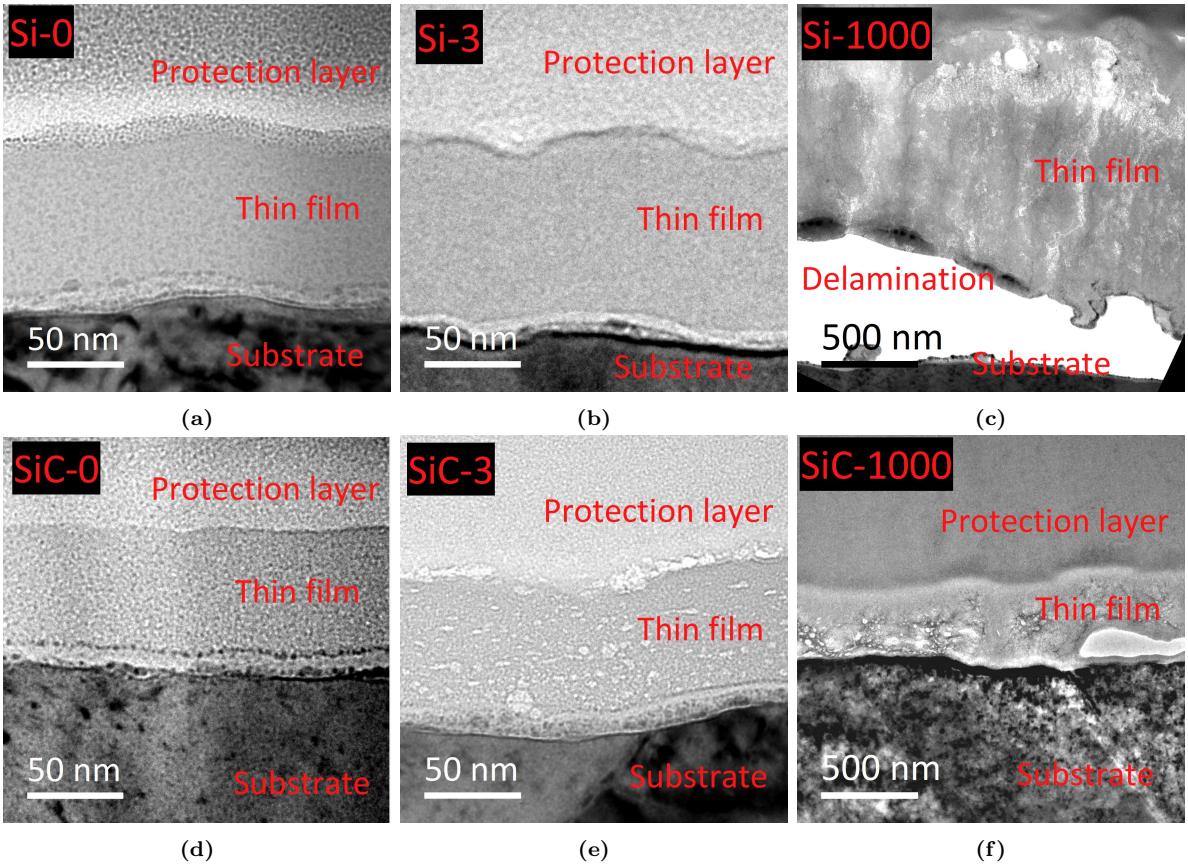

Fig. 4.4.1: Overview images of thin films, acquired with the 2100F TEM instrument. a) Si-0 b) Si-3 c) Si-1000 d) SiC-0 e) SiC-3 f) SiC-1000.

For both the uncycled and the formation-cycled films, an additional phase is observed between the substrate and the film. This layer is labeled "oxide" in Figure 4.4.2, due to the spectroscopy results presented and discussed later. The phase has a slightly brighter contrast and is $\sim$ 10 nm thick in all four films. After three cycles, small holes were observed in SiC-3.

The structure of the SiC_x film is better preserved with fewer changes after 1000 cycles compared to pure Si film which has almost completely delaminated from its substrate. The delamination of Si-1000 is seen in Figure 4.4.1c and also later in Figure 5.2.3a. Additionally, this film is seen

Table 4.4.1: Thickness, t, of all samples. The ellipsometry t is provided by Marte O. Skare at IFE. The TEM thickness is measured with the 2100F TEM instrument. The $\pm$ sign indicated the thickness variations. Uncertainty of thickness measurements is addressed in the discussion. A series of images of the films with low magnification to show thickness variations on the films is given in Appendix A.3

Sample	**Ellipsometry t [nm]**	**TEM t [nm]**	**% t increase**
Si-0	66	80 ± 4	
Si-3		90 ± 15	13%
Si-1000		1395 ± 241	1600%
SiC-0	70	62 ± 3	
SiC-3		67 ± 3	8%
SiC-1000		398 ± 62	540%

to fold at the bottom, observed as increased contrast. Sample SiC-1000 also shows signs of delamination, in the shape of a hole in the film-substrate interface, seen in Figure 4.4.1f and also later in Figure 5.2.3b. In both samples, multiple holes are observed in the thin films. Finally, lack of Bragg diffraction spots by selected area electron diffraction, and lack of diffraction contrast in BF imaging demonstrated that the films were amorphous without any observable crystalline phases.

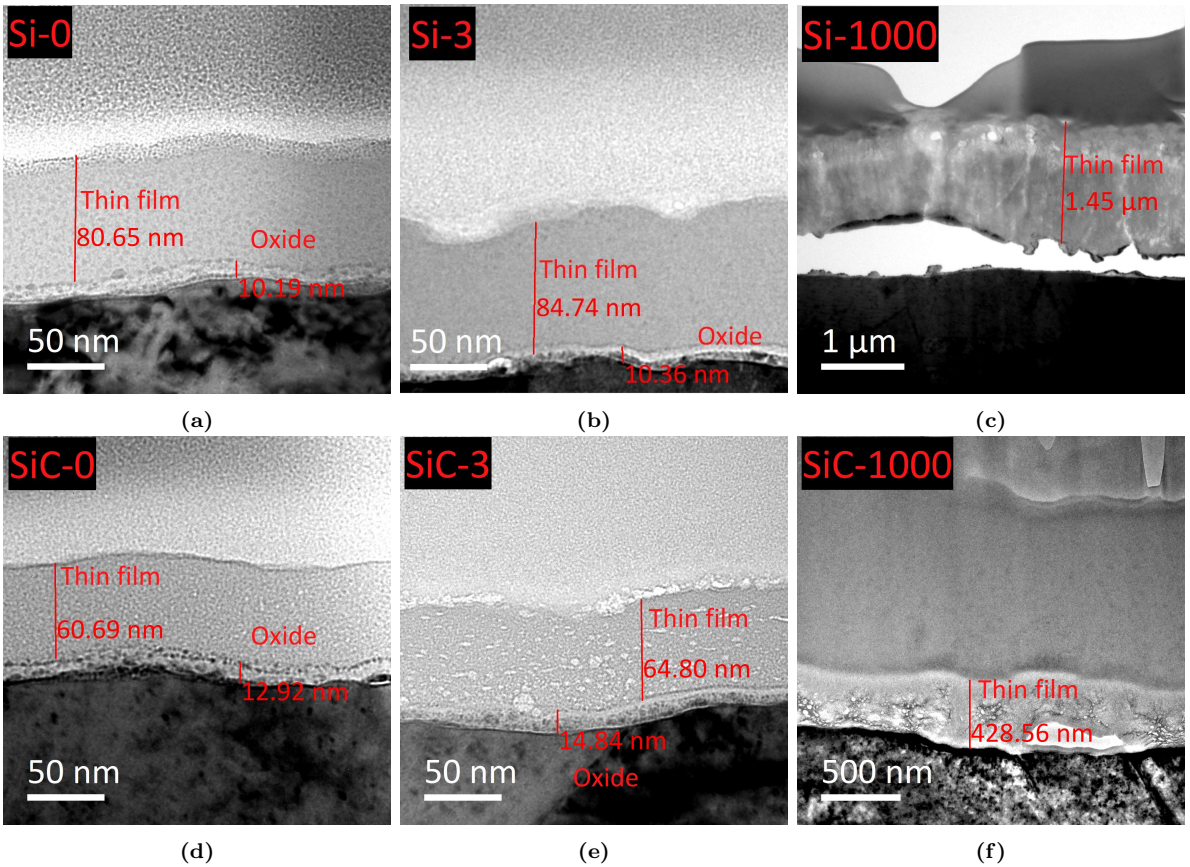

Fig. 4.4.2: Images of films showing thickness measurements of the thin film and the layer between the film and the substrate, labeled "oxide". The labeled lengths differ from those provided in Table 4.4.1, as the tabulated values are averages across the film, and are more reliable. The images are acquired with the 2100F TEM instrument a) Si-0 b) Si-3 c) Si-1000 d) SiC-0 e) SiC-3 f) SiC-1000.

4.5 Chemical Results

Figures 4.5.1 and 4.5.2, are EDS-maps, showing the spatial distribution of elements C, Cu, F, Ga, O, P, Si and Zn. The figures also have a HAADF STEM image with lower magnification which shows the acquisition area for the EDS spectra, marked with a white square and ROI. Note that the intensity scale bars, which indicate the number of counts in the EDS spectra, vary between the different elements and samples. This is because the count-rate during acquisition had large variations, yielding uneven signal strengths between samples. The maps are binned with a binning factor of 2. Between the Cu foil and the bottom of the films, there is a layer containing higher concentrations of O, Zn and P.

Using quantitative EDS, it was found that the x in SiC_x film is ~ 0.53. This value was determined by summing the spectra over a wide region of the film, and finding the ratio between C and Si. The compositions of the thin films are provided in Table 4.5.1.

Table 4.5.1: Atom % of Si, C, O, Cu, Ga, F, P and Zn in samples Si-0, SiC-0, Si-3, SiC-3. Corresponding HAADF STEM images acquired with the 2100F instrument are provided in Appendix A.5. Concentrations were obtained with the Aztec software's "calculate composition" feature.

Sample	Si[at%]	C[at%]	O[at%]	Cu[at%]	Ga[at%]	F[at%]	P[at%]	Zn[at%]
Si-0	80,46	5,2	5,06	8,39	0,82	0,07	0	0
Si-3	85,49	2,3	4,9	6,88	0,38	0,05	0	0
Si-1000	9,18	33,92	45,1	7,04	0,35	3,94	0,48	0
SiC-0	40,78	21,66	18,93	17,66	0,96	0	0	0
SiC-3	61,45	27,19	4,57	6,15	0,63	0,02	0	0
SiC-1000	8,34	57,3	28	4,49	0,56	1,14	0,14	0,02

Figures 4.5.3 and 4.5.4 present EDS linescans across the films Si-0, Si-3, SiC-0 and SiC-3 of the elements F, C, O, Si and Cu. The line profiles are drawn from the Cu-substrate to the C-protection layer, and integrated over a region with little variations in thickness. In the film-substrate interfaces, there is an increase in oxygen concentration. In samples Si-3 and SiC-3, there is an additional smaller oxygen concentration peak at the interface between the top of the film and the protection layer. Fluorine also has a small increase in the same region. In the Si-3 and SiC-3 films, the carbon concentration is seen stable at $\sim$ 30 % throughout the film. The line profiles of the elemental concentrations are smoothed out using a simple algorithm (see Appendix C). The raw data is seen with a brighter contrast behind the graphs. The smoothing has caused the Cu concentration to artificially drop in the beginning of the SiC_x films, which should be overlooked.

Figure 4.5.5 shows elemental maps generated from the electron energy loss ionization edges of Si, O, C and Li separately. EDS maps of F and P are also included. EDS mapping was chosen for F and P because it provided a better signal-to-noise ratio for these elements. Two Si maps were generated from the EELS data: Figure 4.5.5a shows the entire Si signal, independently of the oxidation state of Si. In Figure 4.5.5e, only the energy loss region between 99.25 eV and 102.25 eV is used to make the Si map. This energy loss region has contributions only from zero valent Si and Si in low oxidation states (below +2). The ionization energies required to excite 2p

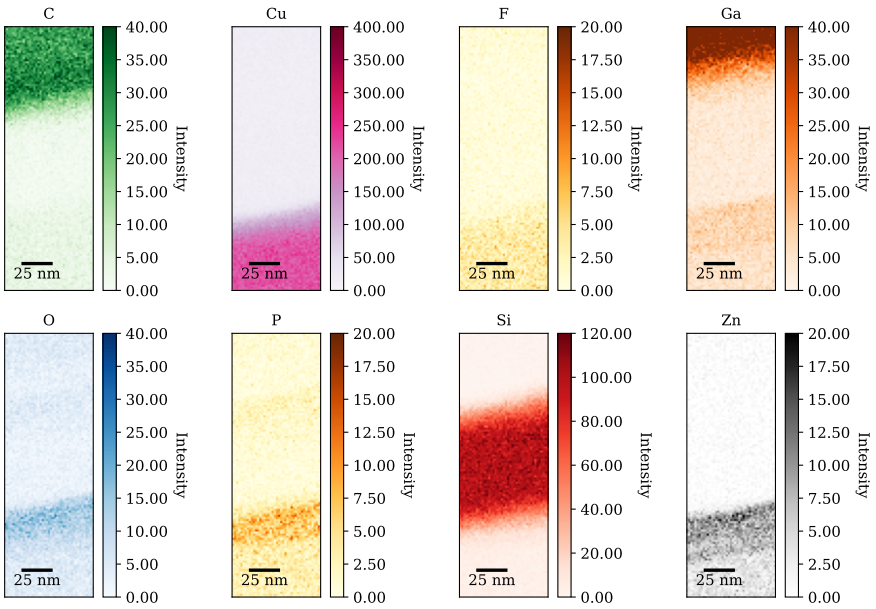

(a)

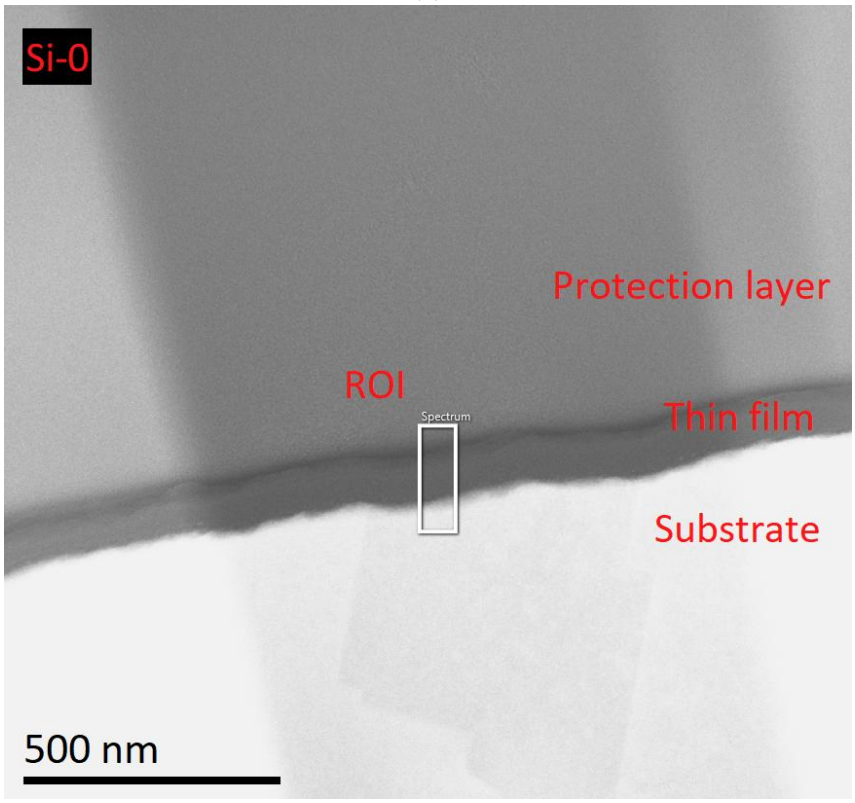

(b)

Fig. 4.5.1: a) EDS colormaps of sample Si-0, showing the distribution of C, Cu, F, Ga, O, P, Si and Zn i the sample, acquired with the 2100F TEM instrument. b) Corresponding HAADF STEM image taken with the 2100F TEM instrument.

electrons to empty states above Fermi level are higher than 102 eV for Si in high oxidation states, i.e. +2 to +4. Hence, highly oxidized Si such as Si in SiO, Si_2O_3 and SiO_2 will not contribute to the signal in Figure 4.5.5e [143, 144]. The latter is labeled Si-filtered. HAADF STEM image acquired during spectroscopy acquisition is also included. Figure 4.5.6 contains corresponding

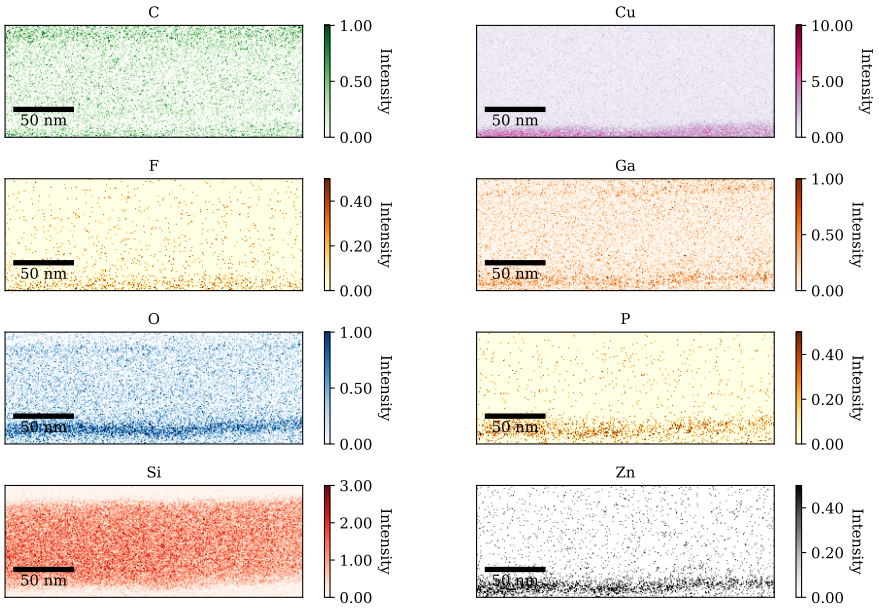

(a)

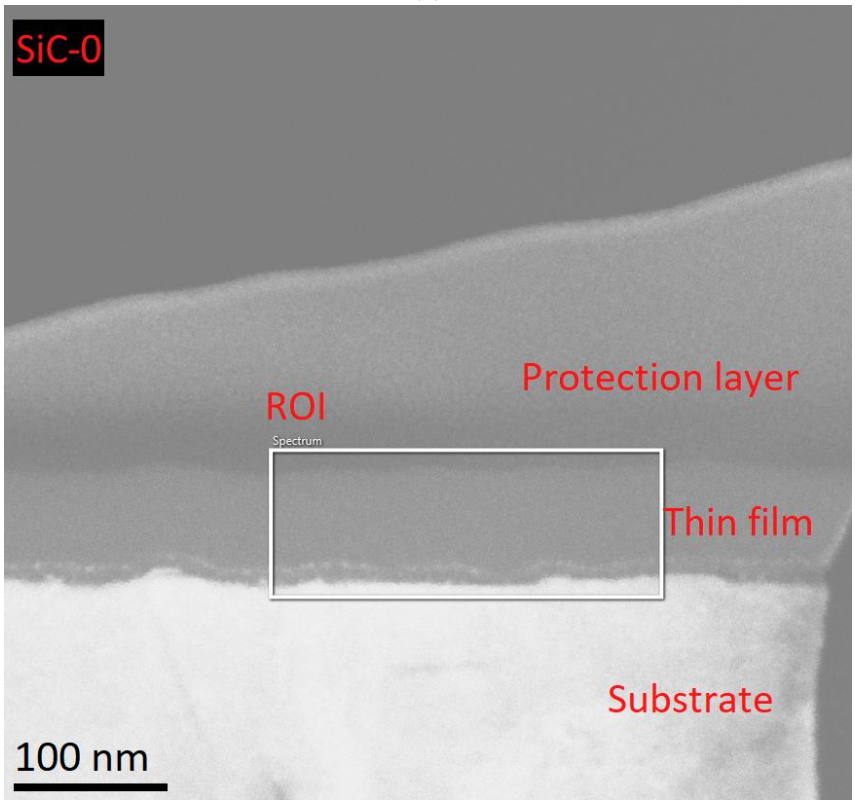

(b)

Fig. 4.5.2: a) EDS colormaps of sample SiC-0, showing the distribution of C, Cu, F, Ga, O, P, Si and Zn i the sample, acquired with the 2100F TEM instrument. b) Corresponding STEM image was taken with the 2100F TEM instrument.

maps for SiC-1000. The energy range for the filtered Si image is 99.4 eV - 102.4 eV.

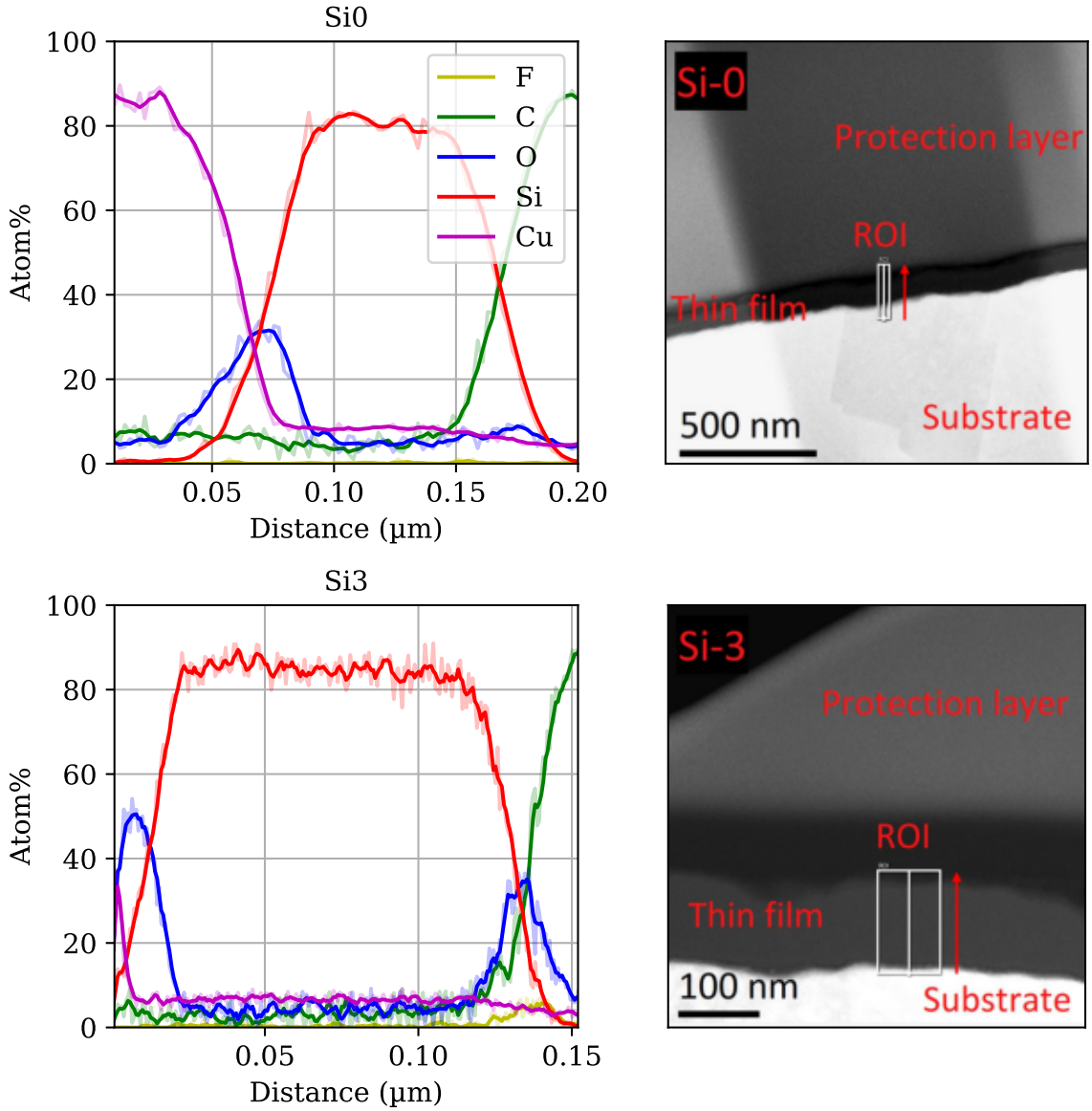

Fig. 4.5.3: Integrated linescan across the film, showing atom % of F, C, O, Si and Cu content (in yellow, green, blue, red and magenta, respectively), of the samples Si-0 and Si-3 with corresponding HAADF STEM images showing the acquisition region. The red arrow indicated the scan direction, i.e. from the Cu foil to the C protection layer. Concentration profiles are smoothed out using a simple algorithm (see Appendix C). The raw data is seen with a brighter contrast behind the graphs. Acquired with the 2100F TEM instrument.

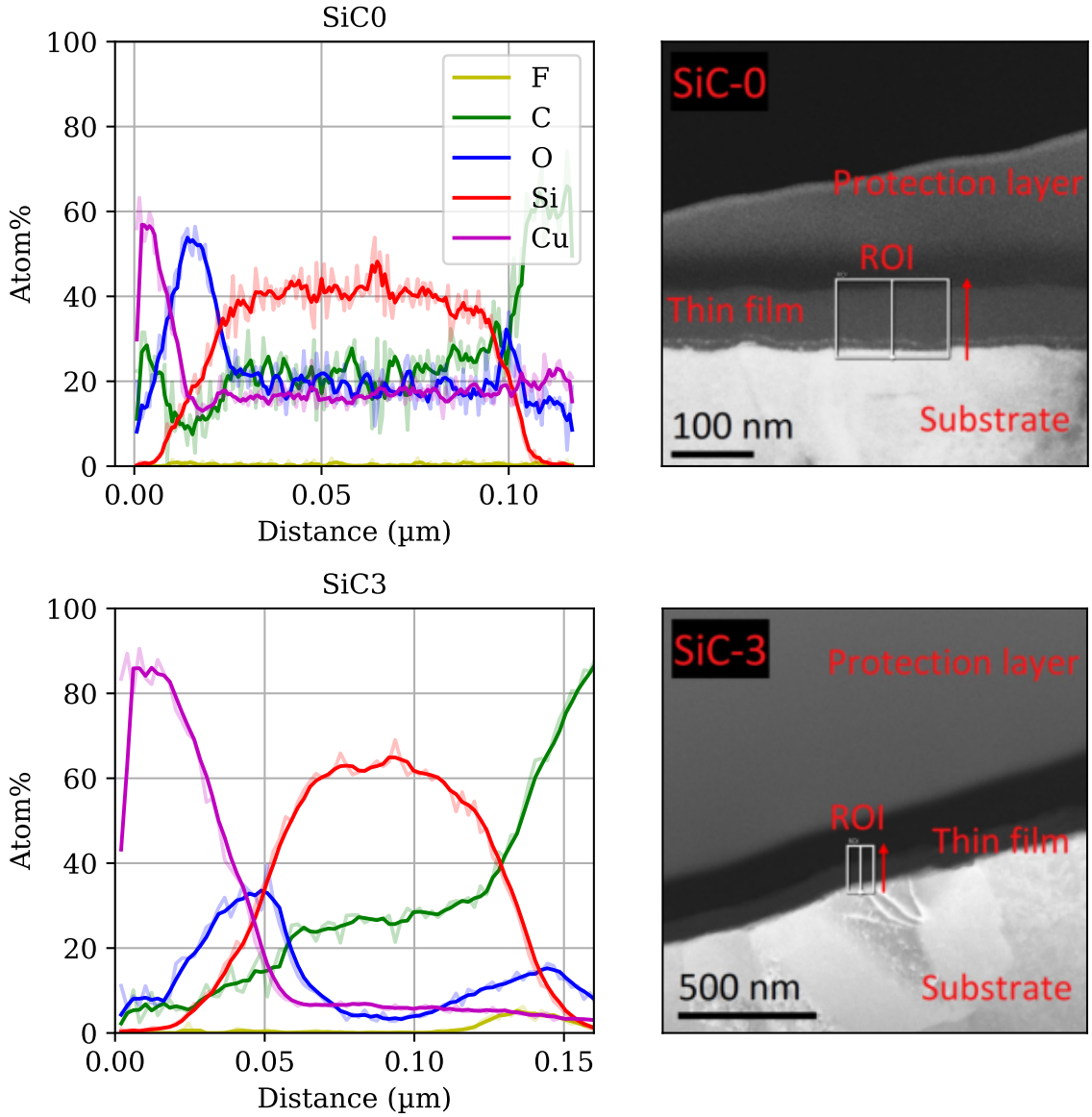

Fig. 4.5.4: Integrated linescan across the film, showing atom % of F, C, O, Si and Cu content (in yellow, green, blue, red and magenta, respectively), of the samples Si-0 and Si-3 with corresponding HAADF STEM images showing the acquisition region. The red arrow indicated the scan direction, i.e. from the Cu foil to the C protection layer. Concentration profiles are smoothed out using a simple algorithm (see Appendix C). The raw data is seen with a brighter contrast behind the graphs. Acquired with the 2100F TEM instrument.

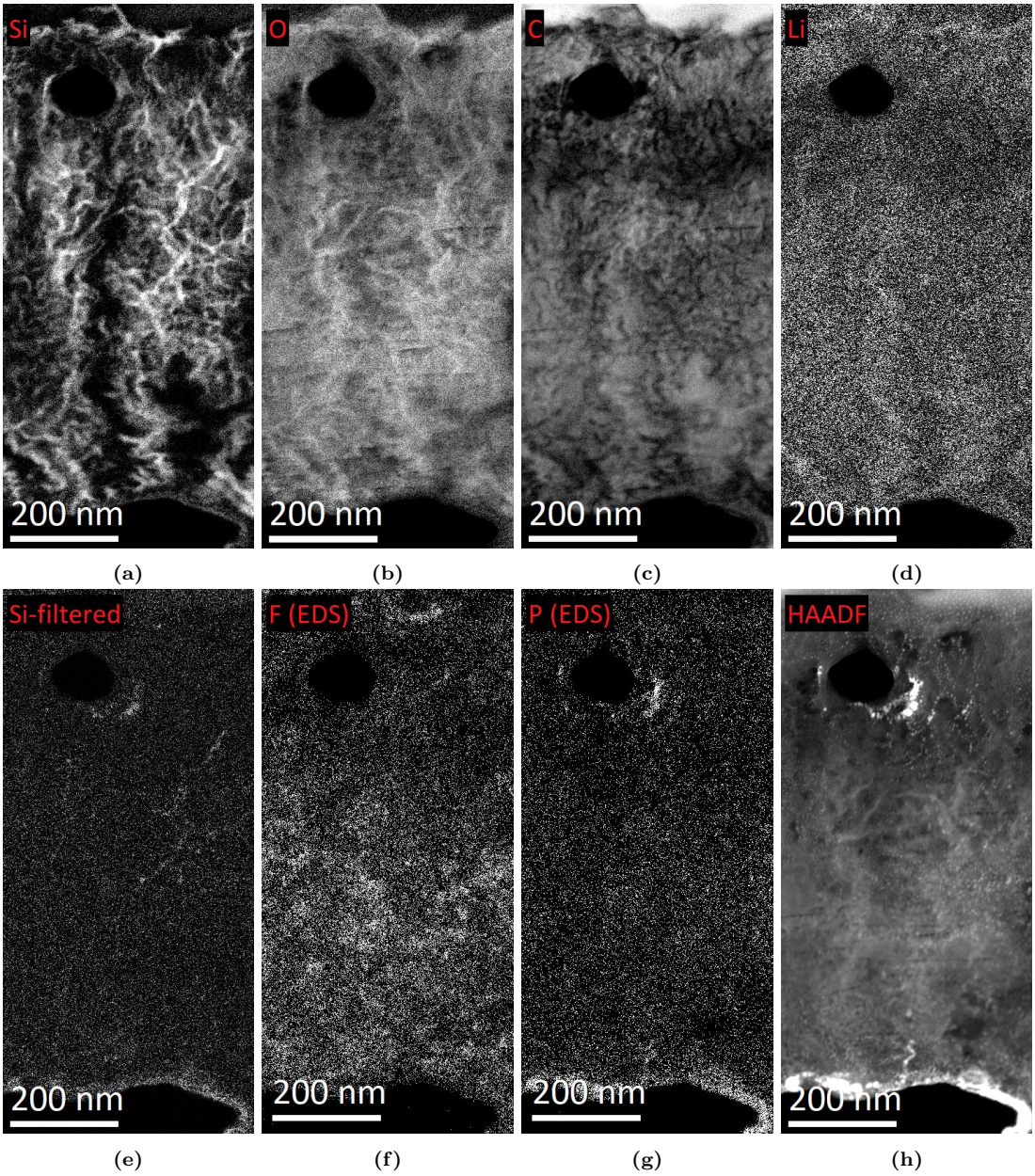

Fig. 4.5.5: EELS and EDS maps of Si-1000 acquired with the ARM200F instrument. Brighter contrast indicates a higher concentration of the relevant element. a) Silicon edge map. b) Oxygen edge map. c) Carbon edge map. d) Lithium edge map. e) Silicon edge map with signals from the energy range 99.25 eV - 102.25 eV. f) Fluorine EDS map. g) Phosphorus EDS map. h) HAADF STEM image acquired during mapping.

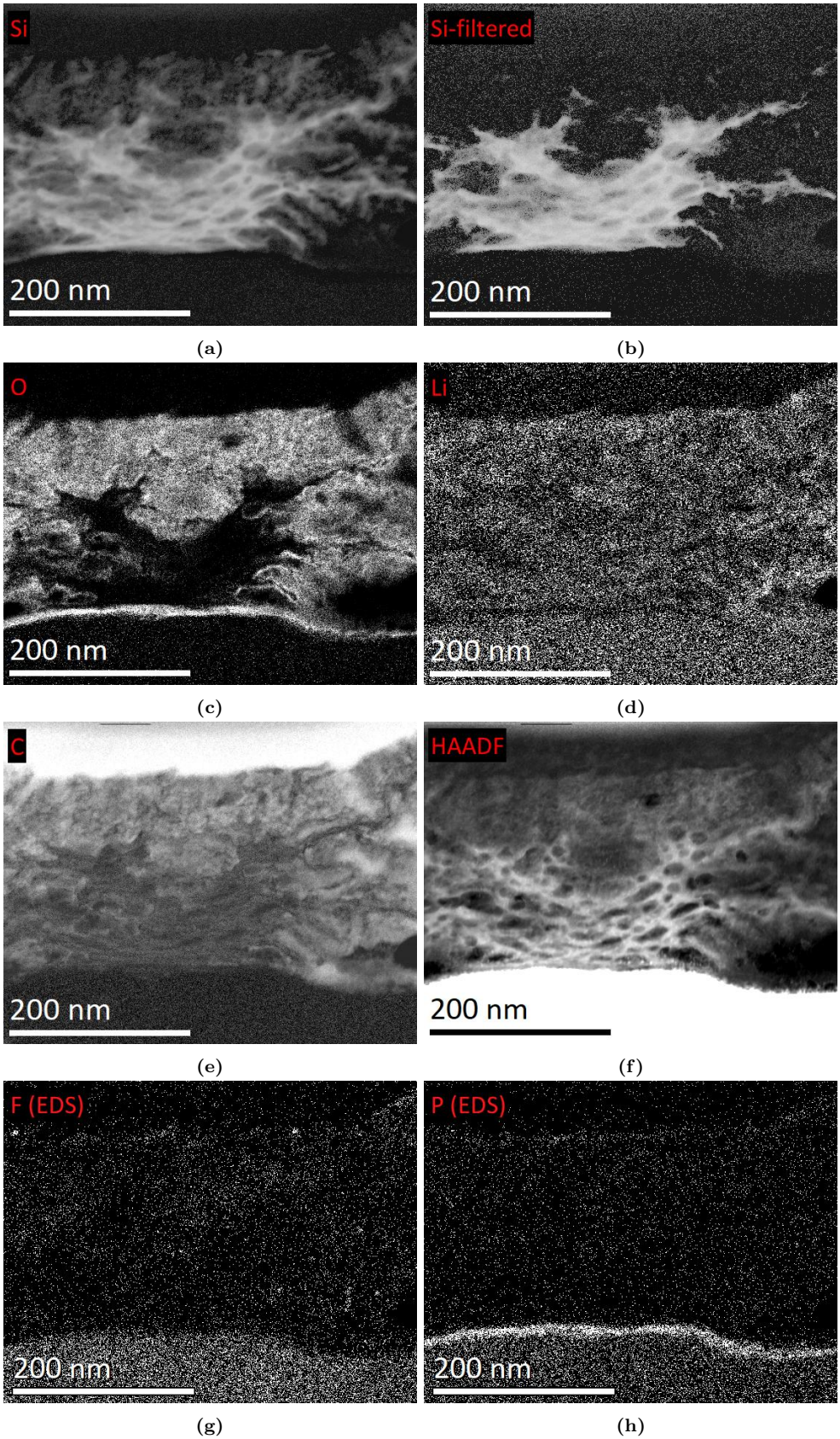

Fig. 4.5.6: EELS and EDS maps of SiC-1000 acquired with the ARM200F instrument. Brighter contrast indicates a higher concentration of the relevant element. a) Silicon edge map. b) Silicon edge map with signals from the energy range 99.4 eV - 102.4 eV. c) Oxygen edge map. d) Lithium edge map. e) Carbon edge map. f) HAADF STEM image acquired during mapping. g) Fluorine EDS map. h) Phosphorus EDS map.

CHAPTER 5

DISCUSSION

5.1 Sources of Error and Uncertainty

5.1.1 Sample Preparation

The quality of the examined samples depend heavily on the sample preparation steps. Variations between the samples, and causes of outliers in cycling data, can have origins in film deposition, cell fabrication, cell opening, and TEM lamella preparation. These will be discussed below

The 4 inch × 4 inch thin film sheets from which the 15 mm discs were punched out, were not homogeneous in thickness, which is seen from the color gradient in the film in Figure 5.1.1. Even though discs used in the test cells were chosen from homogeneous regions of the sheet, they may have small differences in thickness, causing differences in performance. Furthermore, variations within a single disc are considerable, and may still cause local variations. This should be considered, as TEM samples are prepared from 10 µm × 2 µm regions of the 15 mm discs.

Thickness variations of the thin film sheets are believed to originate from the temperature gradients in the substrate during film deposition, caused by an uneven connection between the substrate and the substrate heating plate in the PECVD. The consequence of this is local variations in deposition rate.

After cycling, the cell opening can have caused mechanical deformations on the sample. Upon extracting the working electrode, it was attached to the separator, which had to be peeled off enough for the electrode to be pulled out. In this process, the electrodes were slightly mechanically deformed. Additionally, the remaining electrolyte on the electrode surface solidifies quickly and can add an additional layer on top of the film [37]. The electrodes were therefore washed with dimethyl carbonate subsequent to extraction from the cell, and thus electrolyte solidification was not observed.

(a) (b)

Fig. 5.1.1: The original thin film sheets. The circular holes are where the 15 mm discs used in the coin cells were punched out from. a) Pure Si film. b) SiC_x film.

As mentioned in chapter 3, the samples were transported from the glove box to the FIB-instrument via a sealed plastic bag. However, some air exposure while the sample was mounted to the sample stage before chamber evacuation was unavoidable. Exposure to ambient atmosphere altered the SEI in advance of examination and caused compositional changes, e.g. due to chemical reactions associated with oxidation processes. These may include fluorinated products formed from the dissolution of LiF and $LiPF_6$-products in the presence of water, a general increase of oxygen-containing species, Li-carbonate reacting with carbon dioxide in the air, and $Li_xSi_yO_z$ formation [16, 37, 38].

Alteration of the sample surface was also observed as a change of color from black to orange after exposure of samples Si-3, SiC-3, Si-1000 and SiC-1000. The SiC_x film was orange ahead of cycling, while pure Si film was blue/magenta-colored, as seen in Figure 5.1.1. It could make sense that oxidization of the top layer makes it transparent, revealing the underlying orange color on the SiC_x film, but this would not explain why the pure Si film also became orange.

5.1.2 Measurement Uncertainty

The uncertainty in film thickness measurements is addressed here. The thickness of the six thin films was determined from BF images acquired with the 2100F instrument. The values provided in Table 4.4.1 are averaged from 12 measurements along the TEM lamellae. Thickness was not measured from ARM200F images, as they showed $\sim$ 14 % thinner samples than images from the 2100 and 2100F instruments. The reason for this is likely differences in calibration of the microscopes. Thickness measurements were chosen from the 2100F instrument, as it was the only one to image all six samples, therefore providing consistent results across the samples. It is the relative change of thickness which is of interest in this work, and therefore thickness comparisons across instruments were not included. Moreover, lengths measured with TEM differed from the estimated thicknesses determined with ellipsometry. Si-0 was measured $\sim$ 11 % thinner in TEM, while SiC-0 was measured $\sim$ 21 % thicker in TEM, relative to the ellipsometry measurements. Two plausible causes are presented for the lack of correlation between the ellipsometry and TEM measurements. Because ellipsometry measurements require very flat surfaces, the measurements

were performed on identical films on Si wafers, rather than the actual films. The PECVD deposition rate is estimated to be similar for Si and Cu substrates. Moreover, the same Cauchy fitting model was used on both films, which may have resulted in additional uncertainty as they do not have the same composition. In Appendix D, the ellipsometry fitting done by Marte O. Skare at IFE shows a good match to the experimental data for both films. However, the model is more suited for SiC_x than pure Si, as the substrate is a crystalline Si wafer. Ellipsometry depends on the film and substrate having different optical properties. Thus, it would make sense that there is larger uncertainty for the pure Si film. Lastly, there was an additional layer identified between the thin film and the substrate, containing Zn, P and O. This layer is discussed in the next section, but briefly explained, it is believed to originate from the Cu-foil. Since the ellipsometry measurements were performed on Si wafers which do not have this additional layer, it does not contribute to the ellipsometry measured thicknesses.

Before discussing the spectroscopy results, some sources of error and uncertainty are addressed. The TEM grids were mounted onto the sample holder such that the lamella was pointing towards the EDS detector, with the Cu-finger on the backside, to minimize the amount of spurious Cu-radiation. The holder was also tilted towards the EDS detector to maximize the input rate, but the effect of tilt was negligible. The samples had varying thicknesses, due to difficulties preparing consistent TEM lamellae with FIB. Thicker lamellae give relatively higher re-absorption for low energy peaks in the EDS spectrum, e.g. for carbon and oxygen, compared to e.g. the Cu K peak. In EELS, thicker lamellae give more inelastic scattering that modifies the various peaks differently, as explained in subsection 2.5.2.

The x in SiC_x was determined to ~ 0.53 with data from Table 4.5.1. As explained in the EDS theory in subsection 2.5.1, there is uncertainty related to quantification in EDS. The Aztec software used to analyze the EDS data uses the Cliff-Lorimer equation for quantification [145]. In the conversion from count intensity to atomic concentration, there is uncertainty in the k_{AB} factor in Equation 2.5.1. Parts of this uncertainty comes from thickness variations in the sample, which are not accounted for in k_{AB}. In best case, the uncertainty is ~ 5 %, but often one has to assume $\pm$ 10 % [138]. Still, the obtained composition can indicate trends, e.g. the increase of C, O, F and P in the films after 1000 cycles. The high amounts of Cu are primarily from stray radiation from the Cu TEM grid, as explained in the EDS theory in subsection 2.5.1.

5.2 Characterization of Degradation Mechanisms

This section will discuss the degradation mechanisms observed in the thin films, and give an attempt of explaining the underlying processes.

5.2.1 Before Cycling

Before looking at the effects of cycling, quick attention will be given to the uncycled films. In the SEM images in Figure 4.3.1, Si-0 and SiC-0 are more or less identical in terms of observable

features, i.e. they both have a relatively flat surface with some white spots. The origin and exact composition of these are not clear, but they may be particles with a higher density of Si. However, elemental contrast of secondary electrons is very weak. Most likely the brightness of these spots comes from the increased surface area, from which more secondary electrons can be generated.

In the BF TEM images in Figure 4.4.1, the films are also practically identical. From the bottom, one observes the Cu substrate, an oxygen-rich layer, the film, and the protection layer. The oxygen-rich layer between the substrate and the film is seen as a brighter contrast. The thickness of this layer is measured to 14 nm ±3 nm for Si-0, and 8 nm ±2 nm for SiC-0. The ± indicates thickness variations.

EDS maps in Figures 4.5.1 and 4.5.2 show the distribution of elements in Si-0 and SiC-0. Layers containing Zn and P are seen overlapping the oxygen layer between the film and the substrate. This layer has been observed previously on this type of Cu-foil, and as it is observed to be similar on both films, the effect of this layer is not thought to have caused any difference between the films [146]. The origin of this layer can not be traced back to any source, but it is believed that it is remnants from the production of the Cu-foil. From Table 4.5.1, ~ 5 % of the Si-0 film consists of C, which cannot be correct as the film is supposed to be free from C. The artificial signal may come from the C protection layer deposited ahead of TEM lamella preparation with FIB. The C concentration is predicted to increase as a consequence of cycling, due to SEI formation, but the C concentration in Si-3 is lower than for Si-0. Hence, the hypothesis is that the high C concentration comes from elsewhere than the film. Moreover, carbon contamination may also come from hydrocarbon contamination on the surface. The samples were not plasma cleaned prior to the TEM characterizations. Carbon contamination can also differ from one sample to another. This additional C-concentration should be kept in mind for the other samples as well, e.g. the x in SiC_x, which was found to be ~ 0.53, but may be lower.

A Ga background is observed in all EDS scans, which comes from Ga implantation during sample preparation in the FIB. This is shown in Figure 5.2.1 for sample SiC-1000 as an example. The increase of Ga signal intensity in the substrate region is caused by the higher count rate of Cu. Also, the EDS-based element maps do not only show the signal inside the peaks in the spectra, but also the background signal. The background scales with the overall count rate, hence at the Cu-foil where the count rate is higher than elsewhere, all elements show an artificially higher signal. The increased signal in the protection layer is because the protection layer was made with Ga ion-beam-assisted deposition. This means that large amounts of Ga will be embedded in these layers.

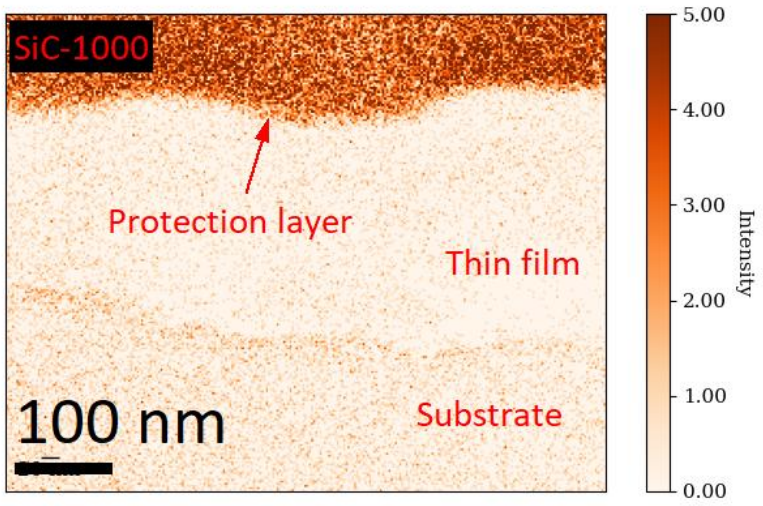

Fig. 5.2.1: EDS map of the Ga signal in sample SiC-1000. The

5.2.2 After 3 Cycles

SEM

Changes in film morphology after the formation-cycles were presented in Figures 4.3.1b and 4.3.1e, in which small differences between the two electrodes are becoming present. Sample Si-3 shows an increased crack formation compared to SiC-3, i.e. it has wider and longer cracks, in addition to a higher density of cracks. The higher frequency and larger width of cracks in the pure Si film were expected, based on previous findings [2, 115]. The increased cracking is directly related to the severe volume expansion of pure silicon, as the amorphous Si structure can expand up to 400 %. The cracking arises as a direct consequence of the formation of other phases during lithiation, which prevents the film from contracting along the same path as the expansion, obstructing the film from preserving its original morphology, as was shown in Figure 2.1.4 and seen in previous studies [44, 45]. This is further discussed below.

TEM

In Figures 4.4.1 and 4.4.2, the corresponding cross-sections were presented. Nano-sized holes are observed in sample SiC-3, unlike Si-3, which has none. Cracks within the sample can have originated from mechanical deformations during electrode extraction from the cell, although this is unlikely to be the cause. As Li-ions diffuse out the film, the film contracts, which may leave holes and cracks. From this explanation, it would be expected that Si-3 had more holes, as it expands more, and can store more Li-ions. The holes became more prominent as the image was slightly defocused to increase the contrast.

Spectroscopy

Figure 5.2.2 shows EELS spectra of the oxide layers and the thin film of SiC-3. The Si $L_{2,3}$ peaks have chemical a shift towards higher energies in the oxide layers. There are silicon oxides on both sides of the film. More specifically, SiO_2 and not SiO. The ionization energy of SiO_2 is known to be $\sim$ 105 eV, while Si is at $\sim$ 99 eV, and SiO is at an intermediate energy around $\sim$ 102 eV [143, 144].

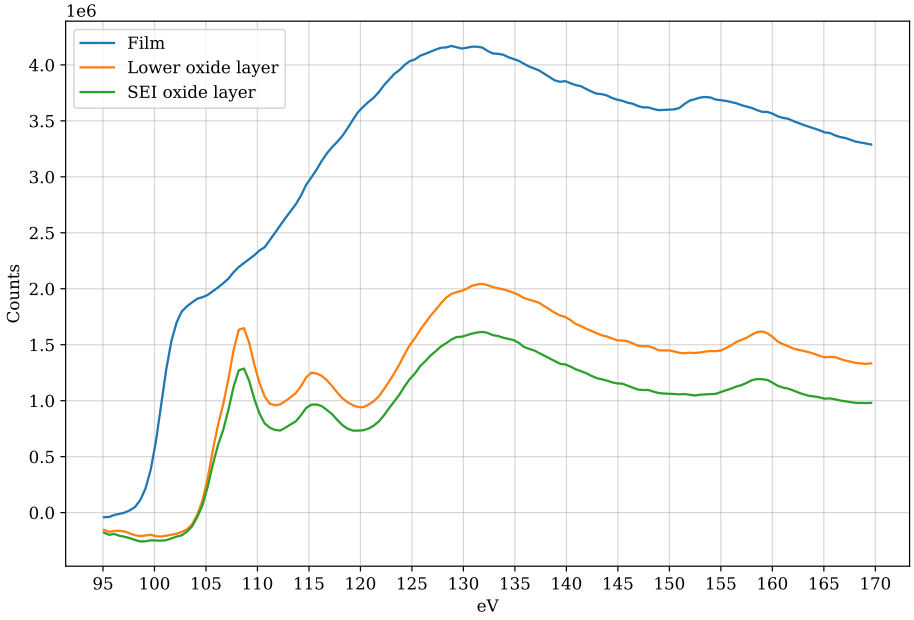

Fig. 5.2.2: Background subtracted EELS spectrum of the Si edges in sample SiC-3, from the two oxygen-rich regions and the middle of the thin film. The signal for the oxide layers drops below 0 counts because of not optimal background subtraction from the original EELS signal. The main message of this figure is the position of the ionization edges.

5.2.3 After 1000 Cycles

SEM

The SEM images in Figures 4.3.1c and 4.3.1f show large changes in surface structure for both films. The large cracks have seemingly grown deeper into the film, as the film has expanded, and the rest of the surface shows general structural deformation and fracturing. This is similar to what was shown in Figure 2.1.4. Degradation has had a larger effect on Si-1000 than SiC-1000. The top surface of the Si-1000 film shows hints of pulverization. SiC_x has degraded less and retained more of its original structure. Although the SEI layer was not directly observable in the SEM images, its presence was evident due to electron beam sensitivity during imaging of the films. SEI phases such as LiF and LiO_x are susceptible to structural changes during electron beam radiation [147]. Thus, the surfaces of Si-1000 and SiC-1000 were seen to change during acquisition of SEM images in Figure 4.3.1. Especially Si-1000 was clearly seen to change as the

electron beam carbon protection layer was deposited. The same effect was observed on SiC-1000 and Si-3 as well, but to a lesser degree.

TEM

The BF TEM images in Figure 4.4.1 show a significant film expansion and deformation of the films. Correspondingly to what was observed in the SEM images, the pure Si film has undergone the largest changes, in addition to delaminating from the substrate. The overview image of Si-1000 in Figure 4.4.1c shows lines with brighter contrast across the film. These are likely porosities created during delithiation. SiC-3 and SiC-1000 show similar behavior. Since Si-1000 had retained a high capacity after 1000 cycles, there must have remained active material to be lithiated/delithiated. These regions with active material expand during lithiation and contract during the following delithiation, leaving additional pores.

The delamination is more clearly seen in Figure 5.2.3. Delamination is thought to be a direct consequence of the volume expansions during cycling. The delamination can also have occurred during opening of the cell and handling of the electrode. Cycling data indicate that delamination has not been a major problem, implying that delamination might have occurred sometime after cycling. SiC-1000 has not delaminated to the same extent, which is most likely related to the smaller volume expansion.

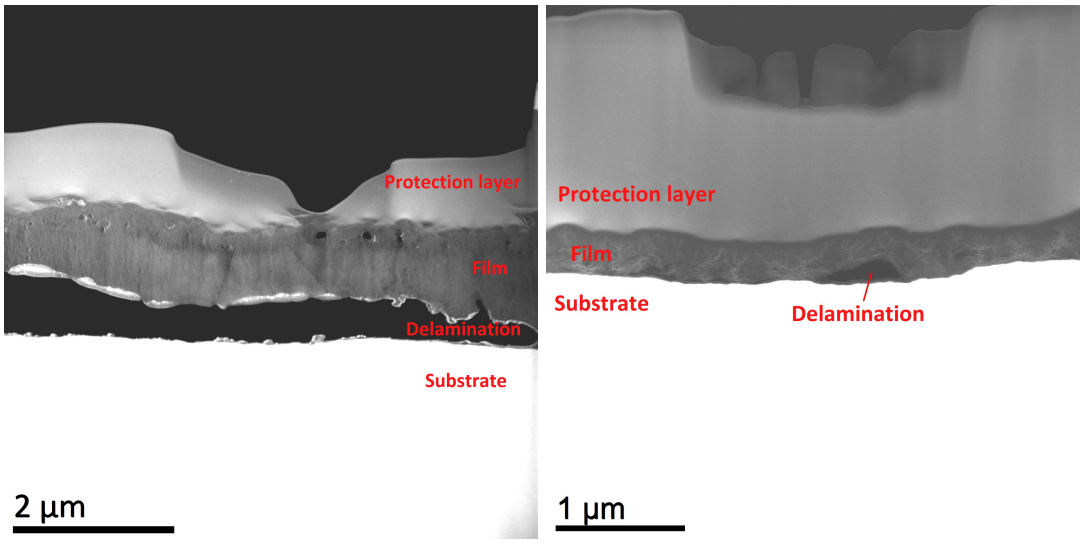

Fig. 5.2.3: HAADF STEM image of samples Si-1000 (a) and SiC-1000 (b), showing delamination of film from the Cu-foil substrate. Images acquired with the ARM200F instrument.

Spectroscopy

Si-1000: This discussion is based on Figure 4.5.5. Note that the energy-filtered maps for Si, map out the oxidation state of the element and not directly its purity. This implies that Si in oxidation state 0 which has alloyed with other elements can still show up in the map for pure Si.

Figure 5.2.4 shows a color map with Si (red), O (blue) and C (green) for Si-1000 and SiC-1000, and will aid the following discussion.

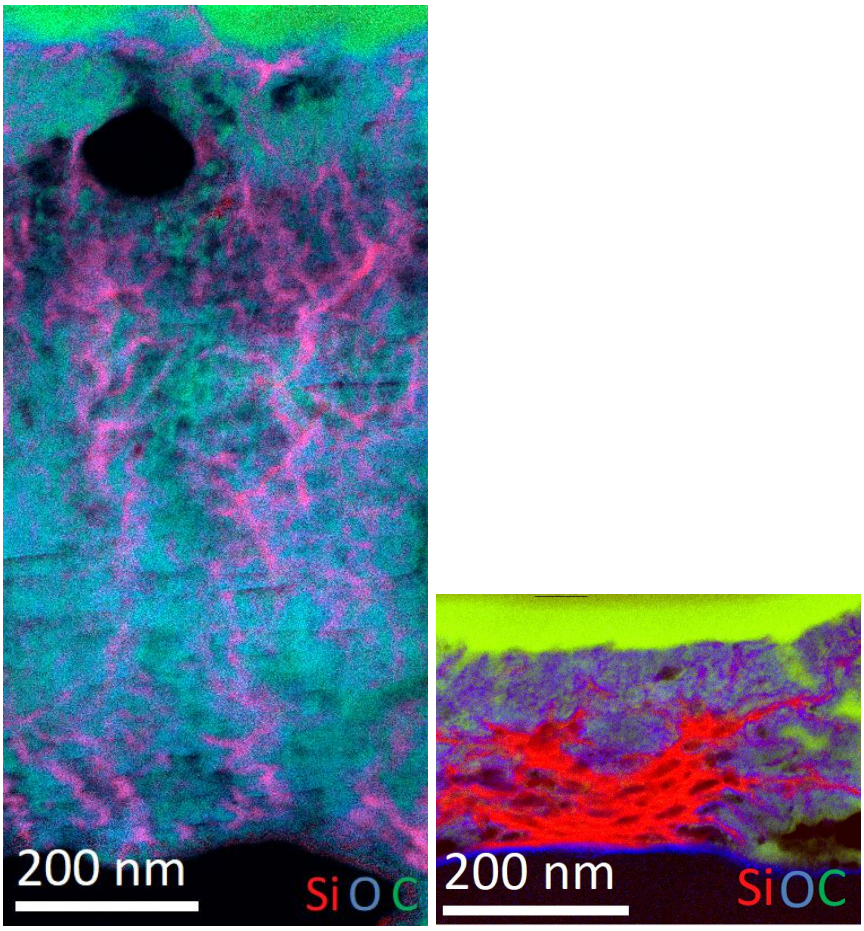

(a) **(b)**

Fig. 5.2.4: EELS color maps of elements Si (red), O (blue) and C (green). a) Si-1000 b) SiC-1000.

Little to no pure silicon is remaining in the sample after 1000 cycles. The ionization edge in the EELS spectrum for silicon has been shifted towards higher energy, indicating alloying with another element, similar to what was shown in Figure 5.2.2 in the oxide and SEI layers. Higher concentrations in the silicon map overlap well with the oxygen map, indicating that silicon oxides have formed as a consequence of the cycling. The underlying mechanisms here are thought to be film cracking, which revealed new surfaces within the film for the electrolyte to form additional SEI. This process has been repeated over 1000 cycles, further assisting the overall film expansion, and preventing it from returning to its initial form. The specific silicon patterns may also be explained as fast lithium diffusion paths, that are assumed to improve the cation diffusion rate, as illustrated in Figure 5.2.5 [47]. The remaining silicon should be regarded as inactive, and not contributing to the capacity of the cell. The cycling data, which will be discussed in the next section disproves the hypothesis that all silicon has become inactive.

Li was observed in Figures 4.5.5d and 4.5.6d, in the form of a continuous Li background throughout the sample. The working electrodes in the cells tested in this work are cycled vs a Li counter electrode, which serves as a practically infinite Li reservoir. In a real battery, e.g. with a layered oxide cathode, Li trapping would be considered a significant issue. This will be discussed further

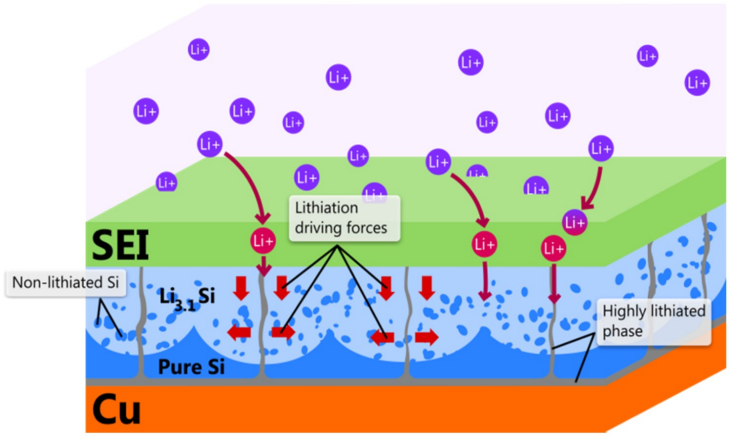

Fig. 5.2.5: Schematic showing the formation of fast diffusion paths in a pure Si thin film on a Cu substrate [47].

in section 5.4. The fast Li diffusion paths are not observed in the EELS map, which makes sense as these paths are unlikely to trap lithium with their high diffusion rates. In general, the low amount of Li corresponds with the fact that the test cells were in their delithiated state when removed from cycling. Hence, all active Li is supposed to have been removed from the working electrode when the cell is opened and therefore not seen in images of the studied electrode. Only passive Li, e.g. in the form of $Li_xSi_yO_z$ Li_xO, LiF, Li_2CO_3 etc, i.e. various SEI phases and trapped Li-ions should be present. Additionally, it can be explained by the thickness of the sample. To efficiently gather Li signals in EELS, the TEM lamella should have been even thinner, to reduce signals from bulk plasmons. These disturb the background removal calculations, and partly overshadow the Li edge in the EELS spectrum. The probability of plasmon excitations is far higher than the probability of exciting Li atoms. Hence, if the lamella was too thick, the Li K-edge would have been buried in the signal from multiple plasmons making it impossible to extract the pure Li signal from the spectra. Additionally, the $M_{2,3}$ ionization edges of some first-row transition metals may overlap with the Li signal [148]. The consequence is an artificial Li signal in the Cu-foil.

The EDS maps of F and P, i.e. Figures 4.5.5f and 4.5.5g, respectively, show further signs of SEI formation. The F map contains regions with higher concentrations which match the regions with higher concentrations of Li, indicating the formation of LiF. Moreover, the suspected LiF regions match where the Si and O maps have lower concentrations. The P map shows a homogeneous concentration in the film, except at the very bottom, and in a region around the hole in the film. The latter does not match any of the other elemental maps, besides the HAADF image. The high concentration at the bottom origins from the aforementioned P, Zn and O rich layer which was observed in the uncycled films.

SiC-1000: This discussion is based on Figure 4.5.6. SiC-1000 is an amorphous substoichiometric silicon carbide thin film. The SiC_x ionization edge is indistinguishable from the pure Si ionization edge, which is why Figure 4.5.6b has more or less signal from the same energy range as Figure 4.5.5e. For simplicity, SiC_x will be referred to as pure Si in this discussion, making it more easily comparable with the Si-1000 discussion.

Compared to Si-1000, SiC-1000 has retained much of its pure Si, which has formed a dendrite-like pattern from the substrate and towards the top of the film. The underlying processes causing this pattern formation are presumably the same as for Si-1000, in terms of cracking, SEI formation and Li trapping. The corresponding oxygen map in Figure 4.5.6c complements the pure Si map, by having an increased concentration where cracks have presumably formed, letting electrolyte in to form new SEI. Between the film and the protection layer, there is a layer with high concentrations of oxygen and oxidized Si, indicating a SEI layer. The same applies to around the pure Si dendrites, where oxygen has entered.

The Li map in Figure 4.5.6d shows regions of increased concentration, but these do not seem to correspond well with the other elemental maps, except for some weak overall similarities with carbon. An increased concentration is also observed in the substrate and the protection layer. This is an artifact likely caused by the increased relative thickness of Cu in the substrate and deposited Ga in the protection layer. Due to their shorter inelastic mean free path compared to the other phases in the sample, these regions have an increased contribution of bulk plasmons that interfere with the background subtraction and create an artificially higher net Li signal.

The EDS maps of F and P were shown in Figures 4.5.6g and 4.5.6h, respectively. F shows a gradually increasing concentration from the bottom to the top of the film. Some small regions of high concentration are observed, but these do not correspond with the other elements. P has a high concentration on top of the substrate, as also seen in the uncycled films, but do otherwise have a homogeneous concentration within the film.

Comments on SEI From the results, there is evidence to believe a formation of the expected SEI phases has occurred, i.e. LiF, Li_xO, Li_2CO_3 and $Li_xSi_yO_z$. No maps had perfect correspondence, which was not expected either, but overlapping regions and change of oxidation state in Si imply the formation of new phases during cycling.

Degradation rates: The difference between the Si-1000 and SiC-1000 need further investigation to understand what causes Si-1000 to seemingly degrade faster. An investigation of the degradation of both films after 20, 50, 100 and 500 cycles to see the degradation rates would have been useful. From this, one would be able to evaluate whether the difference arises from different degradation rates or if there are other underlying mechanisms. It would have been interesting to determine degradation rate as a function of carbon content in the films.

5.3 Consequences of Degradation

5.3.1 Discussion of Cycling Data

This section will relate the observed degradation of both films to the accompanied electrochemical characterization provided in section 4.2. Before discussing the cycling results, recall that these cells are half-cells with a Li metal counter electrode, i.e. the thin film which is an anode in a full-cell becomes the cathode in a half-cell, and will therefore be lithiated during discharging

and delithiated during charging. Note also that the calculated capacities are determined using the thicknesses measured with ellipsometry. The active mass is a product of the thickness, surface area, and estimated mass density. The mass density is estimated based on the atom % from XPS data by Marte O. Skare at IFE. The uncertainties in sample thickness and mass density should be taken into account when comparing with literature and across the films, but do not affect comparisons between charge and discharge capacity.

The first cycle discharge capacity was higher than the charge capacity in both films, as also seen through the initial CE. During the formation-cycles, loss of active material occurs through SEI formation and loss of Li inventory through Li-ion trapping. Upon delithiation, the loss will not contribute to the reversible capacity, as is seen in Figure 5.3.1. As the SEI stabilizes and the full volume of the electrode is activated, the difference between the charge and discharge capacities shrinks, but never becomes the same, as there is a continuous degradation of the battery. The initial CE and total capacity retention were both higher for pure Si than for SiC_x, and could not have been predicted. This is discussed further in the next section.

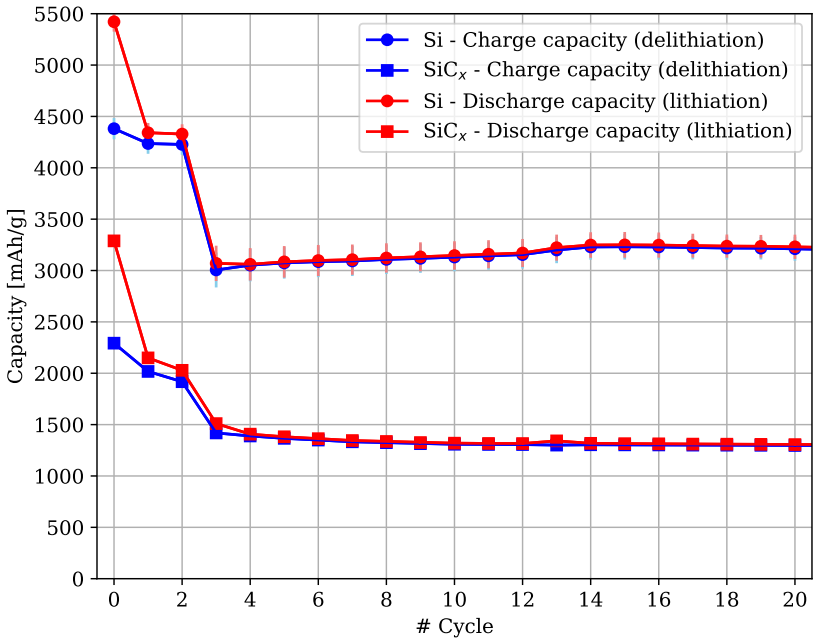

Fig. 5.3.1: Cycling data from section 4.2 cropped to the first 20 cycles. Plotted values are the average of three cells, and the standard deviation from the average is given for each data point in the graph. A significant capacity decay is seen in the formation-cycles.

For the pure Si sample, the reversible capacity was observed to increase between cycles 3 and 15. This is likely caused by a gradual activation of silicon over several cycles, as the aforementioned lithiation front moves into the material, caused by the low conductivity of Si. It is not clear why the same feature was not observed in the SiC_x sample. In similar SiN_x alloy thin film anodes, the nitrogen has been observed to form a matrix for the silicon in the first cycles, in which the material became gradually more activated. Therefore the SiN_x films showed the same increasing capacity as the pure Si sample presented here [18, 149–151]. The C content in the SiC_x film was lower than the N content in the SiN_x films, and may be the reason why this supporting matrix was not formed here.

The pure silicon film begins with a much higher initial capacity than the SiC_x film. This could be expected from the higher theoretical capacity of Si, and the fact that the pure Si films contained more Si than the SiC_x films. The measured initial delithiation capacity for the pure Si film exceeds its theoretical value, which may be explained by the uncertainty in the active mass. The active mass is calculated from the ellipsometry measured thickness. By multiplying the initial specific delithiation capacity with the ratio between the ellipsometry and TEM measured thicknesses from Table 4.4.1, i.e.

$$4381\text{mAhg}^{-1}\frac{66\text{nm}}{80\text{nm}} = 3614\text{mAhg}^{-1},$$

a more realistic capacity is found. This suggests that the TEM thickness measurements are more reliable than the ellipsometry measurements. Equivalently, for the SiC_x film, the new initial specific delithiation capacity becomes

$$2293\text{mAhg}^{-1}\frac{70\text{nm}}{62\text{nm}} = 2589\text{mAhg}^{-1},$$

At the time of writing this thesis, the author was not able to find any publications on the performance of similar SiC_x films which could be quantitatively compared to the results presented here, except in one article by Huang et. al. [115]. In general, it has been found that thinner films yield better capacity retention [21, 44, 45], but in the study by Huang et. al. it was found that thicker SiC_x films have residual SiC due to incomplete reactions, which lower the reaction kinetics, increase hardness and buffer volume changes to improve the mechanical stability and thus the capacity retention. Their results were of comparable thin films, but at 250 nm thickness. Their films were cycled at lower C-rates, and yielded worse capacity retention, presumably because of the films being thicker. From this, it can be speculated to what degree the addition of carbon contributes to improving the cycling stability.

5.3.2 Comparing Cycling Data to Observations

The loss of reversible capacity is directly related to observed SEI formation in the films. The higher initial CE and total capacity retention of pure Si over SiC_x could not have been predicted from the presented SEM, TEM and EELS results. SiC_x seems to be more intact and should have exhibited more stable cycling results. The capacity loss due to Li trapping, thus loss of Li inventory, is assumed to be very low because the films are cycled vs a Li metal electrode, which serves as an infinite Li reservoir. This is very likely the reason why the pure Si film was able to perform better than the SiC_x film, despite the significant structural and chemical changes after 1000 cycles. That said, trapped Li does take up space which could have been used to host additional Li. For this reason, the main cause of capacity loss is related to the loss of active material, which was seen in the form of Si conversion in both films, but more distinctly in Si-1000. Si conversion refers to the conversion of pure Si to Si oxides and SEI components such as $Li_xSi_yO_z$. It is the Si which forms an alloy with Li, and is responsible for the reversible capacity in the cell. Therefore, loss of active silicon leads to a CE below 100 %. The Si was

observed to form oxides and contribute to the SEI, which further trap additional Li. Strangely, the pure silicon film retained a reversible capacity higher than the SiC_x film over 1000 cycles, from which it can be interpreted that the converted silicon is still active. This must not be confused with other degradation mechanisms such as loss of Li inventory, i.e. Li lost to Li trapping and formation of SEI phases.

With section 2.1.4 about silicon oxide anodes in mind, there is reason to believe that the oxidized silicon in the cycled films still is active. Thus, it can have retained its electrochemical activity and not become inert, as first assumed. The exact consequences are still unclear, but this would explain the capacity retention after the conversion of pure Si.

On a side note, it can not be overlooked that the examined regions might have been outliers and not representative of the rest of the films. The PECVD deposited amorphous films are assumed to be homogeneous, but local variations of density and composition may have favored certain regions for electrochemical activity. Therefore other areas than the chosen one may have been less affected by the cycling. From SEM inspections of the cycled films, their surfaces showed little to no local variations. Some regions had slightly higher frequencies of cracks, but not enough to be of any significance. Therefore, the region from which TEM samples were prepared, was arbitrary. That said, the surface morphology is not necessarily representable for sub-surface variations.

Finally, Si-1000 was observed to have strongly delaminated from its substrate, which should break the electrical contact and be visible in terms of a capacity loss. Seen in terms of what was discussed on local thickness variations, the film has likely retained electrical contact elsewhere in the cell. TEM samples are prepared from a very small region of the 15 mm electrode, i.e. the region of interest may not have been representable for the rest of the cell. The delamination could also have occurred during the opening of the coin cell, as previously mentioned.

5.4 Utilizing Silicon Anodes in Full-Scale Full-Cell Batteries

This section will handle the challenges related to applying amorphous silicon and SiC_x thin film in commercial LIBs. The cycling data presented in the previous section may seem promising, but before these materials are used commercially, several issues should be addressed. Before the following discussion, the reader is reminded of the purpose of using thin films in this work. Thin films have been applied as a model to accurately test new materials in a controlled reproducible environment. The intention has not been to develop thin film anodes, but rather to use thin films as a convenient approach to acquiring high-quality and reliable results. The ultimate goal is and has in this project been to build up an understanding of the degradation mechanisms, and apply the knowledge to production e.g. of powder/particle-based anodes. That said, the discussion below will also briefly look into the possibilities of applying thin films in commercial batteries.

Thin films offer significantly shorter electron transfer and Li diffusion pathways because of their

large surface-area to volume ratios, which yield rapid lithiation and delithiation. This would mean faster charging and discharging rates. Additionally, thin films better accommodate mechanical stresses, and are for that reason less susceptible to cracking, pulverization and delamination from the current collector [2, 21, 22]. This is because crack formations are mitigated by the small dimension of the film. Commercial battery packs consist of hundreds to thousands of cells in serial and parallel circuits. Compared to commercially used battery cells, the coin-type half-cells used in this work have low active masses, and thus for a battery pack to keep the same total capacity, it would have to include a lot of cells. Each cell consists also of a separator, electrolyte, counter electrode, spacer, spring and casing, meaning that the volume of the battery pack would also increase significantly. Using a bulk electrode would yield more active mass per cell volume. Going from thin films to bulk introduces several issues. The increased diffusion length of bulk anodes increases the frequency of Li trapping within inactive material.

Lithium trapping is an acknowledged degradation mechanism that is typically due to either slow Li release kinetics, formation of highly stable lithiated compounds or strong bonding with less coordinated atoms at defect sites [7, 51, 152]. For Si anodes, in particular, Li trapping contributes to ~ 30 % of the initial Li loss in the first cycle [153]. Coatings have been shown to mitigate this effect, but other than that, little research seems to have been done directly on Li trapping [3,154]. In commercial batteries, all Li is added via the cathode, and additional Li from the electrolyte's conductive salts, e.g. $LiPF_6$. Therefore, trapped Li will considerably reduce the capacity of the battery, and cause it to quickly degrade. One alternative route around it is pre-lithiation which serves to compensate for irreversible capacity in the first cycle. Pre-lithiation of the anode can be classified into anode pre-lithiation reagents, electrochemical pre-lithiation and chemical pre-lithiation, each with their advantages and disadvantages [155,156]. Other solutions to accommodate the loss of Li inventory involve using anodes with overcapacity compared to the cathode, or by performing formation cycles, and moving the anode to a new cell. Hence the irreversible capacity loss is already accommodated for. Finally, an elegant solution to regain trapped Li-ions is to reduce the cycling rate. Lowering the current density provides additional time for trapped ions to diffuse through the electrode and contribute to the reversible capacity. This latter strategy does not work for irreversibly bound Li-ions in SEI, as these have formed phases, and cannot be regained by simply giving more time.

In this work capacity loss due to Li trapping was more or less neglected because a Li metal counter electrode, providing a practically infinite supply of Li. Commercially using Li metal as the anode would mitigate the consequences of Li trapping, but as mentioned in the theory section, Li metal anodes are highly susceptible to dendrite growth which can penetrate the separator and shortcut the cell. Li plating, which is more relevant for LIBs, was not observed in this work, because of the small amount of Li required to fill the total capacity of the thin films. That said, the cycling voltage window is the principal determinant of Li plating. Low voltages facilitate Li plating, as explained in the theory, section 2.1.4.

A final suggested approach to improving battery performance is to separate the silicon and carbon into separate phases, e.g. composite anodes. Composites of Si and C have been a hot topic within LIB research, and multiple approaches have been studied [3, 22, 48, 157–163]. To

summarize, Si-C composites have been produced with techniques ranging from variations of CVD to ball milling and spray drying, of which some are good alternatives for commercial production while others are not cost-effective and far too complex. The many benefits of composites include improved lithiation kinetics, strengthening the structural stability and preventing loss of active material and lithium inventory. These improve the initial CE, overall reversible capacity, and charge and discharge rates. Strengthening of structural stability implies improving adhesion to the current collector and or connection to a conductive network and boosting the crack resistance, both by preventing crack formation and by mitigating volume expansions. A driving factor for composite electrodes is to benefit from the strengths of each component. Silicon offers high capacity but suffers in terms of cycling stability, and vice versa with graphite. Additionally, graphite is an active material which can also contribute to the total capacity. The design of the composite must also consider its intended application, e.g. EVs for urban environments. In this particular example, the EV will unlikely completely discharge between every charging. For this application, a composite anode could be designed to primarily use graphite for high cycling stability, and then activate the silicon when additional capacity is required, but with the cost of faster degradation. Silicon has also become an attractive anode material for extraterrestrial application, e.g. mars rovers, which need high capacities for a limited amount of cycles [164,165].

As an ending remark, it can not be overlooked that new innovative technologies and concepts are still limited by the existing and available production lines. This limits fast adoption of new technology and materials. Hence, the most accessible strategy is a gradual improvement of the components used in LIBs.

CHAPTER 6

CONCLUSION

The degradation mechanisms of PECVD deposited amorphous silicon and substoichiometric silicon carbide thin films on Cu substrate have been investigated. From each film, one uncycled sample, one sample cycled 3 charge/discharge cycles, and one 1000 cycles were investigated via galvanostatic cycling in half-cell configuration with a Li metal counter electrode. SEM revealed morphological changes after 3 cycles in terms of minor surface cracks. After 1000 cycles, both films exhibited electron beam sensitivity due to SEI formation, and significant changes in morphology, as a consequence of lithiation and delithiation. TEM, EDS and EELS characterization of the FIB-prepared TEM lamella revealed that an SEI layer had formed on top of the films after 3 cycles. The pure Si and the SiC_x films had expanded by 13 % and 8 % after 3 cycles, respectively. After 1000 cycles, the respective films had expanded by 1600 % and 540 % from their initial thickness. TEM and STEM imaging showed almost complete delamination from substrate for the pure Si film, and minor delamination for the SiC_x film. EELS revealed that considerable amounts of the Si had been oxidized. Silicon paths across the film were observed in the pure Si film. In the SiC_x film, the silicon had spread out in a dendrite-looking manner. Based on EELS and EDS, there is reason to believe that SEI phases LiF, Li_xO, Li_2CO_3 and $Li_xSi_yO_z$ were formed.

The pure Si film had better capacity retention than the SiC_x. The initial CEs were 81 % and 70 % for the Si and SiC_x films, respectively. After 1000 cycles, the respective films had a total capacity retention of 41 % and 30 %. The better performance of the pure Si film is thought to come from the near-infinite Li supply from the Li counter electrode. Therefore, loss of Li inventory was neglected as a cause of capacity loss. Hence, noticeable loss of capacity was owed to loss of active material. Speculations were raised concerning local variations in the films. Finally, a discussion stated some of the challenges related to commercialization of Si in LIBs. Nano-sized features, coatings and composites are observed to improve the performance of Si anodes, by improving mechanical stability and mitigating loss of Li inventory and of active material.

CHAPTER 7

FURTHER WORK

This thesis has been a part of the SEAMLESS project at IFE and hence recommendations for further work may overlap with already planned activities. For the continuation of the work in this thesis, the following is advised:

- To achieve a seamless overview of the effect of thin film thickness and carbon content in the thin films, it is recommended to evaluate additional thin films with other combinations of thickness and composition. The work is already initiated in the SEAMLESS project, and the result from this thesis should provide as complementary to the SEAMLESS project.
- The observed effects of degradation in SEM, TEM, EDS and EELS should be evaluated with results from additional electrochemical characterization techniques, such as dQ/dV.
- All the samples investigated had been exposed to ambient conditions prior to characterization (except galvanostatic cycling of course), which has impacted the chemical composition of the thin films and the SEI layer. It is advised to take advantage of an inert transfer chamber, to prevent exposure to ambient atmosphere ahead of characterization. The results portray a more accurate image of the underlying degradation mechanisms, and should also be used to clarify the consequences of exposure before characterization.
- TEM samples should be prepared thinner, to avoid bulk plasmon peaks in the EELS spectrum, which complicate the background subtraction for the Li ionization edge.
- The significance of local variations within a single electrode is still unknown. If time and resources are sufficient, TEM samples should be prepared from multiple regions, to investigate local changes, and what may have caused these.
- Speculations were also raised towards the degradation rate of the two films. Stopping cycling of a film after e.g. 20, 50, 100 and 500 cycles could give useful insight into the degradation rates and steps, as a function of thickness and composition.

BIBLIOGRAPHY

[1] Duc Hong Vo, Anh The Vo, Chi Minh Ho, and Ha Minh Nguyen. The role of renewable energy, alternative and nuclear energy in mitigating carbon emissions in the cptpp countries. *Renewable Energy*, 161:278–292, 2020.

[2] Mohammed Salah, Colin Hall, Candice Francis, Greg Rollo-Walker, and Manrico Fabretto. Binary silicon-based thin-film anodes for lithium-ion batteries: A review. *Journal of Power Sources*, 520:230871, 2022.

[3] Xiuyun Zhao and Vesa-Pekka Lehto. Challenges and prospects of nanosized silicon anodes in lithium-ion batteries. *Nanotechnology*, 32(4):042002, 2020.

[4] Yeru Liang, Chen-Zi Zhao, Hong Yuan, Yuan Chen, Weicai Zhang, Jia-Qi Huang, Dingshan Yu, Yingliang Liu, Maria-Magdalena Titirici, Yu-Lun Chueh, et al. A review of rechargeable batteries for portable electronic devices. *InfoMat*, 1(1):6–32, 2019.

[5] J-M Tarascon and Michel Armand. Issues and challenges facing rechargeable lithium batteries. *Nature*, 414(6861):359–367, 2001.

[6] Yongming Sun, Nian Liu, and Yi Cui. Promises and challenges of nanomaterials for lithium-based rechargeable batteries. *Nature Energy*, 1(7):1–12, 2016.

[7] Qing Ai, Deping Li, Jianguang Guo, Guangmei Hou, Qing Sun, Qidi Sun, Xiaoyan Xu, Wei Zhai, Lin Zhang, Jinkui Feng, et al. Artificial solid electrolyte interphase coating to reduce lithium trapping in silicon anode for high performance lithium-ion batteries. *Advanced Materials Interfaces*, 6(21):1901187, 2019.

[8] Zachary P Cano, Dustin Banham, Siyu Ye, Andreas Hintennach, Jun Lu, Michael Fowler, and Zhongwei Chen. Batteries and fuel cells for emerging electric vehicle markets. *Nature Energy*, 3(4):279–289, 2018.

[9] Bruce Dunn, Haresh Kamath, and Jean-Marie Tarascon. Electrical energy storage for the grid: A battery of choices. *Science*, 334(6058):928–935, 2011.

[10] Michel Armand, Peter Axmann, Dominic Bresser, Mark Copley, Kristina Edström, Christian Ekberg, Dominique Guyomard, Bernard Lestriez, Petr Novák, Martina Petranikova, Willy Porcher, Sigita Trabesinger, Margret Wohlfahrt-Mehrens, and Heng Zhang. Lithium-ion batteries – current state of the art and anticipated developments. *Journal of Power Sources*, 479:228708, 2020.

[11] Kostiantyn Turcheniuk, Dmitry Bondarev, Vinod Singhal, and Gleb Yushin. Ten years left to redesign lithium-ion batteries, 2018.

[12] Jessie Frazelle. Battery day: a closer look at the technology that makes portable electronics possible. *Queue*, 18(5):5–25, 2020.

[13] Retrieved from https://kommunikasjon.ntb.no/pressemelding/cenate-starter-bygging-av-fullskala-pilotreaktor-for-nano-silisium-til-li-batterier?publisherId=17847786&releaseId=17909260. Accessed 04.06.2022.

[14] Retrieved from https://www.cenate.com/news/. Accessed 03.06.2022.

[15] Yue Qi and Stephen J Harris. In situ observation of strains during lithiation of a graphite electrode. *Journal of The Electrochemical Society*, 157(6):A741, 2010.

[16] Kjell W Schroder, Hugo Celio, Lauren J Webb, and Keith J Stevenson. Examining solid electrolyte interphase formation on crystalline silicon electrodes: influence of electrochemical preparation and ambient exposure conditions. *The Journal of Physical Chemistry C*, 116(37):19737–19747, 2012.

[17] Reiner Korthauer. *Lithium-ion batteries: basics and applications*. Springer, 2018.

[18] Asbjørn. Ulvestad. *Performance and Characteristics of Silicon Nitride as a Convertible Alloy Anode Material for Li-ion Batteries*. PhD thesis, UIO, 2018.

[19] Pallavi Verma, Pascal Maire, and Petr Novák. A review of the features and analyses of the solid electrolyte interphase in li-ion batteries. *Electrochimica Acta*, 55(22):6332–6341, 2010.

[20] Yuping Wu. *Lithium-ion batteries: Fundamentals and Applications*, volume 4. CRC press, 2015.

[21] Mohammed Salah, Peter Murphy, Colin Hall, Candice Francis, Robert Kerr, and Manrico Fabretto. Pure silicon thin-film anodes for lithium-ion batteries: A review. *Journal of Power Sources*, 414:48–67, 2019.

[22] Aliya Mukanova, Albina Jetybayeva, Seung-Taek Myung, Sung-Soo Kim, and Zhumabay Bakenov. A mini-review on the development of si-based thin film anodes for li-ion batteries. *Materials Today Energy*, 9:49–66, 2018.

[23] Jianping Yang, Yun-Xiao Wang, Shu-Lei Chou, Renyuan Zhang, Yanfei Xu, Jianwei Fan, Wei-xian Zhang, Hua Kun Liu, Dongyuan Zhao, and Shi Xue Dou. Yolk-shell silicon-mesoporous carbon anode with compact solid electrolyte interphase film for superior lithium-ion batteries. *Nano Energy*, 18:133–142, 2015.

[24] Wenyue Li, Yongbing Tang, Wenpei Kang, Zhenyu Zhang, Xia Yang, Yu Zhu, Wenjun Zhang, and Chun-Sing Lee. Core–shell si/c nanospheres embedded in bubble sheet-like carbon film with enhanced performance as lithium ion battery anodes. *Small*, 11(11):1345–1351, 2015.

[25] Yan Yao, Matthew T McDowell, Ill Ryu, Hui Wu, Nian Liu, Liangbing Hu, William D Nix, and Yi Cui. Interconnected silicon hollow nanospheres for lithium-ion battery anodes with long cycle life. *Nano letters*, 11(7):2949–2954, 2011.

[26] Mi-Hee Park, Min Gyu Kim, Jaebum Joo, Kitae Kim, Jeyoung Kim, Soonho Ahn, Yi Cui, and Jaephil Cho. Silicon nanotube battery anodes. *Nano letters*, 9(11):3844–3847, 2009.

[27] Hui Wu, Gerentt Chan, Jang Wook Choi, Ill Ryu, Yan Yao, Matthew T McDowell, Seok Woo Lee, Ariel Jackson, Yuan Yang, Liangbing Hu, et al. Stable cycling of double-walled silicon nanotube battery anodes through solid–electrolyte interphase control. *Nature nanotechnology*, 7(5):310–315, 2012.

[28] Fang Dai, Ran Yi, Hui Yang, Yuming Zhao, Langli Luo, Mikhail L Gordin, Hiesang Sohn, Shuru Chen, Chongmin Wang, Sulin Zhang, et al. Minimized volume expansion in hierarchical porous silicon upon lithiation. *ACS applied materials & interfaces*, 11(14):13257–13263, 2019.

[29] Mingqi Li, Yan Yu, Jing Li, Baoling Chen, Aishuak Konarov, and P Chen. Fabrication of graphene nanoplatelets-supported siox-disordered carbon composite and its application in lithium-ion batteries. *Journal of Power Sources*, 293:976–982, 2015.

[30] Xiaolin Li, Meng Gu, Shenyang Hu, Rhiannon Kennard, Pengfei Yan, Xilin Chen, Chongmin Wang, Michael J Sailor, Ji-Guang Zhang, and Jun Liu. Mesoporous silicon sponge as an anti-pulverization structure for high-performance lithium-ion battery anodes. *Nature communications*, 5(1):1–7, 2014.

[31] Taeseup Song, Jianliang Xia, Jin-Hyon Lee, Dong Hyun Lee, Moon-Seok Kwon, Jae-Man Choi, Jian Wu, Seok Kwang Doo, Hyuk Chang, Won Il Park, et al. Arrays of sealed silicon nanotubes as anodes for lithium ion batteries. *Nano letters*, 10(5):1710–1716, 2010.

[32] George E Blomgren. The development and future of lithium ion batteries. *Journal of The Electrochemical Society*, 164(1):A5019, 2016.

[33] Thomas B Reddy. *Linden's handbook of batteries*. McGraw-Hill Education, 2011.

[34] Seong Jin An, Jianlin Li, Zhijia Du, Claus Daniel, and David L Wood III. Fast formation cycling for lithium ion batteries. *Journal of Power Sources*, 342:846–852, 2017.

[35] Hanna Bryngelsson, Mårten Stjerndahl, Torbjörn Gustafsson, and Kristina Edström. How dynamic is the sei? *Journal of Power Sources*, 174(2):970–975, 2007.

[36] Perla B Balbuena and Yi Xuan Wang. *Lithium-ion batteries: solid-electrolyte interphase*. World Scientific, 2004.

[37] Sara Malmgren, Katarzyna Ciosek, Rebecka Lindblad, Stefan Plogmaker, Julius Kühn, Håkan Rensmo, Kristina Edström, and Maria Hahlin. Consequences of air exposure on the lithiated graphite sei. *Electrochimica Acta*, 105:83–91, 2013.

[38] Mengyun Nie, Daniel P Abraham, Yanjing Chen, Arijit Bose, and Brett L Lucht. Silicon solid electrolyte interphase (sei) of lithium ion battery characterized by microscopy and spectroscopy. *The Journal of Physical Chemistry C*, 117(26):13403–13412, 2013.

[39] William M Haynes, David R Lide, and Thomas J Bruno. *CRC handbook of chemistry and physics*. CRC press, 2016.

[40] K.M. Abraham. Directions in secondary lithium battery research and development. *Electrochimica Acta*, 38(9):1233–1248, 1993.

[41] Peng Bai, Ju Li, Fikile R Brushett, and Martin Z Bazant. Transition of lithium growth mechanisms in liquid electrolytes. *Energy & Environmental Science*, 9(10):3221–3229, 2016.

[42] Xin-Bing Cheng, Rui Zhang, Chen-Zi Zhao, and Qiang Zhang. Toward safe lithium metal anode in rechargeable batteries: a review. *Chemical reviews*, 117(15):10403–10473, 2017.

[43] Christian Julien, Alain Mauger, Ashok Vijh, and Karim Zaghib. Lithium batteries. In *Lithium batteries*. Springer, 2016.

[44] Matthew T McDowell, Seok Woo Lee, William D Nix, and Yi Cui. 25th anniversary article: understanding the lithiation of silicon and other alloying anodes for lithium-ion batteries. *Advanced Materials*, 25(36):4966–4985, 2013.

[45] Uday Kasavajjula, Chunsheng Wang, and A John Appleby. Nano-and bulk-silicon-based insertion anodes for lithium-ion secondary cells. *Journal of power sources*, 163(2):1003–1039, 2007.

[46] Daniel Uxa, Bujar Jerliu, Erwin Huger, Lars Dorrer, Michael Horisberger, Jochen Stahn, and Harald Schmidt. On the lithiation mechanism of amorphous silicon electrodes in li-ion batteries. *The Journal of Physical Chemistry C*, 123(36):22027–22039, 2019.

[47] Arnaud Bordes, Eric De Vito, Cedric Haon, Christophe Secouard, Alexandre Montani, and Philippe Marcus. Investigation of lithium insertion mechanisms of a thin-film si electrode by coupling time-of-flight secondary-ion mass spectrometry, x-ray photoelectron spectroscopy, and focused-ion-beam/sem. *ACS applied materials and interfaces*, 7(50):27853–27862, 2015.

[48] Aliya Mukanova, Arailym Nurpeissova, Arshat Urazbayev, Sung-Soo Kim, Maksym Myronov, and Zhumabay Bakenov. Silicon thin film on graphene coated nickel foam as an anode for li-ion batteries. *Electrochimica Acta*, 258:800–806, 2017.

[49] Pimpa Limthongkul, Young-Il Jang, Nancy J Dudney, and Yet-Ming Chiang. Electrochemically-driven solid-state amorphization in lithium-silicon alloys and implications for lithium storage. *Acta Materialia*, 51(4):1103–1113, 2003.

[50] Dominique Larcher, Shane Beattie, Mathieu Morcrette, Kristina Edstroem, Jean-Claude Jumas, and Jean-Marie Tarascon. Recent findings and prospects in the field of pure metals as negative electrodes for li-ion batteries. *Journal of Materials Chemistry*, 17(36):3759–3772, 2007.

[51] Wei-Jun Zhang. A review of the electrochemical performance of alloy anodes for lithium-ion batteries. *Journal of Power Sources*, 196(1):13–24, 2011.

[52] Loïc Baggetto and Peter HL Notten. Lithium-ion (de) insertion reaction of germanium thin-film electrodes: An electrochemical and in situ xrd study. *Journal of the Electrochemical Society*, 156(3):A169, 2009.

[53] Xiao Hua Liu, Shan Huang, S Tom Picraux, Ju Li, Ting Zhu, and Jian Yu Huang. Reversible nanopore formation in ge nanowires during lithiation–delithiation cycling: An in situ transmission electron microscopy study. *Nano letters*, 11(9):3991–3997, 2011.

[54] Wentao Liang, Hui Yang, Feifei Fan, Yang Liu, Xiao Hua Liu, Jian Yu Huang, Ting Zhu, and Sulin Zhang. Tough germanium nanoparticles under electrochemical cycling. *Acs Nano*, 7(4):3427–3433, 2013.

[55] Ali Reza Kamali and Derek J Fray. Tin-based materials as advanced anode materials for lithium ion batteries: a review. *Rev. Adv. Mater. Sci*, 27(1):14–24, 2011.

[56] Bote Zhao, Ran Ran, Meilin Liu, and Zongping Shao. A comprehensive review of li4ti5o12-based electrodes for lithium-ion batteries: The latest advancements and future perspectives. *Materials Science and Engineering: R: Reports*, 98:1–71, 2015.

[57] Hong Huang, EM Kelder, L Chen, and J Schoonman. Electrochemical characteristics of sn1- xsixo2 as anode for lithium-ion batteries. *Journal of power sources*, 81:362–367, 1999.

[58] Bo Gao, S Sinha, L Fleming, and O Zhou. Alloy formation in nanostructured silicon. *Advanced Materials*, 13(11):816–819, 2001.

[59] Bingkun Guo, Jie Shu, Zhaoxiang Wang, Hong Yang, Lihong Shi, Yinong Liu, and Liquan Chen. Electrochemical reduction of nano-sio2 in hard carbon as anode material for lithium ion batteries. *Electrochemistry Communications*, 10(12):1876–1878, 2008.

[60] Jang Wook Choi and Doron Aurbach. Promise and reality of post-lithium-ion batteries with high energy densities. *Nature Reviews Materials*, 1(4):1–16, 2016.

[61] Jin-Yi Li, Quan Xu, Ge Li, Ya-Xia Yin, Li-Jun Wan, and Yu-Guo Guo. Research progress regarding si-based anode materials towards practical application in high energy density li-ion batteries. *Materials Chemistry Frontiers*, 1(9):1691–1708, 2017.

[62] Zhenhui Liu, Qiang Yu, Yunlong Zhao, Ruhan He, Ming Xu, Shihao Feng, Shidong Li, Liang Zhou, and Liqiang Mai. Silicon oxides: a promising family of anode materials for lithium-ion batteries. *Chemical Society Reviews*, 48(1):285–309, 2019.

[63] Yu Yao, Jingjing Zhang, Leigang Xue, Tao Huang, and Aishui Yu. Carbon-coated sio2 nanoparticles as anode material for lithium ion batteries. *Journal of Power Sources*, 196(23):10240–10243, 2011.

[64] Jordi Cabana, Laure Monconduit, Dominique Larcher, and M Rosa Palacin. Beyond intercalation-based li-ion batteries: the state of the art and challenges of electrode materials reacting through conversion reactions. *Advanced materials*, 22(35):E170–E192, 2010.

[65] Koichi Mizushima, P.C. Jones, Philip.J. Wiseman, and John.B. Goodenough. Lixcoo2 (0¡x¡-1): A new cathode material for batteries of high energy density. *Materials Research Bulletin*, 15(6):783–789, 1980.

[66] Jeffrey W. Fergus. Recent developments in cathode materials for lithium ion batteries. *Journal of Power Sources*, 195(4):939–954, 2010.

[67] Ramanan.V Chebiam, Arunachalanadar M Kannan, F Prado, and Arumugam Manthiram. Comparison of the chemical stability of the high energy density cathodes of lithium-ion batteries. *Electrochemistry Communications*, 3(11):624–627, 2001.

[68] S. Venkatraman, Y. Shin, and Arumugam Manthiram. Phase relationships and structural and chemical stabilities of charged $Li_{1-x}CoO_{2-d}$ and $Li_{1-x}Ni_{0.85}Co_{0.15}O_{2-d}$ cathodes. *Electrochemical and Solid-State Letters*, 6(1):A9, 2003.

[69] Arumugam Manthiram. A reflection on lithium-ion battery cathode chemistry. *Nature communications*, 11(1):1–9, 2020.

[70] L.A. de Picciotto, Michaelm M. Thackeray, William I.F. David, Peter G. Bruce, and John B. Goodenough. Structural characterization of delithiated livo2. *Materials Research Bulletin*, 19(11):1497–1506, 1984.

[71] Michaelm M. Thackeray, William I.F. David, and John B. Goodenough. Structural characterization of the lithiated iron oxides lixfe3o4 and lixfe2o3 (0¡x¡2). *Materials Research Bulletin*, 17(6):785–793, 1982.

[72] Michaelm M. Thackeray, William I.F. David, Peter G. Bruce, and John B. Goodenough. Lithium insertion into manganese spinels. *Materials Research Bulletin*, 18(4):461–472, 1983.

[73] Rosaling.J. Gummow, Annemaré de Kock, and Michaelm M. Thackeray. Improved capacity retention in rechargeable 4 v lithium/lithium-manganese oxide (spinel) cells. *Solid State Ionics*, 69(1):59–67, 1994.

[74] Wonchang Choi and A. Manthiram. Comparison of metal ion dissolutions from lithium ion battery cathodes. *Journal of The Electrochemical Society*, 153(9):A1760, 2006.

[75] Chun Zhan, Jun Lu, A Jeremy Kropf, Tianpin Wu, Andrew N Jansen, Yang-Kook Sun, Xinping Qiu, and Khalil Amine. Mn (ii) deposition on anodes and its effects on capacity fade in spinel lithium manganate–carbon systems. *Nature communications*, 4(1):1–8, 2013.

[76] LA De Picciotto and Michaelm M Thackeray. Insertion/extraction reactions of lithium with liv2o4. *Materials research bulletin*, 20(12):1409–1420, 1985.

[77] Akshaya K Padhi, Kirakodu S Nanjundaswamy, and John B Goodenough. Phospho-olivines as positive-electrode materials for rechargeable lithium batteries. *Journal of the electrochemical society*, 144(4):1188, 1997.

[78] Genki Kobayashi, Shin-ichi Nishimura, Min-Sik Park, Ryoji Kanno, Masatomo Yashima, Takashi Ida, and Atsuo Yamada. Isolation of solid solution phases in size-controlled lixfepo4 at room temperature. *Advanced Functional Materials*, 19(3):395–403, 2009.

[79] Natalia N. Bramnik, Kristian Nikolowski, Dmytro M. Trots, and Helmut Ehrenberg. Thermal stability of $LiCoPO_4$ cathodes. *Electrochemical and Solid-State Letters*, 11(6):A89, 2008.

[80] Arumugam V. Murugan, T. Muraliganth, and Arumugam. Manthiram. One-pot microwave-hydrothermal synthesis and characterization of carbon-coated $LiMPO_4$ (m=mn, fe, and co) cathodes. *Journal of The Electrochemical Society*, 156(2):A79, 2009.

[81] Tomoyuki Shiratsuchi, Shigeto Okada, Takayuki Doi, and Jun ichi Yamaki. Cathodic performance of limn1-xmxpo4 (m=ti, mg and zr) annealed in an intert atmosphere. *Electrochimica Acta*, 54(11):3145–3151, 2009.

[82] Sung-Wook Kim, Jongsoon Kim, Hyeokjo Gwon, and Kisuk Kang. Phase stability study of $Li_{1-x}MnPO_4$ ($0 \leq x \leq 1$) cathode for li rechargeable battery. *Journal of The Electrochemical Society*, 156(8):A635, 2009.

[83] Albina Jetybayeva, Berik Uzakbaiuly, Aliya Mukanova, Seung-Taek Myung, and Zhumabay Bakenov. Recent advancements in solid electrolytes integrated into all-solid-state 2d and 3d lithium-ion microbatteries. *Journal of Materials Chemistry A*, 9(27):15140–15178, 2021.

[84] K Karuppasamy, Jayaraman Theerthagiri, Dhanasekaran Vikraman, Chang-Joo Yim, Sajjad Hussain, Ramakant Sharma, Thandavaryan Maiyalagan, Jiaqian Qin, and Hyun-Seok Kim. Ionic liquid-based electrolytes for energy storage devices: A brief review on their limits and applications. *Polymers*, 12(4):918, 2020.

[85] Maria Assunta Navarra. Ionic liquids as safe electrolyte components for li-metal and li-ion batteries. *MRS bulletin*, 38(7):548–553, 2013.

[86] Chih-Hao Tsao, Hou-Ming Su, Hsiang-Ting Huang, Ping-Lin Kuo, and Hsisheng Teng. Immobilized cation functional gel polymer electrolytes with high lithium transference number for lithium ion batteries. *Journal of membrane science*, 572:382–389, 2019.

[87] Douglas R MacFarlane, Naoki Tachikawa, Maria Forsyth, Jennifer M Pringle, Patrick C Howlett, Gloria D Elliott, James H Davis, Masayoshi Watanabe, Patrice Simon, and C Austen Angell. Energy applications of ionic liquids. *Energy & Environmental Science*, 7(1):232–250, 2014.

[88] Davide Andrea. *Battery management systems for large lithium-ion battery packs*. Artech house, 2010.

[89] Sabu Thomas, Raju Thomas, Ajesh K Zachariah, and Raghvendra Kumar. *Spectroscopic methods for nanomaterials characterization*, volume 2. Elsevier, 2017.

[90] Ram A Sharma and Randall N Seefurth. Thermodynamic properties of the lithium-silicon system. *Journal of the Electrochemical Society*, 123(12):1763, 1976.

[91] Randall N Seefurth and Ram A Sharma. Investigation of lithium utilization from a lithium-silicon electrode. *Journal of The Electrochemical Society*, 124(8):1207, 1977.

[92] Xiuxia Zuo, Jin Zhu, Peter Müller-Buschbaum, and Ya-Jun Cheng. Silicon based lithium-ion battery anodes: A chronicle perspective review. *Nano Energy*, 31:113–143, 2017.

[93] Marc Obrovac and Leif Christensen. Structural changes in silicon anodes during lithium insertion/extraction. *Electrochemical and solid-state letters*, 7(5):A93, 2004.

[94] Marc Obrovac and VL Chevrier. Alloy negative electrodes for li-ion batteries. *Chemical reviews*, 114(23):11444–11502, 2014.

[95] Igor Kovalenko, Bogdan Zdyrko, Alexandre Magasinski, Benjamin Hertzberg, Zoran Milicev, Ruslan Burtovyy, Igor Luzinov, and Gleb Yushin. A major constituent of brown algae for use in high-capacity li-ion batteries. *Science*, 334(6052):75–79, 2011.

[96] Ranjan Dash and Sreekanth Pannala. Retracted article: Theoretical limits of energy density in silicon-carbon composite anode based lithium ion batteries. *Scientific reports*, 6(1):1–7, 2016.

[97] Bonjae Koo, Hyunjung Kim, Younghyun Cho, Kyu Tae Lee, Nam-Soon Choi, and Jaephil Cho. A highly cross-linked polymeric binder for high-performance silicon negative electrodes in lithium ion batteries. *Angewandte Chemie*, 124(35):8892–8897, 2012.

[98] Jiangxuan Song, Mingjiong Zhou, Ran Yi, Terrence Xu, Mikhail L Gordin, Duihai Tang, Zhaoxin Yu, Michael Regula, and Donghai Wang. Interpenetrated gel polymer binder for high-performance silicon anodes in lithium-ion batteries. *Advanced functional materials*, 24(37):5904–5910, 2014.

[99] H Okamoto. Li-si (lithium-silicon). *Journal of Phase Equilibria and Diffusion*, 30(1):118–119, 2009.

[100] Bujar Jerliu, Erwin Huger, Lars Dorrer, B-K Seidlhofter, Roland Steitz, Vanessa Oberst, Udo Geckle, Michael Bruns, and Hugo Schmidt. Volume expansion during lithiation of amorphous silicon thin film electrodes studied by in-operando neutron reflectometry. *The Journal of Physical Chemistry C*, 118(18):9395–9399, 2014.

[101] S Bourderau, Thierry Brousse, and Donald M Schleich. Amorphous silicon as a possible anode material for li-ion batteries. *Journal of Power Sources*, 81-82:233–236, 1999.

[102] J. P. Maranchi, A. F. Hepp, and Prashant N. Kumta. High capacity, reversible silicon thin-film anodes for lithium-ion batteries. *Electrochemical and Solid-State Letters*, 6(9):A198, 2003.

[103] Hunjoon Jung, Min Park, Shin Hee Han, Hyuck Lim, and Seung-Ki Joo. Amorphous silicon thin-film negative electrode prepared by low pressure chemical vapor deposition for lithium-ion batteries. *Solid State Communications*, 125(7):387–390, 2003.

[104] Hunjoon Jung, Min Park, Yeo-Geon Yoon, Gi-Bum Kim, and Seung-Ki Joo. Amorphous silicon anode for lithium-ion rechargeable batteries. *Journal of Power Sources*, 115(2):346–351, 2003.

[105] Shigeki Ohara, Junji Suzuki, Kyoichi Sekine, and Tsutomu Takamura. Li insertion/extraction reaction at a si film evaporated on a ni foil. *Journal of Power Sources*, 119-121:591–596, 2003. Selected papers presented at the 11th International Meeting on Lithium Batteries.

[106] Shigeki Ohara, Junji Suzuki, Kyoichi Sekine, and Tsutomu Takamura. A thin film silicon anode for li-ion batteries having a very large specific capacity and long cycle life. *Journal of Power Sources*, 136(2):303–306, 2004. Selected papers presented at the International Power Sources Symposium.

[107] Tsutomu Takamura, Shigeki Ohara, Makiko Uehara, Junji Suzuki, and Kyoichi Sekine. A vacuum deposited si film having a li extraction capacity over 2000 mah/g with a long cycle life. *Journal of Power Sources*, 129(1):96–100, 2004. Selected papers presented at the conference High Energy Density Electrochemical Power Sources.

[108] Jinghui Miao and Carl V Thompson. Kinetic study of the initial lithiation of amorphous silicon thin film anodes. *Journal of The Electrochemical Society*, 165(3):A650, 2018.

[109] Gyu bong Cho, Jung pil Noh, Ho jin Sung, Si young Choi, Sang hun Lee, Hyo jun Ahn, Tae hyun Nam, and Ki won Kim. Improved electrochemical properties of patterned si film electrodes. *Microelectronic Engineering*, 89:104–108, 2012. Materials and Devices for Future Logic Technology.

[110] Gyu bong Cho, Jae kwang Kim, Sang hoon Lee, Guk tae Kim, Jung pil Noh, Kwon koo Cho, Ki won Kim, Tae hyun Nam, and Hyo jun Ahn. Facile fabrication of patterned si film electrodes containing trench-structured cu current collectors for thin-film batteries. *Electrochimica Acta*, 224:649–659, 2017.

[111] Jae-Seung Jeong, Myung-Rang Chae, Hae-Bin Park, Yeon-Min Im, Hyo-Jun Ahn, Tae-Hyun Nam, Ki-Won Kim, and Gyu-Bong Cho. Annealing effect on electrochemical properties of patterned si film electrodes for thin-film batteries. *Current Applied Physics*, 18:S28–S32, 2018. Special issue on Recent Advances in Nanoscience and Nanotechnology.

[112] Loïc Baggetto, Dmitry Danilov, and Peter H. L. Notten. Honeycomb-structured silicon: Remarkable morphological changes induced by electrochemical (de)lithiation. *Advanced Materials*, 23(13):1563–1566, 2011.

[113] Evan Foreman, Waleed Zakri, Mohammad Hossein Sanatimoghaddam, Ali Modjtahedi, Saurabh Pathak, Ali Ghorbani Kashkooli, Nicholas G. Garafolo, and Siamak Farhad. A review of inactive materials and components of flexible lithium-ion batteries. *Advanced Sustainable Systems*, 1(11):1700061, 2017.

[114] Antonia Reyes Jimenes, Richard Klopsch, Ralf Wagner, Uta C Rodehorst, Martin Kolek, Roman Nolle, Martin Winter, and Tobias Placke. A step toward high-energy silicon-based thin film lithium ion batteries. *ACS nano*, 11(5):4731–4744, 2017.

[115] Xiaodong D. Huang, Feng Zhang, X. F. Gan, Q. A. Huang, J. Z. Yang, P. T. Lai, and W. M. Tang. Electrochemical characteristics of amorphous silicon carbide film as a lithium-ion battery anode. *RSC Adv.*, 8:5189–5196, 2018.

[116] T Sri Devi Kumari, D Jeyakumar, and T Prem Kumar. Nano silicon carbide: a new lithium-insertion anode material on the horizon. *RSC advances*, 3(35):15028–15034, 2013.

[117] Renzong Hu, Wei Sun, Yulong Chen, Meiqin Zeng, and Min Zhu. Silicon/graphene based nanocomposite anode: Large-scale production and stable high capacity for lithium ion batteries. *Journal of Materials Chemistry A*, 2(24):9118–9125, 2014.

[118] Arenst A. Arie and Joong K. Lee. Estimation of li-ion diffusion coefficients in c60 coated si thin film anodes using electrochemical techniques. *Defect and Diffusion Forum*, 326-328:87–92, 2012.

[119] Ubeyd Toçoğlu, Gizem Hatipoğlu, Miraç Alaf, Fuat Kayış, and Hatem Akbulut. Electrochemical characterization of silicon/graphene/mwcnt hybrid lithium-ion battery anodes produced via rf magnetron sputtering. *Applied Surface Science*, 389:507–513, 2016.

[120] Kuo-Feng Chiu, Shih-Hsuan Su, Hoang-Jyh Leu, and Cheng-Yu Wu. Silicon thin film anodes coated on micron carbon-fiber current collectors for lithium ion batteries. *Surface and Coatings Technology*, 267:70–74, 2015. Selected Papers from The Society of Vacuum Coater's 57th Annual Technical Conference.

[121] Yongqi Q. Zhang, Xianhui H. Xia, Xiuli L. Wang, Yongjin J. Mai, S.J. Shi, Y.Y. Tang, Lu Li, and J.P. Tu. Silicon/graphene-sheet hybrid film as anode for lithium ion batteries. *Electrochemistry Communications*, 23:17–20, 2012.

[122] Jacqueline S Edge, Simon O'Kane, Ryan Prosser, Niall D Kirkaldy, Anisha N Patel, Alastair Hales, Abir Ghosh, Weilong Ai, Jingyi Chen, Jiang Yang, et al. Lithium ion battery degradation: what you need to know. *Physical Chemistry Chemical Physics*, 23(14):8200–8221, 2021.

[123] Rajamouly S Omampuliyur, Maruf Bhuiyan, Zheng Han, Zhu Jing, Lu Li, Eugene A Fitzgerald, Carl V Thompson, and WK Choi. Nanostructured thin film silicon anodes for li-ion microbatteries. *Journal of Nanoscience and Nanotechnology*, 15(7):4926–4933, 2015.

[124] Xiao Hua Liu, Li Zhong, Shan Huang, Scott X Mao, Ting Zhu, and Jian Yu Huang. Size-dependent fracture of silicon nanoparticles during lithiation. *ACS nano*, 6(2):1522–1531, 2012.

[125] Maziar Ashuri, Qianran He, and Leon L Shaw. Silicon as a potential anode material for li-ion batteries: where size, geometry and structure matter. *Nanoscale*, 8(1):74–103, 2016.

[126] Nian Liu, Kaifu Huo, Matthew T McDowell, Jie Zhao, and Yi Cui. Rice husks as a sustainable source of nanostructured silicon for high performance li-ion battery anodes. *Scientific reports*, 3(1):1–7, 2013.

[127] Weili An, Biao Gao, Shixiong Mei, Ben Xiang, Jijiang Fu, Lei Wang, Qiaobao Zhang, Paul K Chu, and Kaifu Huo. Scalable synthesis of ant-nest-like bulk porous silicon for high-performance lithium-ion battery anodes. *Nature communications*, 10(1):1–11, 2019.

[128] Jinglu Yu, Jun Yang, Xuejiao Feng, Hao Jia, Jiulin Wang, and Wei Lu. Uniform carbon coating on silicon nanoparticles by dynamic cvd process for electrochemical lithium storage. *Industrial & Engineering Chemistry Research*, 53(32):12697–12704, 2014.

[129] Timo Ikonen, Tuomo Nissinen, Elina Pohjalainen, Olli Sorsa, Tanja Kallio, and V-P Lehto. Electrochemically anodized porous silicon: Towards simple and affordable anode material for li-ion batteries. *Scientific reports*, 7(1):1–8, 2017.

[130] Yang Jin, Sa Li, Akihiro Kushima, Xiaoquan Zheng, Yongming Sun, Jin Xie, Jie Sun, Weijiang Xue, Guangmin Zhou, Jiang Wu, et al. Self-healing sei enables full-cell cycling of a silicon-majority anode with a coulombic efficiency exceeding 99.9%. *Energy & environmental science*, 10(2):580–592, 2017.

[131] Jaewook Shin and EunAe Cho. Agglomeration mechanism and a protective role of al2o3 for prolonged cycle life of si anode in lithium-ion batteries. *Chemistry of Materials*, 30(10):3233–3243, 2018.

[132] Arenst Andreas Arie, Jin O Song, and Joong Kee Lee. Structural and electrochemical properties of fullerene-coated silicon thin film as anode materials for lithium secondary batteries. *Materials Chemistry and Physics*, 113(1):249–254, 2009.

[133] Arenst Andreas Arie and Joong Kee Lee. Estimation of li-ion diffusion coefficients in c60 coated si thin film anodes using electrochemical techniques. In *Defect and Diffusion Forum*, volume 326, pages 87–92. Trans Tech Publ, 2012.

[134] Guangyuan Zheng, Seok Woo Lee, Zheng Liang, Hyun-Wook Lee, Kai Yan, Hongbin Yao, Haotian Wang, Weiyang Li, Steven Chu, and Yi Cui. Interconnected hollow carbon nanospheres for stable lithium metal anodes. *Nature nanotechnology*, 9(8):618–623, 2014.

[135] Kwangsu Kim, Jin-Hwan Park, Seok-Gwang Doo, and T Kim. Effect of oxidation on li-ion secondary battery with non-stoichiometric silicon oxide (siox) nanoparticles generated in cold plasma. *Thin Solid Films*, 518(22):6547–6549, 2010.

[136] Jaewoo Lee, Sang A Han, Sang-Min Lee, Min-Sik Park, and Jung Ho Kim. Electrochemical properties of nonstoichiometric silicon suboxide anode materials with controlled oxygen concentration. *Composites Part B: Engineering*, 174:107024, 2019.

[137] Yidan Cao, J Craig Bennett, RA Dunlap, and Marc Obrovac. A simple synthesis route for high-capacity sio x anode materials with tunable oxygen content for lithium-ion batteries. *Chemistry of Materials*, 30(21):7418–7422, 2018.

[138] Barry C. Carter and David B. Williams. *Transmission Electron Microscopy: A Textbook for Materials Science*. Springer, 2009.

[139] [Unpublished] Armand Sepehri. Transmission electron microscopy characterization of fe – sn thin films deposited with molecular beam epitaxy. Project report in TFY4520, Department of Physics, NTNU – Norwegian University of Science and Technology, December 2021.

[140] David C. Bell and Anthony J. Garratt-Reed. *Energy dispersive X-ray analysis in the electron microscope*, volume 49. Garland Science, 2003.

[141] F Hofer, F P Schmidt, W Grogger, and G Kothleitner. Fundamentals of electron energy-loss spectroscopy. *IOP Conference Series: Materials Science and Engineering*, 109:012007, feb 2016.

[142] Wanfeng Li and Chaoying Ni. *Electron Energy Loss Spectroscopy (EELS)*, pages 940–945. Springer US, Boston, MA, 2013.

[143] Philip Ewels, Thierry Sikora, Virginie Serin, Chris P. Ewels, and Luc Lajaunie. A complete overhaul of the electron energy-loss spectroscopy and x-ray absorption spectroscopy database: eelsdb.eu. *Microscopy and Microanalysis*, FirstView:1–8, 2 2016.

[144] Philip Ewels, Thierry Sikora, Virginie Serin, Chris P. Ewels, and Luc Lajaunie. A complete overhaul of the electron energy-loss spectroscopy and x-ray absorption spectroscopy database: eelsdb.eu. *Microscopy and Microanalysis*, FirstView:1–8, 2 2016.

[145] Retrieved from https://nano.oxinst.com/products/aztec/aztectem. Accessed 16.6.2022.

[146] Asbjørn Ulvestad, Jan Maehlen, and Martin Kirkengen. Silicon nitride coated silicon thin films as anodes for li-ion batteries. *ECS Transactions*, 64:107–111, 04 2015.

[147] Bing Han, Yucheng Zou, Guiyin Xu, Shiguang Hu, Yuanyuan Kang, Yunxian Qian, Jing Wu, Xiaomin Ma, Jianquan Yao, Tengteng Li, et al. Additive stabilization of sei on graphite observed using cryo-electron microscopy. *Energy & Environmental Science*, 14(9):4882–4889, 2021.

[148] Ferdinand Hofer and Peter Wilhelm. Eels microanalysis of the elements ca to cu using m23 edges. *Ultramicroscopy*, 49(1):189–197, 1993.

[149] Asbjørn Ulvestad, Hanne Flåten Andersen, Jan Petter Mæhlen, Øystein Prytz, and Martin Kirkengen. Long-term cyclability of substoichiometric silicon nitride thin film anodes for li-ion batteries. *Scientific reports*, 7(1):1–10, 2017.

[150] Asbjørn Ulvestad, Jan Maehlen, and Martin Kirkengen. Silicon nitride as anode material for li-ion batteries: Understanding the sinx conversion reaction. *Journal of Power Sources*, 399:414–421, 09 2018.

[151] Asbjørn Ulvestad, Hanne F Andersen, Ingvild JT Jensen, Trygve T Mongstad, Jan Petter Mæhlen, Øystein Prytz, and Martin Kirkengen. Substoichiometric silicon nitride–an anode material for li-ion batteries promising high stability and high capacity. *Scientific reports*, 8(1):1–13, 2018.

[152] Hong Li, Lihong Shi, Qing Wang, Liquan Chen, and Xuejie Huang. Nano-alloy anode for lithium ion batteries. *Solid State Ionics*, 148(3-4):247–258, 2002.

[153] David Rehnlund, Fredrik Lindgren, Solveig Böhme, Tim Nordh, Yiming Zou, Jean Pettersson, Ulf Bexell, Mats Boman, Kristina Edström, and Leif Nyholm. Lithium trapping in alloy forming electrodes and current collectors for lithium based batteries. *Energy & Environmental Science*, 10(6):1350–1357, 2017.

[154] Bin Zhu, Guoliang Liu, Guangxin Lv, Yu Mu, Yunlei Zhao, Yuxi Wang, Xiuqiang Li, Pengcheng Yao, Yu Deng, Yi Cui, et al. Minimized lithium trapping by isovalent isomorphism for high initial coulombic efficiency of silicon anodes. *Science advances*, 5(11):eaax0651, 2019.

[155] Florian Holtstiege, Peer Bärmann, Roman Nölle, Martin Winter, and Tobias Placke. Prelithiation strategies for rechargeable energy storage technologies: Concepts, promises and challenges. *Batteries*, 4(1):4, 2018.

[156] Fei Wang, Bo Wang, Jingxuan Li, Bin Wang, Yu Zhou, Dianlong Wang, Huakun Liu, and Shixue Dou. Prelithiation: a crucial strategy for boosting the practical application of next-generation lithium ion battery. *ACS nano*, 15(2):2197–2218, 2021.

[157] Sujong Chae, Seong-Hyeon Choi, Namhyung Kim, Jaekyung Sung, and Jaephil Cho. Integration of graphite and silicon anodes for the commercialization of high-energy lithium-ion batteries. *Angewandte Chemie International Edition*, 59(1):110–135, 2020.

[158] Fei Dou, Liyi Shi, Guorong Chen, and Dengsong Zhang. Silicon/carbon composite anode materials for lithium-ion batteries. *Electrochemical Energy Reviews*, 2(1):149–198, 2019.

[159] Wei Sun, Renzong Hu, Hui Liu, Meiqin Zeng, Lichun Yang, Haihui Wang, and Min Zhu. Embedding nano-silicon in graphene nanosheets by plasma assisted milling for high capacity anode materials in lithium ion batteries. *Journal of Power Sources*, 268:610–618, 2014.

[160] Ubeyd Toçoğlu, Gizem Hatipoğlu, Miraç Alaf, Fuat Kayış, and Hatem Akbulut. Electrochemical characterization of silicon/graphene/mwcnt hybrid lithium-ion battery anodes produced via rf magnetron sputtering. *Applied Surface Science*, 389:507–513, 2016.

[161] Kuo-Feng Chiu, Shih-Hsuan Su, Hoang-Jyh Leu, and Cheng-Yu Wu. Silicon thin film anodes coated on micron carbon-fiber current collectors for lithium ion batteries. *Surface and Coatings Technology*, 267:70–74, 2015.

[162] Yongqi Q. Zhang, Xianhui H. Xia, Xiuli L. Wang, Yongjin J. Mai, S.J. Shi, Y.Y. Tang, Lu Li, and J.P. Tu. Silicon/graphene-sheet hybrid film as anode for lithium ion batteries. *Electrochemistry communications*, 23:17–20, 2012.

[163] Xiaohui Shen, Zhanyuan Tian, Ruijuan Fan, Le Shao, Dapeng Zhang, Guolin Cao, Liang Kou, and Yangzhi Bai. Research progress on silicon/carbon composite anode materials for lithium-ion battery. *Journal of Energy Chemistry*, 27(4):1067–1090, 2018.

[164] Retrieved from https://scitechdaily.com/lighter-faster-charging-batteries-created-that-could-make-it-easier-to-explore-mars/. Accessed 09.06.2022.

[165] Retrieved from https://www.electronicdesign.com/power-management/article/21801593/nasa-targets-sulfur-and-silicon-to-bolster-lithium-batteries. Accessed 09.06.2022.

Appendices

APPENDIX A

SUPPLEMENTARY RESULTS

A.1 SEM Images of Film Morphology

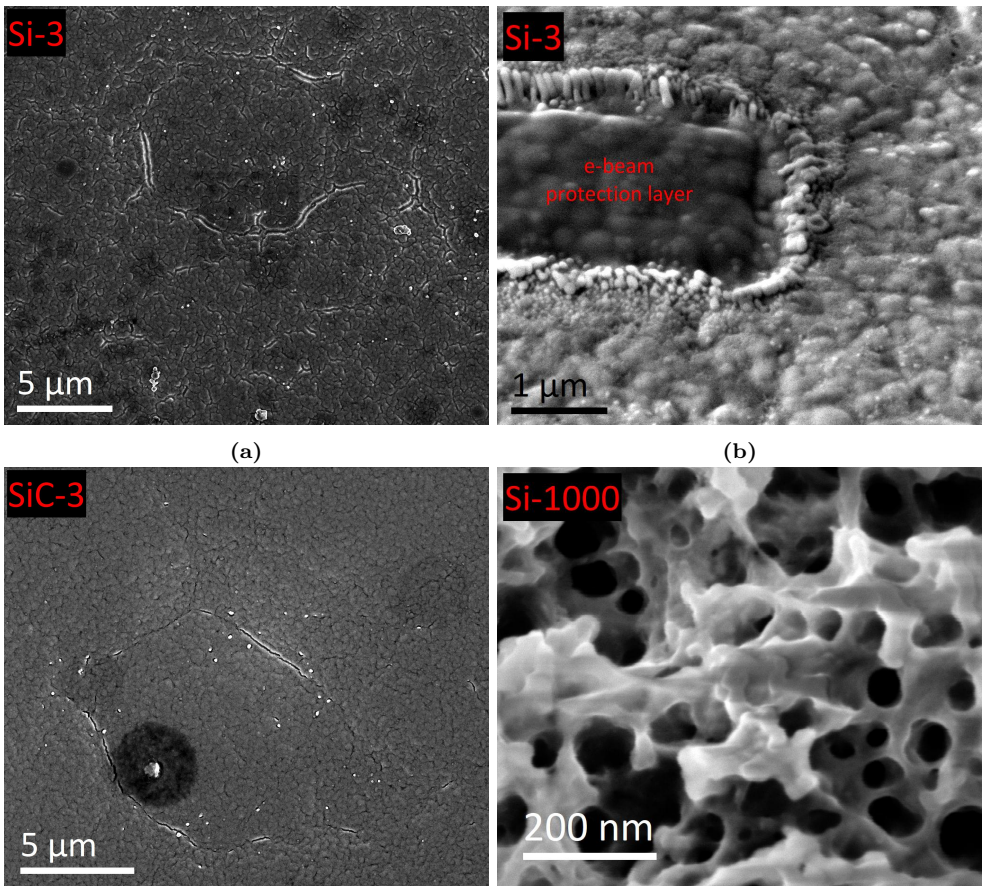

Fig. A.1.1: Additional secondary electron SEM images of the surface morphology. Images not included in the main report, as the purpose of SEM images only is to complement the TEM results. a) Si-3 overview. b) Si-3 after deposition of electron-beam carbon protection layer, showing structural changes in the film as a consequence beam sensitivity. c) SiC-3 overview. d) Si-1000 $<$ 100 nm holes on the film surface.

A.2 SEM Images of TEM Lamellae

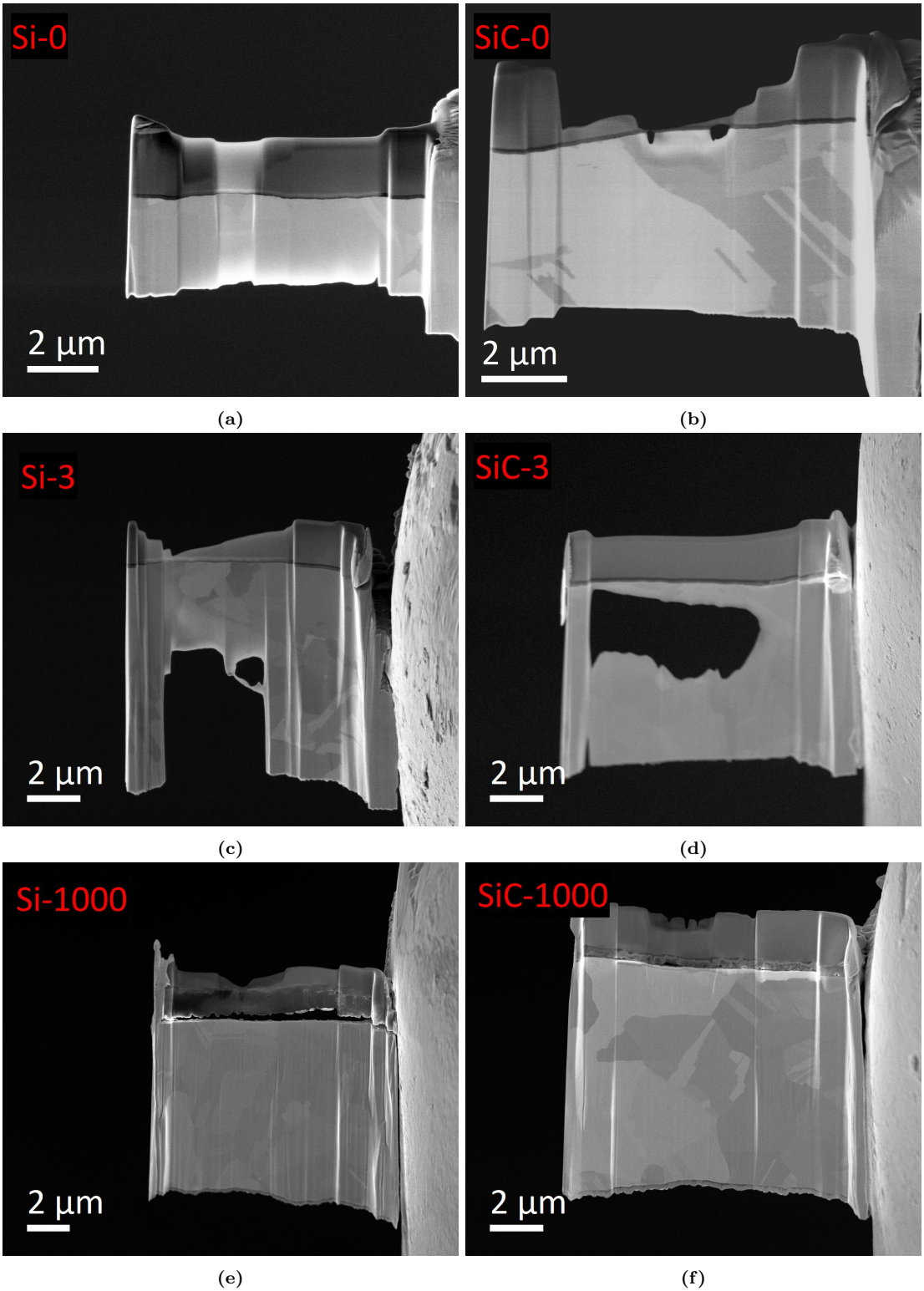

Fig. A.2.1: Secondary electron SEM images of TEM lamellae. a) Si-0. b) SiC-0. c) Si-3. d) SiC-3. e) Si-1000. f) SiC-1000.

A.3 TEM Overview Images of films with low magnification

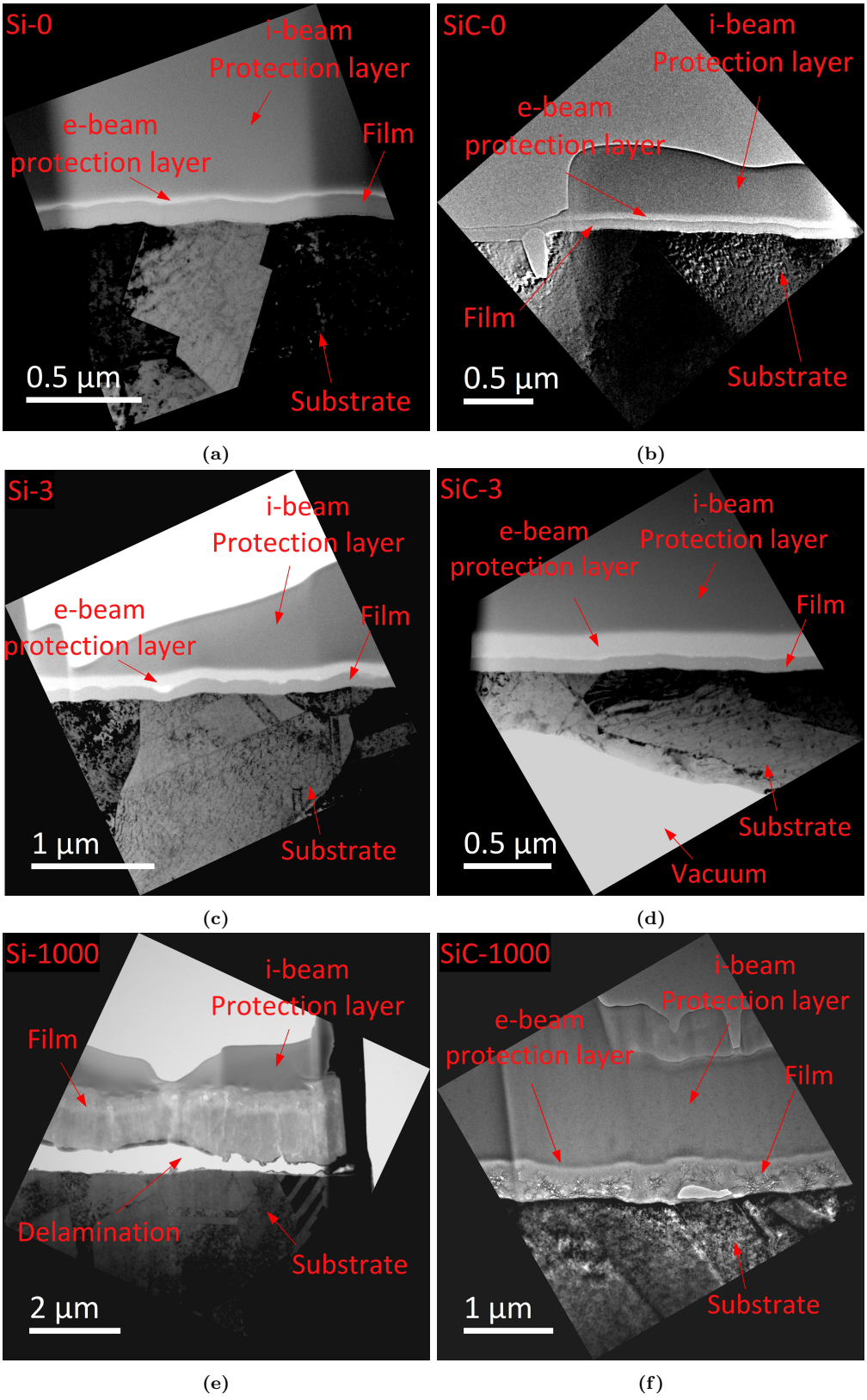

Fig. A.3.1: HAADF STEM images acquired with the 2100F instrument with low magnification, showing thickness variations in the films. a) Si-0. b) SiC-0. c) Si-3. d) SiC-3. e) Si-1000. f) SiC-1000.

A.4 EDS Maps

Si-0

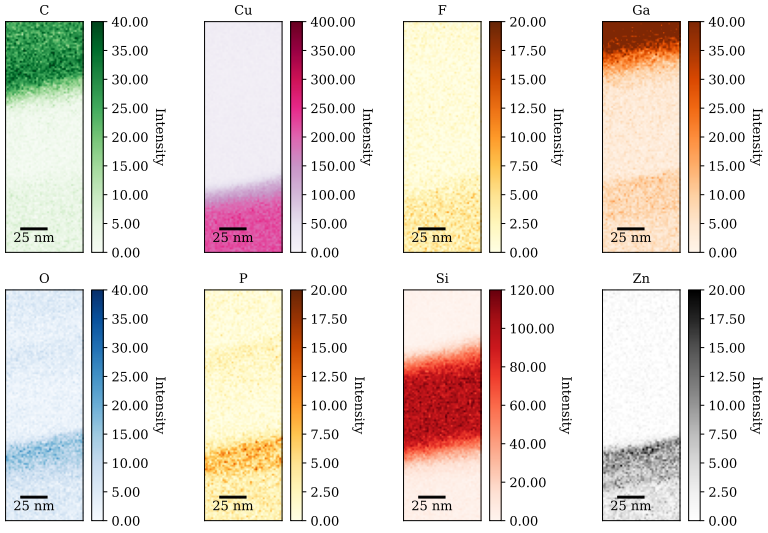

(a)

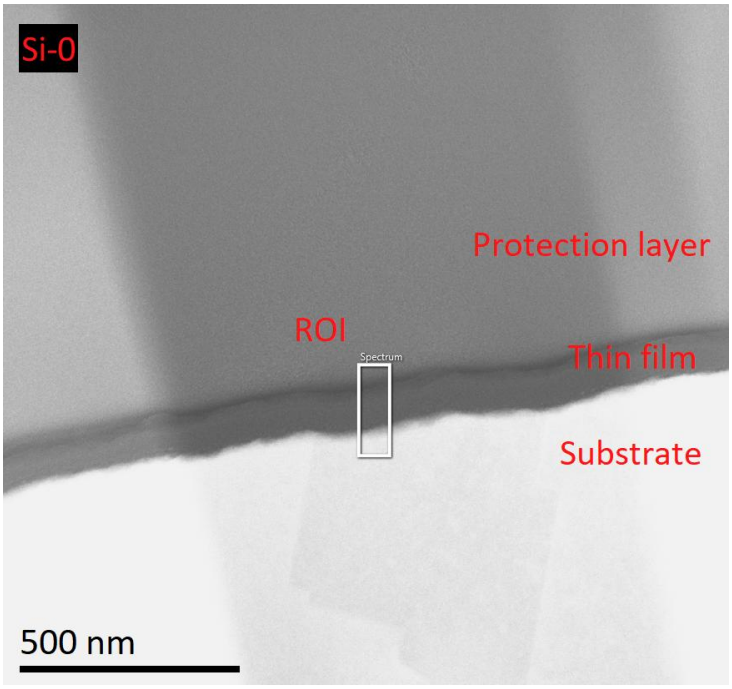

(b)

Fig. A.4.1: a) EDS colormaps of sample Si-0, showing the distribution of C, Cu, F, Ga, O, P, Si and Zn i the sample. b) Corresponding HAADF STEM image.

SiC-0

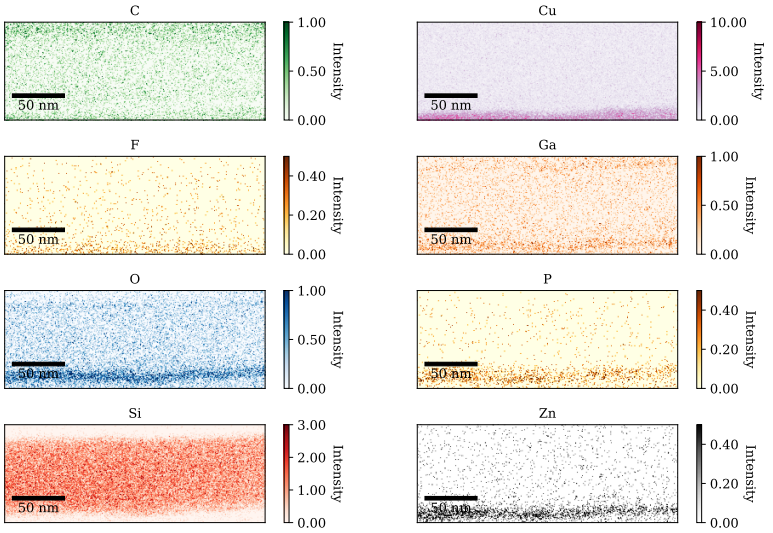

(a)

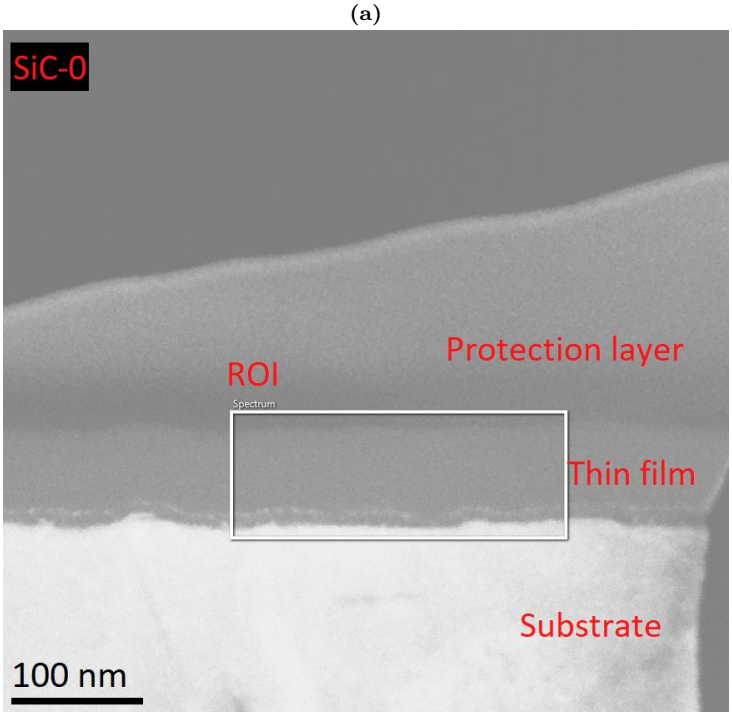

(b)

Fig. A.4.2: a) EDS colormaps of sample SiC-0, showing the distribution of C, Cu, F, Ga, O, P, Si and Zn i the sample. b) Corresponding HAADF STEM image.

Si-3

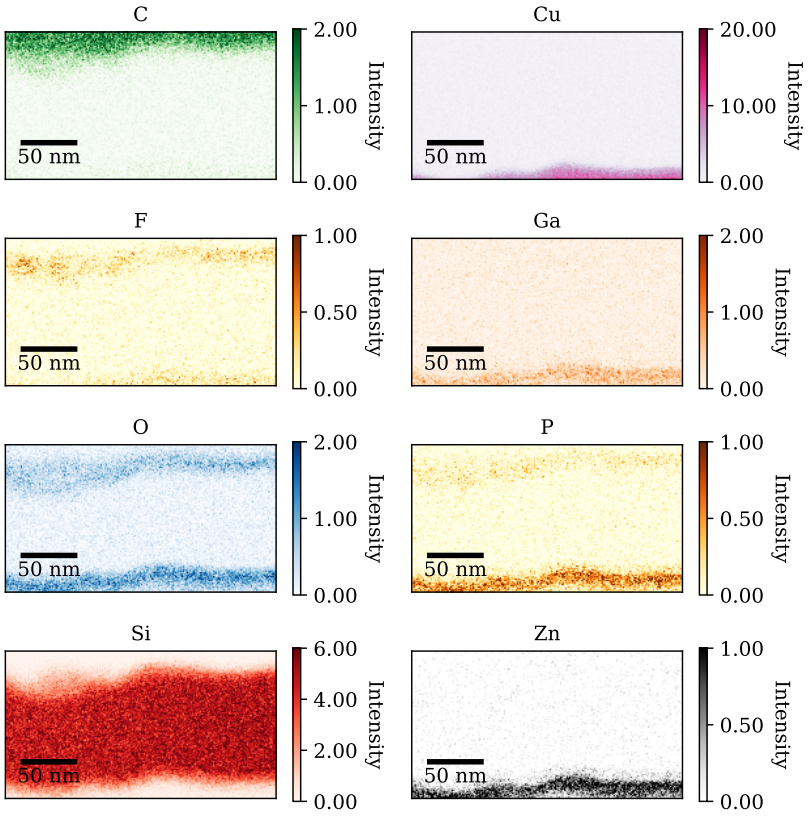

(a)

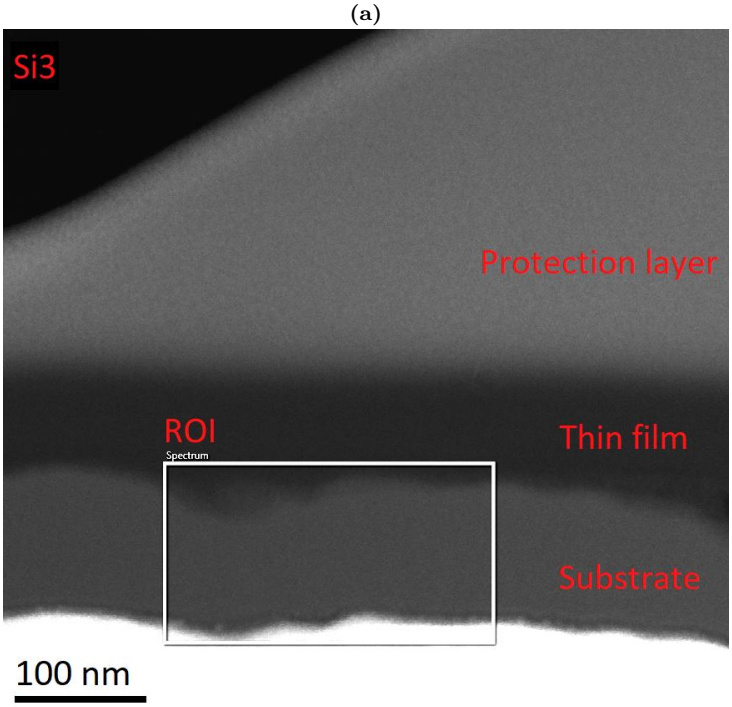

(b)

Fig. A.4.3: a) EDS colormaps of sample Si-3, showing the distribution of C, Cu, F, Ga, O, P, Si and Zn i the sample. b) Corresponding HAADF STEM image.

SiC-3

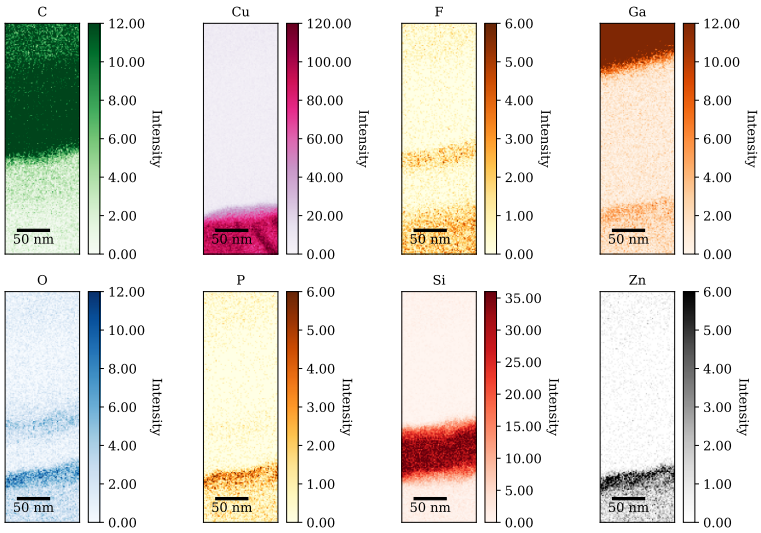

(a)

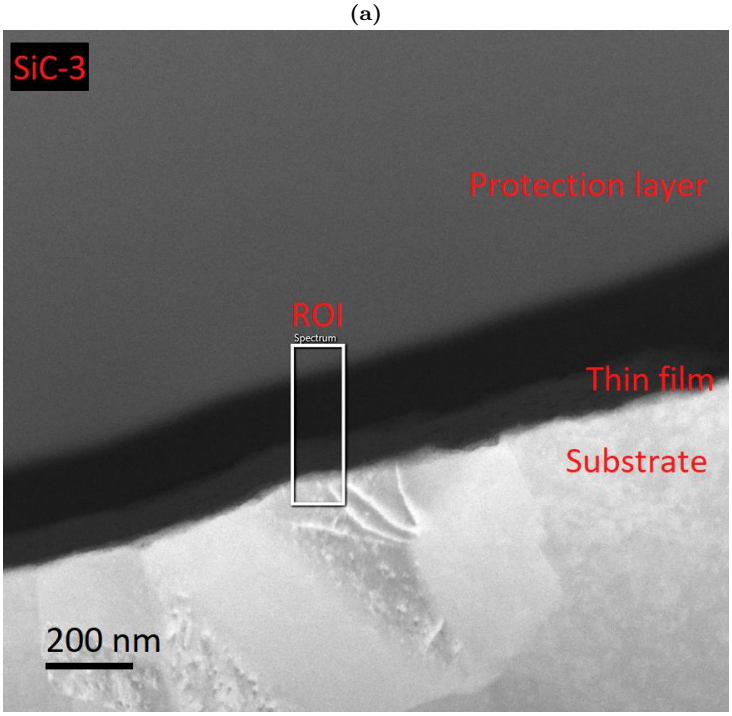

(b)

Fig. A.4.4: a) EDS colormaps of sample SiC-3, showing the distribution of C, Cu, F, Ga, O, P, Si and Zn i the sample. b) Corresponding HAADF STEM image.

Si-1000

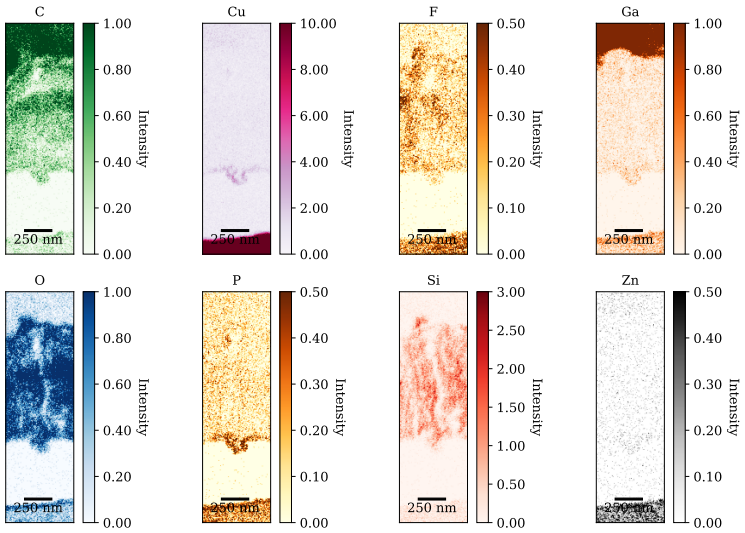

(a)

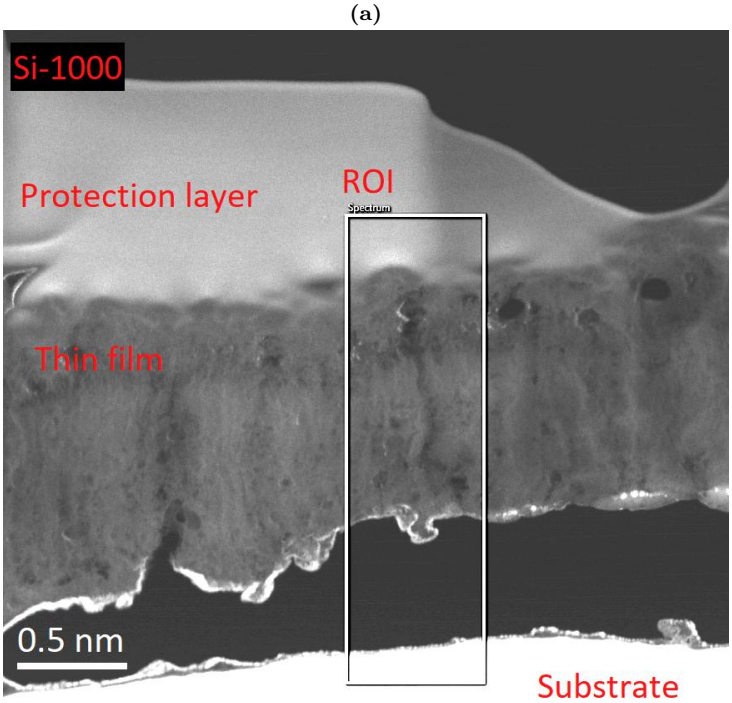

(b)

Fig. A.4.5: a) EDS colormaps of sample Si-1000, showing the distribution of C, Cu, F, Ga, O, P, Si and Zn i the sample. b) Corresponding HAADF STEM image. This image is mirrored relative to the other images of Si-1000.

SiC-1000

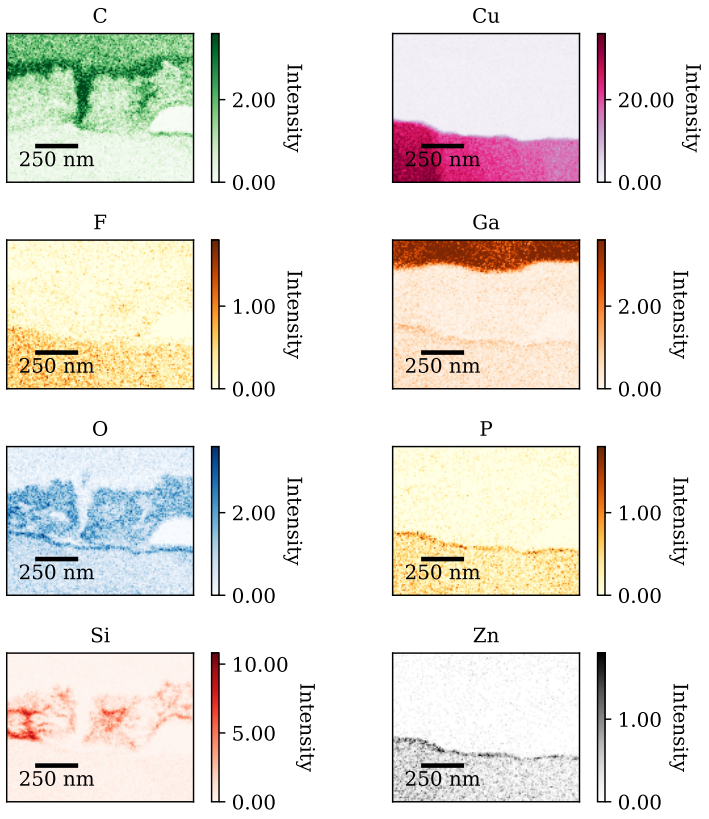

(a)

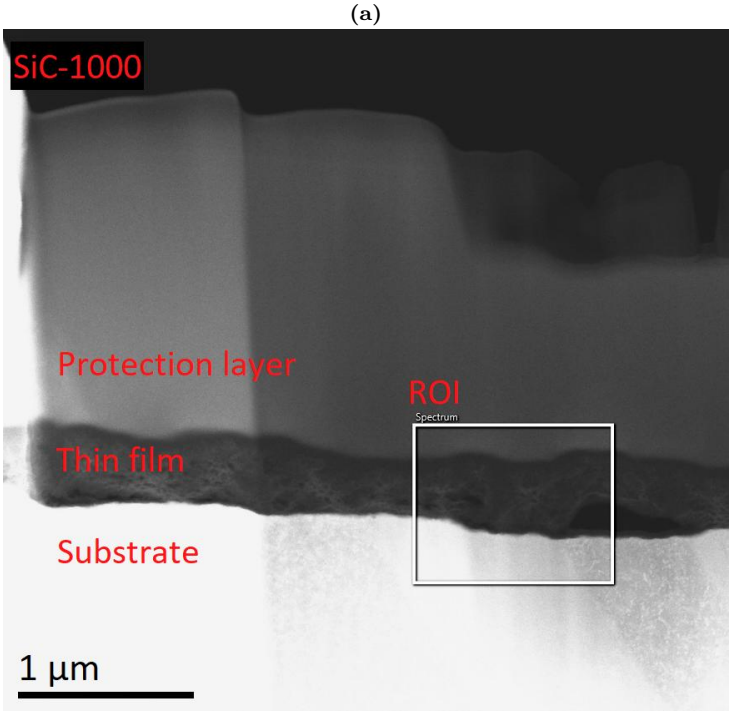

(b)

Fig. A.4.6: a) EDS colormaps of sample SiC-1000, showing the distribution of C, Cu, F, Ga, O, P, Si and Zn i the sample. b) Corresponding HAADF STEM image.

A.5 Quantitative EDS STEM Images

Table A.5.1: Atom % of Si, C, O, Cu, Ga, F, P and Zn in samples Si-0, SiC-0, Si-3, SiC-3. This is the same table as Table 4.5.1, which is provided again with the corresponding HAADF STEM images in section A.5.

Sample	Si[at%]	C[at%]	O[at%]	Cu[at%]	Ga[at%]	F[at%]	P[at%]	Zn[at%]
Si-0	80,46	5,2	5,06	8,39	0,82	0,07	0	0
Si-3	85,49	2,3	4,9	6,88	0,38	0,05	0	0
Si-1000	9,18	33,92	45,1	7,04	0,35	3,94	0,48	0
SiC-0	40,78	21,66	18,93	17,66	0,96	0	0	0
SiC-3	61,45	27,19	4,57	6,15	0,63	0,02	0	0
SiC-1000	8,34	57,3	28	4,49	0,56	1,14	0,14	0,02

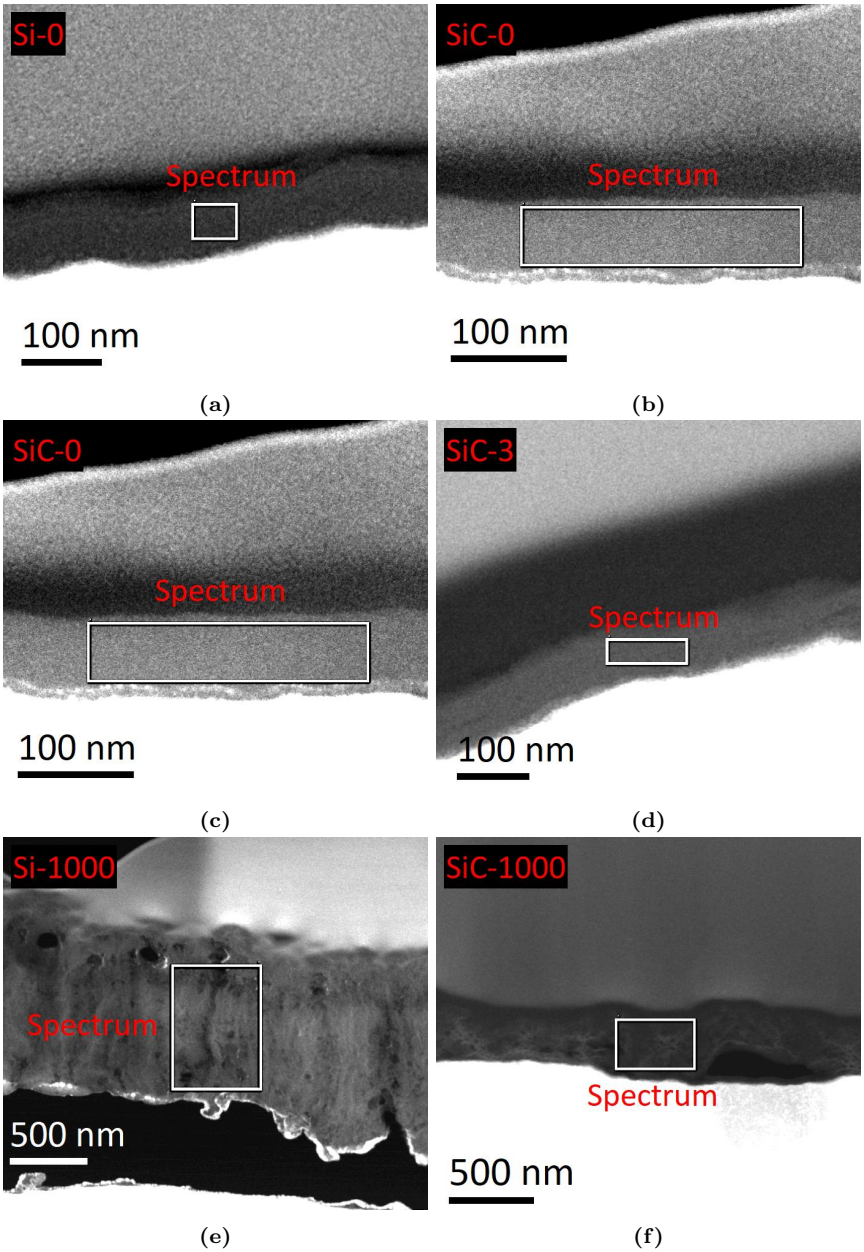

Fig. A.5.1: Corresponding HAADF STEM images acquired with the 2100F instrument, for values in Table 4.5.1. a) Si-0. b) SiC-0. c) Si-3. d) SiC-3. e) Si-1000. f) SiC-1000.

APPENDIX B

GALVANOSTATIC CYCLING PARAMETERS

Table B.0.1: Galvanostatic cycling parameters. The initial thickness is based by on ellipsometry measurements by Marte O. Skare at IFE. Assumed density is based on XPS results by Marte O. Skare at IFE. Active mass is based on the assumed density and the dimensions of the electrode.

Sample	Pure Si	SiC_x
Initial thickness [nm]	66	70
Assumed density [g/cm^3]	2.285	2.251
Active mass [ug]	28.3	31.1
Voltages [V]	1-0.05	1-0.05
Cycle 1	C/20, C/100, C/200 taper	C/20, C/100, C/200 taper
Cycle 2-3	C/20	C/20
Cycle 4->	1C	1C

APPENDIX C

LINESCAN SMOOTHING CODE

The code provided below, was used to smoothen out the plots in Figures 4.5.3 and 4.5.4. This caused the Cu-signal to drop close to the scan edge, which was addressed in the report. This because of the simple nature of the algorithm, which does not properly take edge values into consideration. The function takes in a numpy array, and a chosen number of datapoints used in the smoothening, and return a new array which gives a better looking plot. The function was used to make the plots more easily readable. The raw data is also provided in the mentioned figures, with a brighter contrast.

```
import numpy as np
def smooth(y, box_pts):
    box = np.ones(box_pts)/box_pts
    y_smooth = np.convolve(y, box, mode='same')
    return y_smooth

# y          = numpy array of data which is smoothed out
# box_pts    = number of adjacent datapoints used to smooth out (4 was used)
```

APPENDIX D

SUPPORTING RESULTS FROM IFE

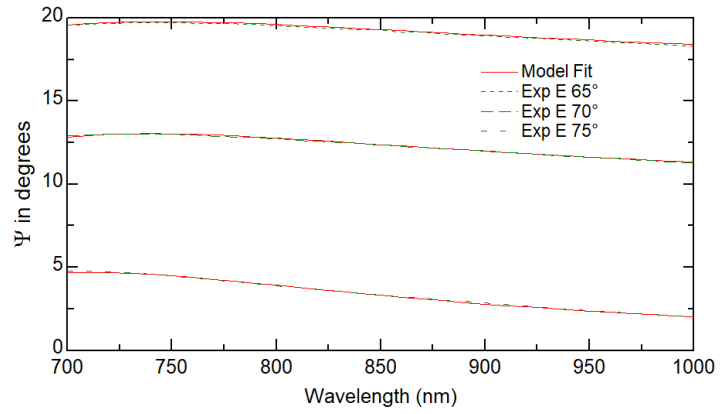

(a)

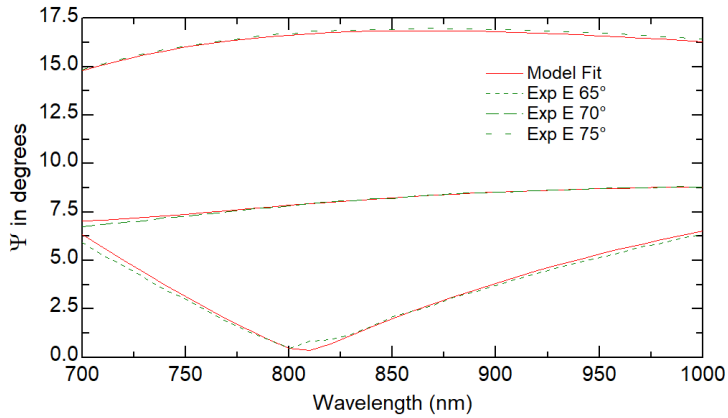

(b)

Fig. D.0.1: Ellipsometry thickness measurements done by Marte O. Skare at IFE. A good, but not excellent model fit is shown to the ellipsometry data. Note that these films are not the same as the ones examined throughout this thesis, but equivalent films deposited on Si wafers. a) Pure silicon. b) SiC_x

Armand Sepehri

TEM Characterization of Degradation Mechanisms in LIBs

NTNU
Norwegian University of
Science and Technology